

**COMPUTATIONAL METHODS
FOR THE DISCRETE
DOWNWARD CONTINUATION
OF THE EARTH GRAVITY AND
EFFECTS OF LATERAL
TOPOGRAPHICAL MASS
DENSITY VARIATION ON
GRAVITY AND THE GEOID**

JIANLIANG HUANG

July 2002



**TECHNICAL REPORT
NO. 216**

**COMPUTATIONAL METHODS FOR THE
DISCRETE DOWNWARD CONTINUATION OF
THE EARTH GRAVITY AND EFFECTS OF
LATERAL TOPOGRAPHICAL MASS DENSITY
VARIATION ON GRAVITY AND THE GEOID**

Jianliang Huang

Department of Geodesy and Geomatics Engineering
University of New Brunswick
P.O. Box 4400
Fredericton, N.B.
Canada
E3B 5A3

July 2002

© Jianliang Huang 2002

PREFACE

This technical report is a reproduction of a dissertation submitted in partial fulfillment of the requirements for the degree of Doctor of Philosophy in the Department of Geodesy and Geomatics Engineering, July 2002. The research was supervised by Dr. Petr Vanicek, and funding was provided by the Natural Sciences and Engineering Research Council of Canada.

As with any copyrighted material, permission to reprint or quote extensively from this report must be received from the author. The citation to this work should appear as follows:

Huang, Jianliang (2002). *Computational Methods for the Discrete Downward Continuation of the Earth Gravity and Effects of Lateral Topographical Mass Density Variation on Gravity and the Geoid*. Ph.D. dissertation, Department of Geodesy and Geomatics Engineering, Technical Report No. 216, University of New Brunswick, Fredericton, New Brunswick, Canada, 141 pp.

Abstract

In this thesis, computational methods for the discrete Poisson downward continuation of the Earth gravity are studied. In addition, the effect of the lateral topographical mass density variation on gravity and the geoid is systematically investigated.

A solution in the spherical harmonic form for the Poisson integral equation is derived. It is pointed out that the solution of the discrete inverse Poisson problem exists, but may not be unique and stable. For a small input error, a large output error is introduced. It is in this sense that the inverse Poisson problem is said to be an ill-posed problem.

It is found that the modified spheroidal Poisson kernel reduces the ‘real’ far-zone contribution with respect to using the spheroidal Poisson kernel significantly, but it cannot perform better than the standard Poisson kernel in reducing it. A fast algorithm is developed for the evaluation of the far-zone contribution.

Heiskanen and Moritz’s (1967) radius condition gives a critical radius of the near-zone cap that is too small for the determination of the cm-geoid, while Martinec’s (1996) condition gives an unnecessarily large radius. It is proposed that the critical near-zone radius be determined as a function of the accuracy of the global geopotential model from which the far-zone contribution is evaluated.

The combined iterative method is proposed to speed up the convergence of the solution of the discrete inverse Poisson problem. The truncated singular value decomposition method is introduced to solve the discrete Poisson integral equation that may be ill-conditioned for a small discrete step.

The three discrete models for the Poisson integral, namely the point-point, point-mean and mean-mean models are assessed against synthetic data. It is shown that the mean-mean model can produce a sufficiently accurate solution when the so called ‘averaging error’ is properly corrected for.

A block-wise technique is developed to solve the discrete Poisson integral equation efficiently with a compressed storage technique for the coefficient matrix. The package DOWN97 is developed to evaluate the discrete Poisson downward continuation.

The analytical downward continuation is compared to the Poisson one by using synthetic data and Helmert gravity anomalies. It is shown that the analytical downward continuation agrees with the discrete Poisson's within 10% of the total downward continuation effect. A fast algorithm is developed to evaluate the analytical downward continuation with its implementation in software.

An ultra-high degree synthetic global geopotential model conforming to the Kaula-type degree variance models is too smooth to simulate the Helmert gravity anomalies, especially in mountainous regions.

An approach for evaluating the effect of the lateral topographical mass density variation on gravity and the geoid is proposed. Formulae for evaluating the standard deviation of the primary indirect topographical mass density effect (PIDE), the direct topographical mass density effect (DDE) and the secondary topographical mass density effect (SIDE) are derived. The effect of the lateral topographical mass density variation on the geoid height ranges from -7.0 cm to 2.8 cm by using a $30'' \times 30''$ DTM (Digital Topographic Model). The software for evaluating the PIDE, DDE and SIDE is described.

Acknowledgements

I am grateful to my advisor and mentor, Prof. Dr. Petr Vaníček for his continuous support and inspiring guidance when I was on and off the campus. The open-minded discussions with him created a unique studying atmosphere. The experience of working with him is an invaluable asset for my career.

I am thankful to my advisor and supervisor, Dr. Spiros D. Pagiatakis at GSD. His guidance and support were indispensable for the continuation and completion of my studies. His knowledge, rigorousness, confidence, and ambition are beneficial to me.

My appreciation is extended to Prof. Dr. Richard Langley, Prof. Dr. David Wells, Prof. Dr. Larry Mayer and Prof. Dr. Alfred Kleusberg for their involvement of supervision. I am indebted to Dr. Wenke Sun, Prof. Dr. Eric Grafarend, Prof. Dr. Michael Sideris, Prof. Dr. Zdeněk Martinec, Prof. Dr. Will E. Featherstone, Dr. Martin Vermeer and Dr. R. O. Castle for the constructive discussions with them. I wish to thank Prof. Dr. David J. Coleman and Ms. M. Wojnarowska for their help with the GIS software, my colleagues at GSD Mr. Marc Véronneau and Dr. André Mainville for sharing their knowledge with me, and Mr. Paul Collins for his time and effort in improving English of this manuscript.

My thanks go to Mrs. Linda O'Brien for all including helps, to my fellow graduate and visiting students of the geodesy group at UNB, Mehdi Najafi, Pavel Novák, Jeff Wong, Juraj Janák, Wilbert Brink, Mensur Omerbašić, and Roderick A. Schipper for the weekly round-table discussions on geodesy with them.

Finally, my wife Shen Chunlin and my son Kaiwen deserve more than thanks for their love, patience, and encouragement.

Contents

Abstract	ii
Acknowledgements	iv
List of Figures	x
List of Tables	xiii
List of Abbreviations	xvi
List of Latin Symbols	xvii
List of Greek Symbols	xx
1 Introduction	1
1.1 The Geoid, Quasigeoid and Height Systems	1
1.2 Geodetic Boundary Value Problems and Downward Continuations . .	4
1.2.1 The Stokes Solution	5
1.2.2 The Molodenskii Solution	7
1.2.3 The Hotine Solution	9
1.3 Review	10
1.4 Objectives	15
1.5 Contributions	16

2	Basic Theory	19
2.1	Dirichlet's Problem and Poisson's Integral Equation	19
2.2	The Inverse Problem and Downward Continuation	21
2.3	Solvability of the Poisson Downward Continuation	23
2.4	Summary	28
3	Discretization of Poisson's Integral Equation	29
3.1	The Far-Zone Contribution	29
3.1.1	Formulation	30
3.1.2	Standard vs. Modified Kernels	37
3.1.3	Determination of The Critical Angular Radius of the Near-Zone Cap	41
3.1.4	An Efficient Algorithm of the Far-Zone Contribution	45
3.2	The Discrete Poisson Integral Equations	50
3.2.1	The Point-Point Model	53
3.2.2	The Point-Mean Model	54
3.2.3	The Mean-Mean Model	55
3.2.4	Analysis of the Discrete Models	56
3.3	Summary	59
4	Solution of the Discrete Poisson Integral Equations	62
4.1	The Combined Iterative Method	63
4.2	Synthetic Geopotential Models	65
4.3	Synthetic Tests of Discrete Models for Poisson's Integral Equation . .	68
4.4	Some Numerical Characteristics of the Mean-Mean Model	74
4.5	Synthetic Test for The Critical Radius of the Near-Zone Cap	76
4.6	Algorithm	77
4.7	Implementation: DOWN'97	81
4.8	The Truncated Singular Value Decomposition Method	81

4.9	Summary	83
5	Analytical Downward Continuation	85
5.1	Theory	85
5.2	Computational Method	87
5.3	Numerical Comparisons with the Discrete Poisson Downward Continuation	88
5.3.1	Synthetic Comparisons	88
5.3.2	Comparisons Using the Helmert Gravity Anomaly	98
5.4	Summary	99
6	Topographical Density Variation Effects on Gravity and the Geoid	104
6.1	Introduction	104
6.2	Digital Topographical Density Model	106
6.3	Mathematical Formulation	108
6.4	Numerical Results	112
6.4.1	Mean Direct Density Effect	113
6.4.2	Primary Indirect Density Effect	118
6.4.3	Total Lateral Topographical Density Variation Effect on the Geoid	118
6.5	Summary	122
7	Conclusions and Recommendations	123
7.1	Solvability of the Discrete Poisson Downward Continuation	124
7.2	Discretization of Poisson's integral	124
7.3	Solution of the Discrete Inverse Poisson Problem	125
7.4	Analytical Downward Continuation	126
7.5	Topographical Density Variation Effects on Gravity and Geoid	127

7.6 Recommendations	128
References	129
Vita	
Main Publications	
Main Conference Papers	

List of Figures

1.1	Geoid, quasigeoid and height systems.	2
1.2	The real and the Helmert spaces.	6
1.3	Moritz's analytical downward continuation from the Earth Surface to the point level.	8
2.1	λ_n^{-1} versus degree n . $H = 2 \text{ km}$	27
3.1	K , $K^{l, S}$ and $K^{l, MS}$ vs. ψ ($30' - 60'$). $H = 2 \text{ km}$	35
3.2	K , $K^{l, S}$ and $K^{l, MS}$ vs. ψ ($1^\circ - 180^\circ$). $H = 2 \text{ km}$	36
3.3	The truncation error coefficients Q_n^I . $\psi_0 = 1^\circ$, $H = 2 \text{ km}$	38
3.4	The far-zone contributions $F_{\Delta g}^{l, I}$ vs. degree n . $\psi_0 = 1^\circ$, $H = 2 \text{ km}$. . .	39
3.5	The standard deviation m_F^I vs. degree n . $\psi_0 = 1^\circ$, $H = 2 \text{ km}$	40
3.6	The far-zone contribution effect on geoid in the Rocky Mountains. $\psi_0 = 1^\circ$. Contour interval: 0.002 m.	42
3.7	The truncation error coefficients Q_n of the standard Poisson kernel K for different radii ψ_0 . $H = 2 \text{ km}$	46
3.8	The far-zone contributions $F_{\Delta g}^{20}$ for different radii ψ_0 . $H = 2 \text{ km}$. . .	47
3.9	The standard deviations of the far-zone contributions m_F for different radii ψ_0 . $H = 2 \text{ km}$	48
3.10	$C_\alpha(m, H, \theta)$ vs. H	51
3.11	$C_\alpha(m, H, \theta)$ vs. m	52

3.12	The singular value spectrum of the coefficient matrices for the point-point model (solid lines), the point-mean model (dotdashed lines), and the mean-mean model (dashed lines) of $5' \times 5'$	60
4.1	Anomaly degree variances σ_n^2 of the Tscherning/Rapp degree variance model, EGM96 and GPM98a.	67
4.2	Error distribution of the downward continuation using the GPM98a synthetic data.	70
4.3	The 3-D table for the doubly averaged kernel coefficients $\overline{\overline{B_{ij}}}$	78
4.4	The matrix coefficients of the discrete Poisson equation $b_{ij}(= \overline{\overline{B_{ij}}})$ vs. H for different ψ	79
4.5	The block-wise approach.	80
5.1	The geoid height error distribution for the DDC and ADC of the EGM96 synthetic data.	91
5.2	The point-point DDC effect on the geoid from the synthetic gravity data of EGM96 (21-360). Contour interval: 0.01 m.	92
5.3	The ADC effect on the geoid from the synthetic gravity data of EGM96 (21-360). Contour interval: 0.01 m.	93
5.4	The geoid height error distribution for the DDC and ADC of the GPM98a synthetic data.	95
5.5	The point-point DDC effect on the geoid from the synthetic gravity data of GPM98a (21-1800). Contour interval: 0.01 m.	96
5.6	The ADC effect on the geoid from the synthetic gravity data of GPM98a (21-1800). Contour interval: 0.01 m.	97
5.7	The point-point DDC effect on the geoid, using the residual Helmert gravity anomalies above degree 20 of EGM96. Contour interval: 0.1 m.	100
5.8	The ADC effect on the geoid, using the residual Helmert gravity anomalies above degree 20 of EGM96. Contour interval: 0.1 m.	101

5.9	The difference between the DDC and ADC effects on the geoid, using the residual Helmert gravity anomalies. Contour interval: 0.02 m. . .	102
6.1	The lateral topographical mass density map in the Rocky Mountains. White areas indicate water bodies and geographical boundaries. Unit: g/cm^3	109
6.2	The standard deviation of the topographical mass density in the Rocky Mountains. White areas indicate water bodies and geographical boundaries. Unit: g/cm^3	109
6.3	Geoid correction profiles due to the mean DDE computed from different number of point values.	114
6.4	The mean DDE $\overline{\delta A_D}$ on gravity at the Earth surface in the Canadian Rocky Mountains in mGal. The solid lines delimit water bodies. . . .	115
6.5	The point standard deviation of the DDE $\sigma_{\delta A}$ in the Canadian Rocky Mountains in mGal. The solid lines delimit water bodies.	115
6.6	The mean DDE $\overline{\delta A_D}$ on the geoid in the Canadian Rocky Mountains in mGal. The solid lines delimit water bodies.	116
6.7	The mean DDE on the geoid in the Canadian Rocky Mountains. Contour interval: 1 cm.	117
6.8	The PIDE δN_D on the geoid in the Canadian Rocky Mountains. Contour interval: 1 cm.	119
6.9	The standard deviation of the PIDE $\sigma_{\delta N}$ in the Canadian Rocky Mountains (cm).	120
6.10	The sum of the DDE and PIDE on the geoid in the Canadian Rocky Mountains. Contour interval: 1 cm.	121

List of Tables

3.1	The modified Poisson kernel coefficients $t_n(H, 1^\circ)$	34
3.2	Statistics of the mean $5' \times 5'$ DEM in the test regions. Unit: m. . . .	58
3.3	Condition numbers in the test regions by using the mean $5' \times 5'$ DEM.	58
4.1	The $5' \times 5'$ point-point downward continuation of the synthetic field of degree 21 to degree 1800 derived from GPM98a. $\psi_0 = 1^\circ$. Unit: mGal.	69
4.2	The $5' \times 5'$ point-mean downward continuation of the synthetic field of degree 21 to degree 1800 derived from GPM98a. $\psi_0 = 1^\circ$. Unit: mGal.	69
4.3	The $5' \times 5'$ mean-mean downward continuation of the synthetic field of degree 21 to degree 1800 derived from GPM98a. $\psi_0 = 1^\circ$. Unit: mGal.	69
4.4	The $5' \times 5'$ mean-mean downward continuation of the synthetic field of degree 21 to degree 1800 derived from GPM98a <i>with the correction of the averaging error</i> . $\psi_0 = 1^\circ$. Unit: mGal.	72
4.5	The averaging errors and their downward continuation of the mean-mean model for different grid steps. $\psi_0 = 1^\circ$. Unit: mGal.	72
4.6	The mean-mean downward continuation errors for different grid steps with and without the correction of the averaging errors. $\psi_0 = 1^\circ$. Unit: mGal.	73
4.7	The $5' \times 5'$ mean-mean downward continuation errors of the synthetic field of degree 21 to degree 1800 derived from GPM98a due to using different DTMs for evaluating the coefficients $\overline{\overline{B_{ij}}}$. $\psi_0 = 1^\circ$. Unit: mGal.	75

4.8	The $5' \times 5'$ mean-mean downward continuation errors of the synthetic field of degree 21 to degree 1800 derived from GPM98a due to using different grids of point values for evaluating the mean anomalies on the Earth's surface. Unit: mGal.	75
4.9	The mean-mean downward continuation errors of the synthetic field of degree 21 to degree 1800 derived from GPM98a due to using different grids for evaluating the downward continuation. Unit: mGal.	76
4.10	The point-point downward continuation of the synthetic field of degree 21 to degree 1800 derived from GPM98a for $\psi_0 = 0.5^\circ$. Unit: mGal.	77
5.1	The point-point DDC of the synthetic field of EGM96 (21-360) in the test region. Unit: mGal.	90
5.2	The ADC of the synthetic field of EGM96 (21-360) in the test region. Unit: mGal.	90
5.3	Accuracy of the point-point DDC and the ADC by using the synthetic field of EGM96 (21-360) in the test region. Unit: m.	90
5.4	The point-point DDC of the synthetic field of GPM98a (21-1800) in the test region. Unit: mGal.	94
5.5	The ADC of the synthetic field of GPM98a (21-1800) in the test region. Unit: mGal.	94
5.6	Accuracy of the point-point DDC and the ADC by using the synthetic field of GPM98a (21-1800) in the test region. Unit: m.	95
5.7	Statistics of the residual Helmert gravity anomaly above degree 20 of EGM96 and the height data in the test region.	99
5.8	The gravity results of the DDC and the ADC from the residual Helmert gravity anomaly in the test region. Unit: mGal.	99
5.9	The geoid height results of the DDC and the ADC from the residual Helmert gravity anomaly in the test region. Unit: m.	100

6.1	Direct topographical lateral density variation effects on gravity at the Earth surface in mGal.	114
6.2	Direct and primary indirect lateral topographical density variation effects on geoid heights, in cm.	116
6.3	Topographic mass density variation effects versus the total topographical effects using the actual mean density value. (Note: DTE, SITE and PITE by Vaníček et al. are computed by using the constant density 2.67 g/cm^3 .)	118
6.4	Distribution of the total effect values caused by the lateral topographical mass density variation.	119

List of Abbreviations

ADC	analytical downward continuation
DDC	discrete Poisson downward continuation
DDE	direct topographical mass density effect
DTE	direct topographical effect
DEM	digital elevation model
DTDM	digital topographical mass density model
EGM96	Earth Geopotential Model 96
GBVP	geodetic boundary value problem
GIS	Geographic Information System
GSD	Geodetic Survey Division, Natural Resources Canada
GRS80	Geodetic Reference System 1980
PIDE	primary indirect topographical mass density effect
PITE	primary indirect topographical effect
RMS	root of mean squares
StdDev	standard deviation
SIDE	secondary indirect topographical mass density effect
SITE	secondary indirect topographical effect
SVE	singular value expansion
SVD	singular value decomposition
TSVD	truncated singular value decomposition

List of Latin Symbols

c_{nm}, d_{nm}	spherical harmonic coefficients of gopotential
d	distance between two points on the sphere of radius R
dC_{nm}	the standard deviations of the geopotential model coefficients
$d\epsilon$	the discretization error
f	the flattening of the Earth
\mathbf{f}	parameter vector
\mathbf{g}	observation vector
g	actual Earth gravity
g_n	term n in the analytical downward continuation
\bar{g}	mean actual Earth gravity along the plumb line
h	geodetic height
k	the maximum degree being taken for evaluation of the far-zone contribution
k	the truncation parameter for the TSVD
m	order of spherical harmonics
m_F^I	the standard deviation of the far-zone contribution for K^l, I
n	degree of spherical harmonics
n	the normal to the reference ellipsoidal surface
r	geocentric radius
r_g	geocentric radius of a point on the geoid
r_t	geocentric radius of the computation point on the Earth surface
r'_t	geocentric radius of the integration point on the Earth surface

t_n	the modified Poisson kernel coefficients
v	domain of a harmonic function
B	integral operator or coefficient matrix
\tilde{B}	an approximation of B
B_{ij}	matrix coefficients for the point-point model
$\overline{B_{ij}}$	matrix coefficients for the point-mean model
$\overline{\overline{B_{ij}}}$	matrix coefficients for the mean-mean model
C_{nm}	the fully normalized spherical harmonic coefficients of geopotential
$D\Delta g$	downward continuation of gravity anomaly
\mathcal{F}	the model space
$F_{\Delta g}$	the far-zone contribution of Poisson's integral
$F_{\Delta g}^{l, I}$	the far-zone contribution of Poisson's integral above degree l for $K^{l, I}$
G	universal gravitational constant
H	height above a reference sphere of radius R
H^0	orthometric height
H^N	normal height
I	superscript indicating the type of kernel in use
K	the Poisson kernel
K_l	the first l degrees of terms in the Poisson kernel
$K^{l, MS}$	the modified spheroidal Poisson kernel
$K^{l, S}$	the spheroidal Poisson kernel
\mathcal{L}	the data space
L	distance between two points
L	the integral operator for the analytical downward continuation
M	mass of the Earth
M	the total number of cells within the near-zone
N	geoid height
N	the total number of unknown parameters

N^h	Helmert's co-geoid height
P_n	Legendre's polynomial of the first kind
$P_{n,m}$	associated Legendre's function of the first kind
Q_n	truncation error coefficients of Poisson's integral
Q_n^{MS}	truncation error coefficients of Poisson's integral for K_{MS}
Q_n^S	truncation error coefficients of Poisson's integral for K_S
R	the mean radius of the Earth
S	spherical Stokes's kernel function
T	disturbing gravity potential
T^h	Helmert's disturbing gravity potential
W	actual gravity potential
U	normal gravity potential
U, Σ, V	SVD matrices
V	harmonic function
$Y_{n,m}$	surface spherical harmonic functions
$\overline{Y_{n,m}}$	mean surface spherical harmonic functions over cells

List of Greek Symbols

γ	normal gravity
$\bar{\gamma}$	mean normal gravity along the plumb line
γ_g	normal gravity on the geoid
γ_E	normal gravity on the reference ellipsoid
γ_T	normal gravity on the telluroid
δ	parameter error vector
δg	gravity disturbance
δA	the direct topographical effect on gravity (DTE)
δA_D	the direct topographical mass density effect on gravity (DDE)
δN_D	the primary indirect topographical mass density effect on the geoid (PIDE)
δ_N^{adc}	the geoid height error of the ADC
δ_N^{ddc}	the geoid height error of the DDC
$\delta\gamma$	the secondary indirect topographical effect (SITE)
$\delta\gamma_D$	the secondary indirect topographical mass density effect (SIDE)
$\delta\bar{\rho}$	lateral density variation
ϵ	observation error vector
ζ	height anomaly
θ	geocentric co-latitude
λ	geocentric longitude
λ'	geocentric longitude of the integration point
λ_n	singular-values of degree n

ν	the normal to the telluroid
ρ	density of topographical masses
ρ_0	constant density 2.67 g/cm^3
$\bar{\rho}$	cell mean density of topographical masses
σ_n^2	degree variances
σ_{nm}	the surface spherical harmonic coefficients of a function
$\sigma_{\bar{\rho}}$	the standard deviation of the mean topographical mass density
$\sigma_{\bar{\rho}}(\Omega', \Omega'')$	covariance of the mean topographical mass densities between two points
$\sigma_{\delta A}$	the standard deviation of the DDE
$\sigma_{\delta N}$	the standard deviation of the PIDE
$\sigma_{\delta \gamma}$	the standard deviation of the SIDE
τ	the surface density function
ϕ	geocentric latitude
ϕ'	geocentric latitude of the integration point
ψ	angular distance between two points
ψ_0	angular radius of the near-zone
Δ	the sampling step of data
Δg	the free-air gravity anomaly
Δg^B	the simple Bouguer gravity anomaly
$\Delta g'$	the free-air gravity anomaly at a point level
Δg^h	Helmert's gravity anomaly
Δg^l	gravity anomaly components above degree l
$\overline{\Delta g^l}$	mean gravity anomaly components above degree l
ΔS_j	integration surface elements
$\Delta \lambda$	the data sampling step in the longitude direction
Ω	solid angle denoting the pair (θ, λ) for the computation point
Ω'	solid angle denoting the pair (θ', λ') for the integration point
Ω'_0	the near integration zone with the angular radius ψ_0

Chapter 1

Introduction

1.1 The Geoid, Quasigeoid and Height Systems

The *geoid* is defined as an equipotential surface of the gravitational and rotational Earth coinciding with the mean sea level of the oceans. It is a natural reference surface for heights since it is horizontal everywhere. Its shape is roughly an oblate ellipsoid with semi-axes 6378 and 6357 km, but may deviate locally from the *best-fitting ellipsoid* in about value by as much as 100 m. The best-fitting ellipsoid is usually considered as the geocentric ellipsoid that is closest to the geoid, with a mass identical to that of the Earth. Its minor axis is always parallel to the Earth axis of rotation. The *normal potential* U generated by the ellipsoid on the ellipsoidal surface is equal to the actual potential W_0 on the geoid. The *geoid height* or *geoid undulation* is defined as the distance of a point on the geoid from the best-fitting ellipsoidal surface along the normal to the ellipsoidal surface, and is denoted by N (see Figure 1.1). The height of the natural surface of the Earth above the geoid is called the *orthometric height* and is denoted by H^0 , while the height above the ellipsoidal surface is called the *geodetic height* denoted by h . These three parameters

are related by (Vaníček and Krakiwsky, 1986)

$$h = N + H^0. \quad (1.1)$$

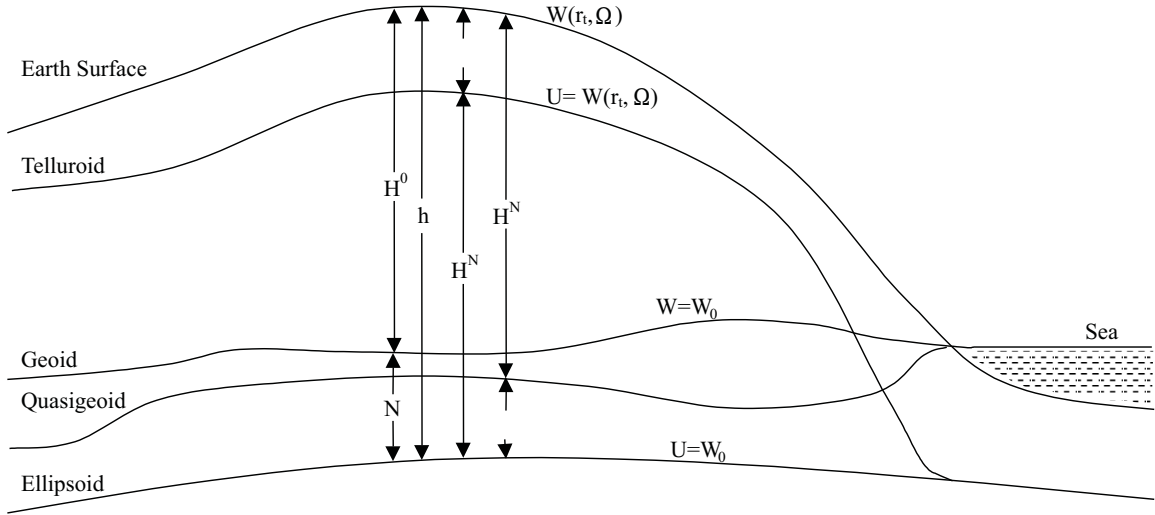


Figure 1.1: Geoid, quasigeoid and height systems.

A parallel concept to the geoid is the *quasigeoid*. It was defined by Molodenskii et al.(1960). In the Molodenskii system, a conceptual surface called the *telluroid* is introduced as the surface whose normal potential of any point is equal to the actual potential at the corresponding point on the Earth surface. The distance between the telluroid and the Earth surface along the normal to the telluroid is called the *height anomaly* denoted by ζ . The quasigeoid is a surface that is displaced from the reference ellipsoid by the height anomaly. Unlike the geoid, the quasigeoid is not an equipotential surface but it coincides with the geoid in the open oceans. The height of a point above the quasigeoid is called the *normal height* denoted by H^N . The pair

(N, H^0) is related to the pair (ζ, H^N) by

$$N + H^0 = \zeta + H^N. \quad (1.2)$$

The height anomaly ζ can be converted to the geoid height N by (Heiskanen and Moritz, 1967)

$$N = \zeta + \frac{\bar{g} - \bar{\gamma}}{\bar{\gamma}} H^0, \quad (1.3)$$

where \bar{g} is the mean value of the actual gravity along the plumb line between the geoid and the Earth surface, $\bar{\gamma}$ is the mean value of the normal gravity along the normal to the reference ellipsoid from the telluroid. The conversion relation between H^0 and H^N can be obtained by substituting eqn. (1.3) into eqn. (1.2)

$$H^N = H^0 + \frac{\bar{g} - \bar{\gamma}}{\bar{\gamma}} H^0. \quad (1.4)$$

The orthometric height and the normal height systems are the most widely used systems in the world. There exist other height systems: for example the dynamic height doesn't have geometrical meaning and can be derived from leveled height (Vaníček and Krakiwsky, 1986). The orthometric height (or the normal height) can be determined by traditional spirit leveling, a precise but inefficient method. An efficient alternative is satellite positioning. Satellite positioning systems such as GPS, GLONASS and the upcoming GALILEO allow us to determine geodetic heights with an accuracy of better than 1 cm. In order to derive the orthometric height or the normal height from the satellite-determined geodetic height without losing accuracy, the geoid (or quasigeoid) has to be known to the same accuracy. The geoid (or quasigeoid) provides the means of converting geodetic to orthometric heights for a number of satellite positioning applications such as topographic mapping, GPS leveling, navigation, hydrographic surveying, oceanography and others.

1.2 Geodetic Boundary Value Problems and Downward Continuations

The geoid can be determined from the *disturbing potential* denoted by T , that is defined as the difference between the actual gravity potential W and the normal gravity potential U at a point

$$T(r, \Omega) = W(r, \Omega) - U(r, \Omega), \quad (1.5)$$

where Ω is the solid angle denoting the pair (θ, λ) , the spherical co-latitude and longitude, and r is the geocentric radius of the point. The disturbing potential T is harmonic everywhere above the Earth surface (ignoring the existence of the atmosphere).

If the disturbing potential T is known on the Earth surface, the height anomaly ζ can be determined by using *Bruns formula*

$$\zeta = \frac{T(r_t, \Omega)}{\gamma_T}, \quad (1.6)$$

where r_t is the geocentric radius of a point on the Earth surface, γ_T is the normal gravity at the corresponding point on the telluroid.

If the disturbing potential T is known on the geoid, the geoid height N can be determined by using Bruns formula

$$N = \frac{T(r_g, \Omega)}{\gamma_E}, \quad (1.7)$$

where r_g is the geocentric radius of a point on the geoid, γ_E is the normal gravity on the reference ellipsoid.

Assuming the disturbing potential T is harmonic, i.e. it satisfies the Laplace differential equation

$$\Delta T = 0, \quad (1.8)$$

it can be determined by solving the boundary value problem (BVP) for the Laplace equation which is called the *geodetic boundary value problem* (GBVP) in physical

geodesy. Three representative solutions for this equation are: the Stokes (1849), the Molodenskii et al. (1962) and the Hotine (1969) solutions. Stokes and Molodenskii et al. derive their solutions by solving the third boundary value problem, while the Hotine solution is based on the second boundary value problem.

1.2.1 The Stokes Solution

The Stokes solution may be obtained by making use of the boundary condition

$$\left. \frac{\partial T(r, \Omega)}{\partial n} \right|_{r=r_g} - \frac{1}{\gamma_E} \frac{\partial \gamma}{\partial n} T(r_g, \Omega) = -\Delta g(r_g, \Omega), \quad (1.9)$$

where

$$\Delta g(r_g, \Omega) = g(r_g, \Omega) - \gamma_E, \quad (1.10)$$

is the *gravity anomaly* on the geoid, n is the normal to the ellipsoidal surface, $g(r_g, \Omega)$ is the gravity on the geoid, and γ_E is the normal gravity on the reference ellipsoid. Then the solution for the disturbing potential T is given by the *Stokes integral* (Stokes, 1949)

$$T(r_g, \Omega) = \frac{R}{4\pi} \int_{\Omega'} S(\psi) \Delta g(r_g, \Omega) d\Omega', \quad (1.11)$$

where R is the mean radius of the Earth, $S(\psi)$ is the spherical Stokes kernel ¹.

Stokes solution to eqn. (1.8) is valid only when there are no masses outside the geoid. The existence of topography and atmosphere violates this condition. The removal of the masses above the geoid, one way or another, is necessary to fulfill this condition. A number of reduction methods have been proposed for this purpose. In Canada and the US, Helmert's 2nd condensation reduction has been used to determine the geoid (Vaníček and Kleusberg, 1987; Véronneau, 1996; Vaníček et al., 1999; Smith and Milbert, 1999). Following this scheme, the topography and the atmosphere are

¹The Stokes formula gives a spherical approximation to T . A more accurate solution should take the ellipsoidal correction into consideration (Sagrebín, 1956; Molodenskii, 1962; Bjerhammar, 1966; Koch, 1968; Moritz, 1974; Martinec and Grafarend, 1997; Fei and Sideris; 2000, 2001; Huang et al, 2000)

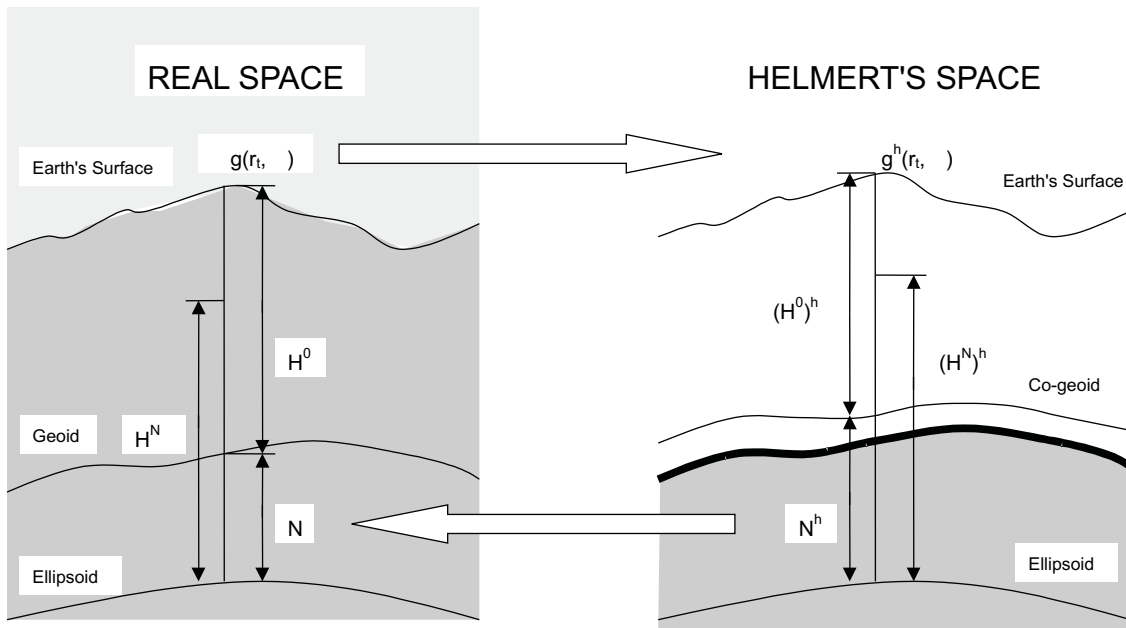


Figure 1.2: The real and the Helmert spaces.

condensed so as to form a surface layer just beneath the geoid. It is a limiting case of an isostatic reduction according to the Pratt-Hayford system as the depth of compensation D goes to zero (Heiskanen and Moritz, 1967). Vaníček and Martinec (1994) define the Stokes problem with Helmert's 2nd condensation as the *Stokes-Helmert scheme* (see Figure 1.2). The principle of this scheme may be described as follows (Vaníček and Sjöberg, 1991; Najafi, 1996; Vaníček et al., 1999):

1. Transforming the “observed gravity anomaly” Δg_t on the Earth surface from the real space into the Helmert gravity anomaly Δg_t^h , referred to the same surface in Helmert space,
2. *Continuing* Δg_t^h downwards to the Helmert co-geoid,
3. Solving the boundary value problem in the Helmert space, i.e., solving for the Helmert co-geoid using Stokes formula,

4. Transforming the co-geoid to the geoid by adding the primary indirect topographical and atmospherical effect (PITE and PIAE).

The first step (from real space to Helmert space) involves the removal and condensation of the topographical masses, which require the mass density distribution between the geoid and the Earth surface. Since the density information for the whole topography is difficult to obtain, a constant density ($2.67g/cm^3$) is usually assumed in place of the real one, introducing an error into the Helmert gravity anomaly and the geoid solution. The unknown topographical mass density imposes theoretical and practical challenges to the application of the Stokes-Helmert method because of the incomplete removal and condensation of topography by using constant density in the first step. One of the objectives of this research is to investigate the topographical mass density variation effects on the geoid for the Stokes-Helmert method.

1.2.2 The Molodenskii Solution

In order to avoid the removal and condensation (or compensation) of the topographical masses, Molodenskii defines the boundary as the Earth surface in his solution to eqn. (1.8), which is called the “modern” geodetic boundary value problem. The Molodenskii solution may be obtained by making use of the following boundary condition on the Earth’s surface: (Molodenkii et al., 1960; Moritz, 1969; Sideris, 1987)

$$\left. \frac{\partial T(r, \Omega)}{\partial \nu} \right|_{r=r_t} - \frac{1}{\gamma_T} \frac{\partial \gamma}{\partial \nu} T(r_t, \Omega) = -\Delta g(r_t, \Omega), \quad (1.12)$$

where

$$\Delta g(r_t, \Omega) = g(r_t, \Omega) - \gamma_T \quad (1.13)$$

is the gravity anomaly on the Earth surface, $g(r_t, \Omega)$ is the actual gravity on the Earth surface, and ν is the normal to the telluroid. The solution for the disturbing potential T may be given by the following series (Moritz, 1969)

$$T(r_t, \Omega) = \frac{R}{4\pi} \int_{\Omega'} S(\psi) \Delta g(r_t, \Omega) d\Omega' + \sum_{n=1}^{\infty} \frac{R}{4\pi} \int_{\Omega'} S(\psi) g_n d\Omega', \quad (1.14)$$

where g_n are the *analytical downward continuation* terms.

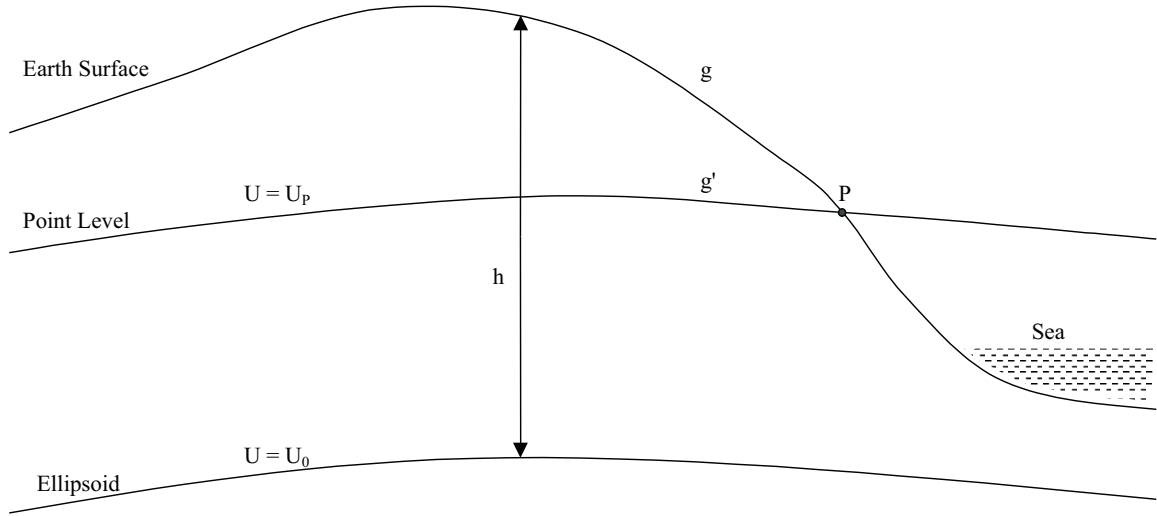


Figure 1.3: Moritz’s analytical downward continuation from the Earth Surface to the point level.

The analytical downward continuation is used to reduce the gravity anomaly to a level surface on which the Stokes integration can be carried out to compute the disturbing potential T (see Figure 1.3). Consider a point P at the Earth surface and the equipotential surface $U = U_P$ passing through P (so-called “point level”). Then the gravity anomaly Δg given at the Earth surface may be analytically continued to that point level, yielding $\Delta g'$

$$\Delta g' = \sum_{n=0}^{\infty} g_n. \quad (1.15)$$

Note that $\Delta g'$ refers to the level surface $U = U_P$. Consequently, Stokes’s formula can be applied to determine T on the Earth surface.

Sideris (1987) suggested a method to determine the downward continuation terms g_n by a *two-step continuation* procedure, in which the gravity anomalies are analytically continued from the telluroid down to the geoid as Δg^0 , then an upward continuation of Δg_0 to the point level finally provides $\Delta g'$.

1.2.3 The Hotine Solution

The Hotine solution to eqn. (1.8) can be obtained by using the boundary condition on the geoid

$$\left. \frac{\partial T(r, \Omega)}{\partial n} \right|_{r=r_g} = -\delta g(r_g, \Omega), \quad (1.16)$$

where

$$\delta g(r_g, \Omega) = g(r_g, \Omega) - \gamma_g \quad (1.17)$$

is called the *gravity disturbance* on the geoid, and γ_g is the normal gravity on the geoid.

The solution for the disturbing potential T can be given by using the Hotine kernel function $H(\psi)$ (Hotine, 1969, 29.17) ²

$$T(r_g, \Omega) = \frac{R}{4\pi} \int_{\Omega'} H(\psi) \delta g(r_g, \Omega) d\Omega', \quad (1.18)$$

Similar to Stokes' solution, the Hotine solution also requires harmonicity of T above the geoid. A similar reduction scheme to that of Stokes-Helmert is applicable to the Hotine method as well. Accordingly, the downward continuation is also an essential step to reduce δg from the Earth surface to the geoid. The Hotine kernel function allows the gravity disturbance δg to contain the zero-order and the first-order terms, while the terms of order 0 and 1 are considered as 'forbidden' as in the Stokes solution. In other words, the reference ellipsoid may not be geocentric and may have a different normal potential on the ellipsoidal surface from the actual potential on the geoid if the Hotine solution is applied for geoid determination. Evaluation of δg requires known geodetic heights for generating the normal gravity on the Earth's surface. This requirement has limited the application of the Hotine solution because only the orthometric heights are available at most gravity points.

We have seen that the downward continuation is a fundamental step in determining the disturbing potential in all three solutions. The use of this technique is

²This solution represents a spherical approximation of T , and an ellipsoidal correction is needed to give a more accurate solution.

theoretically and practically necessary so that the Stokes formula and the Hotine formula can be applied rigorously and so that the height anomaly can then be evaluated efficiently by the Fast Fourier Transform (FFT) (Sideris, 1987), or by improved numerical integration (Huang et al., 2000). However it is a controversial issue whether this step leads to a better geoid solution since the downward continuation is classified as an ill-posed problem in geodetic literature. In other words, whether and how the downward continuation can be applied to generate a centimeter-geoid is still an open question. The main objective of this research is to study the downward continuation method for the geoid determination, and answer this question.

The downward continuation is also an indispensable step for airborne gravimetry (Schwarz, 1978; Forsberg and Kenyon, 1995; Novák et. al, 2000). Airborne gravimetry has the advantage of allowing a rapid coverage of large regions of the world with significant economy over other methods. It is particularly useful and necessary for covering coastal, mountainous and polar regions. Since the data are collected at the flight level, they have to be continued downward to the geoid for both geophysical and geodetic applications.

1.3 Review

The downward continuation problem is classified as an ill-posed problem due to the fact that a comparatively smooth function of the gravity anomaly is used to construct a more detailed and therefore ‘rougher’ function of the gravity anomaly. Hofmann-Wellenhof and Moritz (1986) show by a planar spectral analysis that there is an exponential amplification of the gravity anomalies at high frequencies when continued downwards. For satellite perturbation methods, the 300-th degree coefficients of the gravity anomaly at an altitude of 150 km must be known with an accuracy of 1 μgal ($10^{-8}ms^{-2}$) in order to recover 1 $mgal$ ($10^{-5}ms^{-2}$) accuracy at the Earth surface (Jekeli, 1981). Milbert (1999) states: “One is faced with the ‘dilemma of downward

continuation'. If one uses a coarse grid, one suffers from omission error in a geoid product. If one uses a finer grid, one suffers from error and noise amplification." Schwarz (1978) summarizes numerical features of the ill-posed problem as follows:

- (a) "The solution does not continuously depend on the given data, i.e., small changes in the data may cause large changes in the solution."
- (b) "The matrices resulting from the discretization of the problem will be ill-conditioned, i.e., the inverse matrices will strongly oscillate and the condition numbers will be large."
- (c) "The accuracy of the solution does not increase with the grid density, i.e., as the grid becomes smaller, any norm of the approximate solution typically becomes large."

A recent revisiting of the problem of downward continuation gives a different understanding to it. Vaníček et al. (1996) demonstrate that the determination of the downward continuation of mean Helmert's gravity anomalies on a grid of reasonable step (5 arc-sec.) is a well-posed problem with a unique solution and can be done routinely to any accuracy desired in the geoid computation. Martinec (1996) shows that the problem is stable until the discretization step becomes smaller than 50 arc-seconds. Furthermore, Vaníček and Wong (1999) argue: "For Helmert's gravity anomalies, the answer to all three Hadamard's conditions is affirmative, and we conclude that we are dealing with a well-posed problem. We note that the fact that small changes in input data may cause large changes in solution, does not strictly violate the third Hadamard condition as the solution is still continuous." These results give us new insight into the downward continuation problem that has traditionally been classified as an ill-posed problem.

Regardless of the downward continuation being an ill-posed problem or not, the commonly accepted fact is that it definitely amplifies the errors of the input data.

How the effects of the random errors can be eliminated as much as possible, and to what extent the random errors of the input data affect the determination of geoid vis-à-vis the decreasing size of the grid, needs to be investigated.

Before attempting a solution, the Poisson integral equation has to be discretized. Bjerhammar (1987) defines the discrete boundary value problem as: “A finite number of discrete observations of the gravity anomaly are given on the surface of the Earth. It is wanted to find a solution, that satisfy all given observations and be regular at infinity.” He suggests a Dirac approach which postulates $\Delta g = 0$ for all points on the Bjerhammar sphere with the exception of selected points, where the gravity anomalies are unknown impulses on infinitesimal surface elements. These unknown impulses do not correspond to the physical reality. Whether the Dirac approach can be applied to determine the local geoid needs further research.

Vaníček et al. (1996) treat the gravity anomalies on the geoid as mean values over regular cells in the near-zone, plus the far-zone contribution which can be evaluated by a global geopotential model. The Molodenskii modification of the Poisson kernel is applied in order to reduce the far-zone effect. Its formulation is based on grid-mean values of the gravity anomalies on the Earth surface in order to smooth the gravity field.

Martinec (1996) follows the same approach as Vaníček et al. but uses the spheroidal Poisson kernel and discretizes gravity anomalies as point values. A comparison between the two approaches shows that the point-value solutions are up to five times smaller than the mean-value solutions (Sun and Vaníček, 1998). This is due to the fact that the use of the doubly averaged Poisson kernel in the mean approach makes the Poisson kernel smoother but the solutions rougher. Since different kernels and discretization methods have been proposed, the discretization of the Poisson integral still needs to be studied systematically to find a discrete model most accurate and most efficient from the computational point of view.

The methods for the solution of ill-posed problems include the least-squares collocation (Moritz, 1976, 1980; Rummel et al., 1979) and the regularization techniques (Tikhonov and Arsenin, 1977; Schwarz, 1978; Rummel et al., 1979; Tarantola, 1987; Xu and Rummel, 1992; Rauhut, 1992; Engels et al., 1993). The least-squares collocation technique generates a solution with the minimum norm in the solution space. Its validity to gravity field estimation has been debated for some time because ergodicity³ could not be established. On the other hand, the solution through regularization techniques usually introduces a bias since it strongly depends on the regularization factor and the constraint function that can be chosen in different ways. Any regularization technique aims to suppress or control the sensitive components of the system to the input data and seek a smooth and stable solution, while the sought solution may not possess inherently the property of smoothness and stability.

Martinec (1996) suggests ‘a physical regularization’ in which the high-frequency components of the gravity signals are smoothed and dampened by compensating the topographical masses in an appropriate way. He compares three condensation models and finds that for the region of the Canadian Rocky Mountains, the Airy-Heiskanen condensation performs best in reducing the high-frequency components, while Helmert’s 2nd condensation performs the worst. The smooth condensation model may relatively alleviate the ill-conditioning, but the problem may still be ill-conditioned since random errors in observations affect the entire frequency spectrum.

On the error propagation of downward continuation, Milbert (1999) simulates how synthetic random errors in input data are amplified in the solutions, while Vaníček and Wong (1999) show how standard deviations of input data are amplified from the Earth surface to the geoid. However, the available gravity anomalies we have are usually correlated. The question is how correlated random errors in input data are propagated through the downward continuation. The assumption of statistical

³A stationary random function is called *ergodic* if it has a normal probability function with zero mean and a covariance function that converges to zero as the sampling interval increases indefinitely.

independence may underestimate the errors in the solutions. However this issue is outside the scope of this research.

As far as numerical computation is concerned, we are dealing with a huge system of equations. For example, for an area of $10^\circ \times 10^\circ$ and a grid of $5' \times 5'$, the total number of equations is 14400. With a finer grid and a larger area, the computational difficulty becomes more serious even with the present-day advanced computer systems. Therefore, an efficient algorithm is necessary for the realization of the downward continuation.

In addition to the discrete Poisson downward continuation, the analytical continuation has been widely used for the determination of the geoid associated with the Molodenskii solution (Moritz, 1980; Sideris, 1987; Sideris and Forsberg 1990; Wang, 1988, 1990). It is based on the Taylor series expansion of the gravity anomaly along the plumb line. One question arises: What is the relation between the Poisson continuation and the analytical continuation? Huang et al. (1998) compared the mean Poisson downward continuation to the (point) analytical downward continuation. Numerical results in the Canadian Rocky Mountains show that the analytical downward continuation result differs significantly from that of the mean Poisson downward continuation (22 cm on average). Sideris et al. (1999) find that the differences between the point Poisson and analytical downward continuation reach 25 cm on average for the geoid in the same region. Further studies are needed to systematically compare the two methods through a synthetic approach and establish the relation between the two continuation methods.

Finally, the evaluation of the Helmert gravity anomaly is affected by topography. The use of the constant topographical mass density introduces errors into the downward continuation. Martinec (1993) suggests theoretically that the lateral density variation of topographical masses may affect the geoid at the decimeter level. Pagiatakis et al. (1999) show that the effect can reach 10 *cm* in the Skeena Region British Columbia, and several millimeters in New Brunswick where the terrain is

moderate (hilly) when only the terrain correction is considered. During the period of this research, Kuhn (2000) studied several isostatic compensation models by taking real topographical mass density into account for the regularization of the Earth surface. His numerical results for the area of Baden-Württemberg (South-West Germany) show that the real mass density is needed for the cm-geoid modeling. A systematic study of the effect of the lateral density variation on the downward continuation, and consequently on the geoid is needed to establish a procedure to evaluate and correct for the effect.

1.4 Objectives

The first objective of this research is to develop computational methods for the discrete Poisson downward continuation of the Earth gravity to support the determination of a precise geoid. It is treated in chapters 2-5.

Chapter 2 introduces the basic theory behind Poisson's integral including a description of Dirichlet's problem, the theoretical definition of the downward continuation problem and a discussion of its solvability. A solution in the spherical harmonic form to the inverse Poisson problem is derived.

Chapter 3 addresses the discretization of Poisson Integral. It consists of two parts: (1) the far-zone effect dealing with its formulation, kernel modifications, determination of the size of the near-zone cap and a fast algorithm of the far-zone contribution; (2) discrete Poisson integral equations, discussing three discretization models, and their stability using singular value decomposition (SVD).

Chapter 4 develops methods for stable solutions of the discrete Poisson integral equations. Synthetic fields are used to identify the best discretization model, and to quantify the validity of the regularization techniques. Finally an efficient algorithm for the computation of downward continuation is proposed.

Chapter 5 compares the discrete Poisson downward continuation with the analytical downward continuation. It aims to establish theoretical and numerical relations between the two methods.

Chapter 6 investigates the effect of lateral topographical mass density variation on the gravity reduction and the geoid. It is the second objective of this research. First, the topographical mass density model is developed. Second, mathematical models for the estimation of the direct topographical density effect, the primary indirect topographical density effect and the secondary indirect topographical density effect are formulated. Finally, numerical results over the Canadian Rocky Mountains are presented and discussed.

Chapter 7 summarizes the conclusions drawn from this research. A computational approach for the downward continuation is proposed. Recommendations are made with regard to further studies.

1.5 Contributions

In brief, this research has contributed the following findings and aspects:

- A solution in the spherical harmonic form to the inverse Poisson problem was derived. It is pointed out that the solution of the discrete inverse Poisson problem exists, but may not be unique and stable.
- It was found that the modified spheroidal Poisson kernel significantly reduced the real far-zone contribution over using the unmodified spheroidal Poisson kernel. Furthermore, the standard Poisson kernel works as efficiently as the modified spheroidal Poisson kernel in reducing the real far-zone contribution.
- It was found that Heiskanen and Moritz's (1967) radius condition for the determination of the cap size for downward continuation gives a critical radius of the

near-zone cap that is too small for the determination of the 1-cm geoid while Martinec's (1996) condition gives a radius that is unnecessarily large.

- An efficient algorithm for the evaluation of the far-zone contribution of the Poisson integral was developed. The new algorithm is one order of magnitude faster than the standard algorithm while providing a sufficient accuracy.
- The combined iterative method was proposed to speed up convergence of the solution of the discrete inverse Poisson problem. The truncated singular value decomposition method was introduced to solve the Poisson integral equation. It gives us a discrete solution from the spectral point of view establishing a link to the continuous solution.
- The synthetic tests carried out in this research showed that the mean-mean discrete model of the Poisson integral produced a sufficiently accurate solution when the averaging error was taken in account.
- A block-wise technique was developed to solve the discrete Poisson equation efficiently.
- A software package was developed for the Poisson downward continuation computation. The three discretization models (point-point, point-mean, mean-mean) were implemented in the package.
- Tests with synthetic data and the real Helmert gravity anomalies suggested that the analytical downward continuation was in agreement with the discrete Poisson downward continuation within 10% of the total downward continuation effect. A fast algorithm with the corresponding software was developed to evaluate the analytical downward continuation.
- It was found that an ultra-high degree synthetic global geopotential model constrained to the Kaula-type degree-variance models was too smooth to simulate

the Helmert gravity anomaly, especially in mountainous regions.

- A procedure for the evaluation of the effects of the lateral topographical mass density variation on gravity and geoid was established. Formulae for evaluating standard deviations of the effects were derived.
- Effects of the lateral topographical mass density variation on the geoid height ranged from -7.0 cm to 2.8 cm with a mean of -0.7 cm and an RMS of 1.2 cm in the Canadian Rocky mountains by using the 30'' \times 60'' DEM. The software for evaluating the topographical density effect on the geoid was developed.

Chapter 2

Basic Theory

2.1 Dirichlet's Problem and Poisson's Integral Equation

A function V is called *harmonic* in a region $v \subset \mathfrak{R}^3$ bounded by S if it satisfies Laplace's equation

$$\Delta V = 0 \tag{2.1}$$

at every point of v . The problem of finding the harmonic function from its boundary values on S is called *Dirichlet's problem*, or the first boundary-value problem. *Dirichlet's principle* states: for given boundary values on a Ljapunov surface S , there always exists a harmonic function V that satisfies the given boundary values on S . Furthermore *Stokes's theorem* states that the harmonic function V outside the surface S is uniquely determined by its values on S (Kellogg, 1929; MacMillan, 1930). For example, the gravitational potential of the Earth outside the Earth surface is harmonic. Therefore, the gravitational potential outside the Earth surface can be determined uniquely, given the gravitational potential values at the Earth surface.

While Stokes's theorem guarantees the existence of a unique harmonic function, it doesn't provide the method by which it can be determined from the given boundary

values. In general, for an arbitrary boundary shape, it is difficult to find an analytical form of the solution. A simple shape of a boundary is a spherical surface. An explicit solution of Dirichlet's problem for the exterior of the sphere can be expressed in terms of *Poisson's integral*. It has important applications in physical geodesy, especially in the continuation of the Earth's gravity.

Poisson's integral can be written as (Heiskanen and Moritz, 1967, eqn. 1-89):

$$V(r, \Omega) = \frac{1}{4\pi} \int_{\Omega'} K(r, \psi, R) V(R, \Omega') d\Omega' \quad (2.2)$$

where the Poisson kernel function is expressed as follows

$$K(r, \psi, R) = \frac{R(r^2 - R^2)}{L^3}, \quad (2.3)$$

$$L = (r^2 + R^2 - 2Rr \cos \psi)^{\frac{1}{2}}, \quad (2.4)$$

where L is the distance between (r, Ω) and (R, Ω') , r is the geocentric radius of a point outside the sphere, R is the radius of the sphere, and ψ is the angular distance between geocentric directions Ω and Ω' . In the Poisson integral, the following abbreviation is used to represent the integration over the unit sphere.

$$\int_{\Omega'} d\Omega' = \int_{\lambda'=0}^{2\pi} \int_{\theta'=0}^{\pi} \sin \theta' d\theta' d\lambda' \quad (2.5)$$

Poisson's integral is a special case of Stokes's theorem. In order to apply this integral formula, the sought function must be harmonic above the spherical boundary. In spherical approximation, the gravity anomaly can be expressed as (Heiskanen and Moritz, 1967, eqn. 2-155; Rapp et al., 1991):

$$\Delta g(r, \Omega) = \frac{GM}{Rr} \sum_{n=0}^{\infty} (n-1) \left(\frac{R}{r}\right)^{n+1} \sum_{m=-n}^n C_{nm} Y_{nm}(\Omega) \quad (2.6)$$

where GM is the geocentric gravitational constant, C_{nm} are the fully normalized spherical harmonic coefficients of the geopotential. In addition:

$$Y_{nm}(\Omega) = P_{n|m|}(\cos \theta) \begin{cases} \cos m\lambda & \text{if } m \geq 0 \\ \sin |m|\lambda & \text{if } m < 0 \end{cases} . \quad (2.7)$$

The $P_{n|m}(\cos \theta)$ values are the fully normalized associated Legendre functions of the first kind, n and m are the degree and the order of harmonic series, λ and θ stand for longitude and co-latitude. It can easily be proven that $r\Delta g(r, \Omega)$ is harmonic outside the sphere. Substituting it into eqn. (2.2), Poisson's integral equation for the gravity anomaly can be expressed as

$$\Delta g(r, \Omega) = \frac{R}{4\pi r} \int_{\Omega'} K(r, \psi, R) \Delta g(R, \Omega') d\Omega', \quad (2.8)$$

where $\Delta g(r, \Omega)$ is the gravity anomaly at the point (r, Ω) outside the sphere whereas $\Delta g(R, \Omega')$ represents the gravity anomaly at the point (R, Ω') on the sphere.

Eqn. (2.8) also holds true for the gravity disturbance δg (Hotine, 1969; Vaníček et al., 1996; Sun and Vaníček, 1998). The conclusions drawn from this research will be applicable to the downward continuation of the gravity disturbance δg as well.

Eqn. (2.8) is the basic formula for continuation of the gravity anomaly. This equation tells us that the gravity anomaly outside the sphere is uniquely determined, given its boundary values on its surface.

In eqn. (2.8), the boundary values $\Delta g(R, \Omega')$ are defined on a sphere of radius R , while the boundary values in the geoid determination are needed on the geoid. Therefore, the continuations on the basis of eqn. (2.8) provide spherical approximation results. The maximum downward continuation effect on the geoid in the Canadian Rocky Mountains is smaller than 2 m (Vaníček et al., 1996; Vaníček et al., 1999). Considering the flattening of the Earth ($f \doteq 3 \times 10^{-3}$), the spherical approximation error for the downward continuation will not exceed 1 cm.

2.2 The Inverse Problem and Downward Continuation

The Poisson downward continuation is an inverse problem that represents a cross-disciplinary and challenging subject being encountered in mathematics, science, medicine,

engineering and others. A variety of definitions have been given in outlining the inverse problem. A geophysical definition given by Tarantola (1988) may appropriately be applicable for the Poisson downward continuation:

“Let \mathbf{S} represent a physical system (for instance the whole universe, or a planet, or a quantum particle). Assume that we are able to define a set of model parameters which completely describes \mathbf{S} . These parameters may not all be directly measurable (for instance, the radius of the Earth’s metallic core is not directly measurable). We can operationally define some observable parameters whose actual values hopefully depend on the values of the model parameters. To solve the *forward problem* is to predict the values of the observable parameters, given arbitrary values of the model parameters. To solve the *inverse problem* is to infer the values of the model parameters from given observed values of observable parameters.”

Thus, the forward problem predicts specific facts from a well-defined model, while the inverse problem determines the model from the observed facts. In geodesy, predicting atmospheric effects on GPS measurements from an atmospheric model is a forward problem. Conversely, finding the atmospheric model from GPS measurements is an inverse problem. Since the inverse problem is about the derivation of the system model from specific observations, it is often under-determined due to insufficient observations, instability of the system and experimental uncertainties.

In Poisson’s integral equation (2.8), the gravity anomaly anywhere outside the sphere can be predicted, when the gravity anomaly values $\Delta g(R, \Omega')$ are known on the surface of the sphere. It means that $\Delta g(R, \Omega')$ can be chosen as model parameters for that $\Delta g(r, \Omega)$ outside the sphere. The corresponding inverse problem of solving for $\Delta g(R, \Omega')$ from $\Delta g(r, \Omega)$ is called the downward continuation of the gravity anomaly or the *inverse Poisson problem*. The Poisson problem is routinely used as a closed formula, while the inverse Poisson problem involves the solution of an ill-posed problem. The next section will detail the ill-posed problem.

2.3 Solvability of the Poisson Downward Continuation

The generic form of the Poisson integral equation is called the Fredholm integral equation of the first kind in mathematics, which may be ill-posed due to insufficient data and experimental uncertainties. The concepts of the well-posed and ill-posed problems (Hadamard, 1952; Tikhonov and Arsenin, 1977) can be used to describe and testify to its solvability. Let's consider the following system:

$$B\mathbf{f} = \mathbf{g}, \tag{2.9}$$

where B is an integral or matrix operator, \mathbf{f} is an unknown vector of model parameters in the model space \mathcal{F} and \mathbf{g} is the observation vector in the observation space \mathcal{L} . The problem of determining the solution $\mathbf{f} \in \mathcal{F}$ from the observation vector $\mathbf{g} \in \mathcal{L}$ is said to be well-posed on the pair of normed spaces $(\mathcal{F}, \mathcal{L})$ if the following three conditions are satisfied (Hadamard, 1952; Tikhonov and Arsenin, 1977):

1. For every element $\mathbf{g} \in \mathcal{L}$ there exists a solution $\mathbf{f} \in \mathcal{F}$.
2. The solution is unique.
3. The solution is stable on the spaces $(\mathcal{F}, \mathcal{L})$.

The problem of determining the solution $\mathbf{f} = B^{-1}\mathbf{g}$ in space \mathcal{F} from the data $\mathbf{g} \in \mathcal{L}$ is said to be stable on the spaces $(\mathcal{F}, \mathcal{L})$, if and only if $\mathbf{f} + \delta = B^{-1}(\mathbf{g} + \epsilon)$ such that $|\|\mathbf{f} + \delta\| - \|\mathbf{f}\|| < \delta_1$ for $|\|\mathbf{g} + \epsilon\| - \|\mathbf{g}\|| < \epsilon_1$. ϵ , ϵ_1 , δ and δ_1 are sufficiently small quantities. Problems that do not satisfy the three conditions above are said to be *ill-posed*.

If the space \mathcal{L} is chosen in a “natural” manner for the problem in question, conditions 1 and 2 characterize its mathematical determinacy. Condition 3 is connected with the physical determinacy of the problem, as well as with the possibility of applying numerical methods to solve it on the basis of observations with random errors.

The existence of the solution of the Poisson integral equation can be confirmed from the physical point of view. The quantity being sought represents the gravity anomaly $\Delta g(R, \Omega')$, whose existence is physically justified. From the mathematical point of view, the Picard theorem (Sjöberg, 1979; Groetsch, 1984; Hansen, 1992; Martinec, 1996) defines the condition of existence for the solution of the Fredholm integral equation of the first kind in the continuous case.

The product of the Poisson kernel function of eqn.(2.8) and the term R/r can be expanded into the spherical harmonics series (Heiskanen and Moritz, 1967, eqns. 1-82', 1-88).

$$\frac{R}{r}K(r, \psi, R) = \sum_{n=0}^{\infty} (2n+1)\lambda_n P_n(\cos\psi) = \sum_{n=0}^{\infty} \lambda_n \sum_{m=-n}^n Y_{nm}(\Omega)Y_{nm}(\Omega'), \quad (2.10)$$

where

$$\lambda_n = \left(\frac{R}{r}\right)^{n+2} \quad (\textit{singular - values}). \quad (2.11)$$

This expression is called the *singular value expansion* (SVE) of the Poisson kernel.

The *Picard condition* states that the Poisson integral equation has a solution if and only if

$$\sum_{n=0}^{\infty} \frac{\sigma_n^2}{\lambda_n^2} < \infty \quad (2.12)$$

where

$$\sigma_n^2 = \sum_{m=-n}^n \sigma_{nm}^2, \quad (2.13)$$

$$\sigma_{nm} = \frac{1}{4\pi} \int_{\Omega} \Delta g(r_t, \Omega) Y_{nm}(\Omega) d\Omega, \quad (2.14)$$

σ_n^2 are the *degree-variances* of $\Delta g(r_t, \Omega)$ (Heiskanen and Moritz, 1967, p.259), r_t is the geocentric radius of the observation point on the topography, σ_{nm} are the surface spherical harmonics coefficients of $\Delta g(r_t, \Omega)$. Note that they differ from the spherical harmonics coefficients C_{nm} of the global geopotential model by definition. Coefficients σ_{nm} are derived from the gravity anomaly on the irregular (Earth) surface while C_{nm} are derived from the gravity anomaly on the surface of a sphere. In other words, σ_{nm} are referred to the natural Earth surface while C_{nm} are referred to a sphere with

a chosen radius. Furthermore, the coefficients σ_{nm} have units of acceleration $[LT^{-2}]$, while coefficients C_{nm} are defined as unitless. Eqn. (2.14) can also be defined as the spherical harmonic transform which transforms the gravity anomaly $\Delta g(r_t, \Omega)$ into the harmonic spectral form. Eqn. (2.12) is called the *Picard condition* in the continuous case. To satisfy this condition, the degree-variances σ_n^2 must decay at a rate which can compensate the attenuation of the squares of the singular values λ_n^2 so as to render the sum of eqn. (2.12) finite.

A solution of eqn.(2.8) in the form of the harmonic series can be easily derived as

$$\Delta g(R, \Omega') = \sum_{n=0}^{\infty} \sum_{m=-n}^n \frac{\sigma_{nm}}{\lambda_n} Y_{nm}(\Omega'). \quad (2.15)$$

This series diverges unless the Picard condition holds. It shows clearly that the downward continuation makes the field rougher via an amplification of the spectral components σ_{nm} by a factor λ_n^{-1} (that is greater than 1). It is evident that the high-frequency components of $\Delta g(R, \Omega')$ oscillate more strongly than those of $\Delta g(r_t, \Omega)$.

The existence of a solution for the continuous Poisson integral equation is mathematically interesting. However, whether the solution exists is not so important in practice as it is in theory. Bjerhammar (1964) pointed out that the assumption of a complete continuous gravity coverage at every point of the Earth's surface is unrealistic because we can measure gravity only at discrete points. For the discrete inverse Poisson problem, the upper limit of the degree n in the Picard condition is a finite number depending on the resolution of the discrete data. Thus, the Picard condition is naturally satisfied. This assertion is clearly shown by eqn. (2.12). When n is finite, the spherical harmonic expansion leads to a finite series. Under this circumstance, only a partial solution corresponding to the lower frequency band is obtained.

Uniqueness is often questionable when a theoretical model is applied to solve practical problems even though it is guaranteed in theory. A numerical method associated with a specific data set will produce an approximate solution to the true solution.

The discrete solution depends not only on the data but also on the discretization procedures and solution methods. For example, the solution using mean observed values is different from the one using observed point values. From the numerical point of view, any discrete solution is an approximation of the inverse Poisson problem with respect to a certain frequency band. For instance, the $30' \times 30'$ sampling leads to a solution of up to harmonic degree $n = 360$. The $5' \times 5'$ sampling can generate a solution of up to harmonic degree $n = 2160$. For a given sampling step Δ , the maximum distinguishable frequency band is bounded by $\frac{\pi}{\Delta}$ in terms of the sampling theorem. However, it is still an open question as to which discretization scheme can most closely approximate the physical reality of the gravity corresponding to a certain frequency limit. It is one of the important issues to be treated in this research.

The stability problem arises from the fact that an approximate solution is sought when the observation vector \mathbf{g} is known only approximately and the operator B is derived by a finite number of significant digits. Let $\tilde{\mathbf{g}}$ and \tilde{B} denote approximations of \mathbf{g} and B . Under these conditions, the approximate solution $\tilde{\mathbf{f}} = \tilde{B}^{-1}\tilde{\mathbf{g}}$ depends entirely on the condition of the operator \tilde{B}^{-1} . As an approximate solution, $\tilde{\mathbf{f}}$ is expected to be off by a small “distance” from $\mathbf{f} \in \mathcal{F}$ if $\tilde{\mathbf{g}}$ is off by a small “distance” from $\mathbf{g} \in \mathcal{L}$.

Frequently, operator \tilde{B} is derived such that the system is unstable for two reasons. Either \tilde{B} becomes singular due to round-off errors, or the problem is physically unstable. Under either condition, for a small change in input, we get a large change in the output. One strategy to avoid the former is to increase the precision of the arithmetic operations. There will still be a problem with the latter case that is, that a small input error intrinsically leads to a large output error. The inverse Poisson problem belongs to this class of problems. A small high-frequency error in the observations will be amplified by λ_n^{-1} into the solution of eqn. (2.15). For example, when $H = 2km$ and $n = 2160$ that roughly represents the $5' \times 5'$ grid, the amplification factor is about 2; when $H = 2km$ and $n = 5400$ that roughly represents the $2' \times 2'$

grid, the amplification factor becomes about 5. For the $30'' \times 30''$ grid and $H = 2km$, the amplification factor reaches 880 which will result in a completely wrong result when a systematic noise of high-frequency with a magnitude of $1 mGal$ is present in the observations (see Figure 2.1). It is in this sense that the inverse Poisson problem is said to be ill-posed.

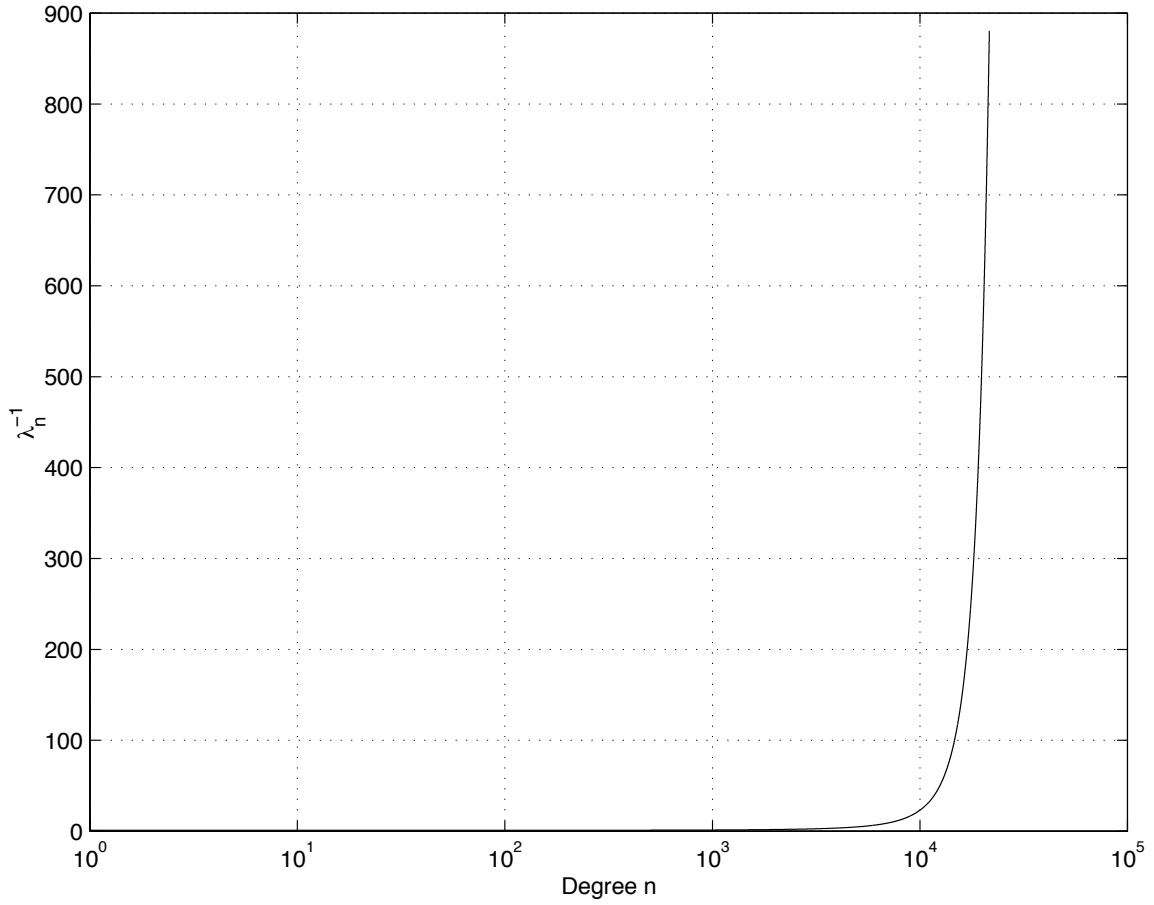


Figure 2.1: λ_n^{-1} versus degree n. $H = 2 km$.

2.4 Summary

Poisson's integral is a solution of Dirichlet's boundary value problem with the boundary values defined on a spherical surface. The generic form of Poisson's integral is called the Fredholm integral equation of the first kind in mathematics. The downward continuation of a harmonic function is defined as the inverse Poisson problem. A spherical harmonic form of solution for the continuous inverse Poisson problem was given. The corresponding discrete solution exists, but is not unique or stable. For a small error in input, we may get a large error in output. The high-resolution solution may contain larger errors if high-frequency errors exist in the data. It is in this sense that the inverse Poisson problem is an ill-posed problem.

Chapter 3

Discretization of Poisson's Integral Equation

Discretization of Poisson's integral equation is a process of approximating the continuous Poisson integral with a discrete form that is expected to best use the available data at discrete points and to efficiently eliminate errors and biases in the practical evaluation of the downward continuation. The discretization must consider the following issues: **a)** evaluation of the far-zone contribution, **b)** modification of the Poisson kernel, **c)** combination of terrestrial data with a satellite geopotential model, **d)** truncation of the Poisson integral and, **e)** discretization of the Poisson integral in the near-zone.

3.1 The Far-Zone Contribution

The Poisson integration converges rapidly with respect to the distance of the integration point from the computation point since its kernel is inversely proportional to the cube of the distance. Its far-zone effect being very small can be evaluated separately by using a global geopotential model. This section includes discussions on the methods for evaluating the *far-zone contribution* (also called the truncation error),

modification of the Poisson kernel, determination of the critical angular radius for the near-zone cap and an algorithm for the evaluation of the far-zone contribution.

3.1.1 Formulation

By analogy to the treatment of Stokes's integral (Molodenskii et al., 1956; Heiskanen and Moritz, 1967; Vaníček and Sjöberg, 1991; Vaníček et al., 1996), the domain of Poisson's integral may be split into two parts: the near-zone and the far-zone. The near-zone is routinely chosen as a spherical cap with an angular radius of ψ_0 , contributing the dominant part of the integral value. The far-zone covers the rest of the spherical surface, merely accounting for a very small part of the integration value. Then, the Poisson integral can be written as

$$\Delta g(r, \Omega) = \frac{R}{4\pi r} \int_{\Omega'_0} K(r, \psi, R) \Delta g(R, \Omega') d\Omega' + F_{\Delta g}(r, \Omega), \quad (3.1)$$

where

$$F_{\Delta g}(r, \Omega) = \frac{R}{4\pi r} \int_{\Omega' - \Omega'_0} K(r, \psi, R) \Delta g(R, \Omega') d\Omega'. \quad (3.2)$$

where Ω'_0 and $\Omega' - \Omega'_0$ indicate the near- and the far- zones, respectively. Eqn. (3.2) represents the far-zone contribution. Due to the lack of global gravity coverage, it is usually evaluated from a global geopotential model such as EGM96 (Lemoine et al., 1998) by using the Molodenskii-type harmonic expansion technique

$$F_{\Delta g}(r, \Omega) = \frac{R\gamma}{2r} \sum_{n=2}^{\infty} (n-1) Q_n(H, \psi_0) \sum_{m=-n}^n C_{nm} Y_{nm}(\Omega), \quad (3.3)$$

where

$$Q_n(H, \psi_0) = \int_{\psi_0}^{\pi} K(r, \psi, R) P_n(\cos \psi) \sin \psi d\psi \quad (3.4)$$

are called the *truncation error coefficients*, and $H = r - R$.

Series (3.3) converges more rapidly than the harmonic series for the gravity anomaly since the short-wavelength components are practically eliminated from it by separating the near-zone, which mainly accounts for the short-wavelength components.

Therefore, the far-zone effect may be estimated with sufficient accuracy by a global geopotential model.

It has become standard practice to use the combined technique in the determination of the geoid, i.e., terrestrial data are used in combination with a satellite-only geopotential model. The low-frequency part of the geoid is derived from the satellite-only solution, while the high-frequency part of it is computed from the terrestrial gravity data. As a matter of fact, the satellite solution provides homogeneous long-wavelength components but no local details, while the terrestrial data give the local details but the long-wavelength components are biased because of the limited regional distribution. The combination of the satellite solution with the terrestrial gravity data promises the best solution for the geoid. Furthermore, the removal of the low-frequency components from the gravity anomaly at the Earth surface significantly reduces the far-zone contribution, which is dominated by long-wavelength components for both the downward continuation and the subsequent Stokes integration. Using eqn.(3.1), the high-degree (high-frequency) component of Δg can be written as

$$\Delta g^l(r, \Omega) = \frac{R}{4\pi r} \int_{\Omega_0} K(r, \psi, R) \Delta g^l(R, \Omega') d\Omega' + F_{\Delta g}^l(r, \Omega), \quad (3.5)$$

where K corresponds to the standard Poisson kernel. Superscript l indicates components above degree l of geopotential harmonics. Similarly, the far-zone contribution in eqn. (3.5), as it now contains only high-degree terms, can be written (cf. eqn.(3.3))

as

$$F_{\Delta g}^l(r, \Omega) = \frac{R\gamma}{2r} \sum_{n=l+1}^{\infty} (n-1) Q_n(H, \psi_0) \sum_{m=-n}^n C_{nm} Y_{nm}(\Omega), \quad (3.6)$$

where the index n now starts from $l+1$.

One may notice from the spectral point of view that eqn. (3.5) is not correct as the standard Poisson kernel K contains all frequencies while the quantities convolved with, namely $\Delta g^l(R, \Omega)$, are band-limited (high-frequency content).

Splitting the integral of eqn. (3.5) into two bands, gives

$$\begin{aligned} \frac{R}{4\pi r} \int_{\Omega'_0} K(r, \psi, R) \Delta g^l(R, \Omega') d\Omega' &= \frac{R}{4\pi r} \int_{\Omega'_0} K_l(r, \psi, R) \Delta g^l(R, \Omega') d\Omega' \\ &+ \frac{R}{4\pi r} \int_{\Omega'_0} K^l(r, \psi, R) \Delta g^l(R, \Omega') d\Omega', \end{aligned} \quad (3.7)$$

where

$$K_l(r, \psi, R) = \sum_{n=0}^l (2n+1) \left(\frac{R}{r}\right)^{n+1} P_n(\cos \psi), \quad (3.8)$$

$$K^l(r, \psi, R) = K(r, \psi, R) - K_l(r, \psi, R). \quad (3.9)$$

If we want to be spectrally correct when using eqn. (3.5), only the second term on the right-hand side of eqn. (3.7) should be used, which means that the first would be arbitrarily set to zero which would violate the orthogonality relation. In eqn. (3.5), the first l degrees of terms of the standard Poisson K are orthogonal to Δg^l globally, i.e.,

$$\frac{R}{4\pi r} \int_{\Omega'_0} K_l(r, \psi, R) \Delta g^l(R, \Omega') d\Omega' + \frac{R}{4\pi r} \int_{\Omega' - \Omega'_0} K_l(r, \psi, R) \Delta g^l(R, \Omega') d\Omega' = 0, \quad (3.10)$$

However, none of the terms on the left-hand side of eqn.(3.10) is equal to zero, and both terms are included in the near-zone and the far-zone contributions. Therefore eqns. (3.5) and (3.6) do not correspond to the ‘real’ (or pure) far-zone contribution for Δg^l from the spectral point of view.

Similar to the Stokes integral, the convergence of eqn. (3.6) strongly depends on the truncation coefficients Q_n , which are functions of the kernel $K(r, \psi, R)$ and the angular radius of the near-zone cap ψ_0 . Several treatments to the Stokes kernel have been proposed, firstly to make the far-zone effect disappear more rapidly, and secondly to also eliminate the dependency of the far-zone effect on high degrees of the erroneous geopotential coefficients (Molodenskii et. al, 1962; Meissl, 1971; Vaníček and Kleusberg, 1987; Sjöberg, 1984, 1991; Vaníček and Sjöberg, 1991; Featherstone et. al, 1998). Among various treatments, Vaníček and Kleusberg’s (1987) modification has been applied to Poisson’s kernel (Vaníček et al., 1996) to reduce the real far-zone contribution by using the spheroidal Poisson kernel (Martinec, 1996).

Following Wong and Gore's (1969) idea, the spheroidal Poisson kernel can be constructed as (Martinec, 1996)

$$K^{l, S}(r, \psi, R) = K^l(r, \psi, R). \quad (3.11)$$

This kernel can act as a filter to eliminate the long-wavelength residuals in Δg^l due to exclusion of the first l degrees of terms of K . By using it, the far-zone contribution becomes

$$F_{\Delta g}^{l, S}(r, \Omega) = \frac{R\gamma}{2r} \sum_{n=l+1}^{\infty} (n-1)Q_n^S(H, \psi_0) \sum_{m=-n}^n C_{nm}Y_{nm}(\Omega), \quad (3.12)$$

where

$$Q_n^S(H, \psi_0) = \int_{\psi_0}^{\pi} K^{l, S}(r, \psi, R)P_n(\cos \psi) \sin \psi d\psi. \quad (3.13)$$

The $F_{\Delta g}^{l, S}$ represents the real far-zone contribution for Δg^l since the first l -degree terms K_l have been removed from the standard Poisson kernel K^l .

Using Vaníček and Kleusberg's (1987) modification method, the modified spheroidal Poisson kernel is written as (Vaníček et al., 1996)

$$K^{l, MS}(r, \psi, R) = K(r, \psi, R) - \sum_{n=0}^l \frac{2n+1}{2} t_n(H, \psi_0) P_n(\cos \psi). \quad (3.14)$$

The far-zone contribution becomes

$$F_{\Delta g}^{l, MS}(r, \Omega) = \frac{R\gamma}{2r} \sum_{n=l+1}^{\infty} (n-1)Q_n^{MS}(H, \psi_0) \sum_{m=-n}^n C_{nm}Y_{nm}(\Omega), \quad (3.15)$$

where

$$Q_n^{MS}(H, \psi_0) = \int_{\psi_0}^{\pi} K^{l, MS}(r, \psi, R)P_n(\cos \psi) \sin \psi d\psi. \quad (3.16)$$

The modified spheroidal Poisson kernel $K^{l, MS}$ is created to minimize the real far-zone contribution $F_{\Delta g}^{l, S}$ for Δg^l by introducing the *modified Poisson kernel coefficients* $t_n(H, \psi_0)$ (Vaníček et. al, 1996). Table 3.1 lists the coefficients from degree 0 to degree 20. It can be found that the first l terms of the standard Poisson kernel K are modified by less than 4% at the most. This implies that the standard Poisson kernel K tends to

Table 3.1: The modified Poisson kernel coefficients $t_n(H, 1^\circ)$.

Degree	1000 m	2000 m	3000 m	4000 m
0	0.183049E-01	0.365995E-01	0.548793E-01	0.731400E-01
1	0.179937E-01	0.359772E-01	0.539461E-01	0.718959E-01
2	0.176852E-01	0.353604E-01	0.530210E-01	0.706626E-01
3	0.173794E-01	0.347489E-01	0.521040E-01	0.694402E-01
4	0.170764E-01	0.341429E-01	0.511952E-01	0.682286E-01
5	0.167760E-01	0.335423E-01	0.502944E-01	0.670278E-01
6	0.164784E-01	0.329471E-01	0.494017E-01	0.658378E-01
7	0.161834E-01	0.323573E-01	0.485172E-01	0.646587E-01
8	0.158911E-01	0.317728E-01	0.476407E-01	0.634903E-01
9	0.156016E-01	0.311938E-01	0.467723E-01	0.623327E-01
10	0.153147E-01	0.306202E-01	0.459120E-01	0.611859E-01
11	0.150305E-01	0.300519E-01	0.450598E-01	0.600499E-01
12	0.147490E-01	0.294890E-01	0.442157E-01	0.589247E-01
13	0.144702E-01	0.289315E-01	0.433796E-01	0.578102E-01
14	0.141941E-01	0.283794E-01	0.425516E-01	0.567065E-01
15	0.139206E-01	0.278326E-01	0.417316E-01	0.556134E-01
16	0.136499E-01	0.272912E-01	0.409197E-01	0.545312E-01
17	0.133818E-01	0.267551E-01	0.401158E-01	0.534596E-01
18	0.131164E-01	0.262244E-01	0.393199E-01	0.523987E-01
19	0.128536E-01	0.256990E-01	0.385320E-01	0.513485E-01
20	0.125935E-01	0.251789E-01	0.377521E-01	0.503090E-01

reduce the real far-zone contribution $F_{\Delta g}^{l,S}$ for Δg^l as the modified spheroidal Poisson kernel $K^{l,MS}$ is expected to do.

Figures 3.1 and 3.2 show the three types of the Poisson kernel values against the spherical distance ψ over the near-zone and the far-zone. The differences between K and $K^{l,MS}$ are too small to be considered. On the other hand, $K^{l,S}$ possesses considerably more power than K and $K^{l,MS}$ over the far-zone.

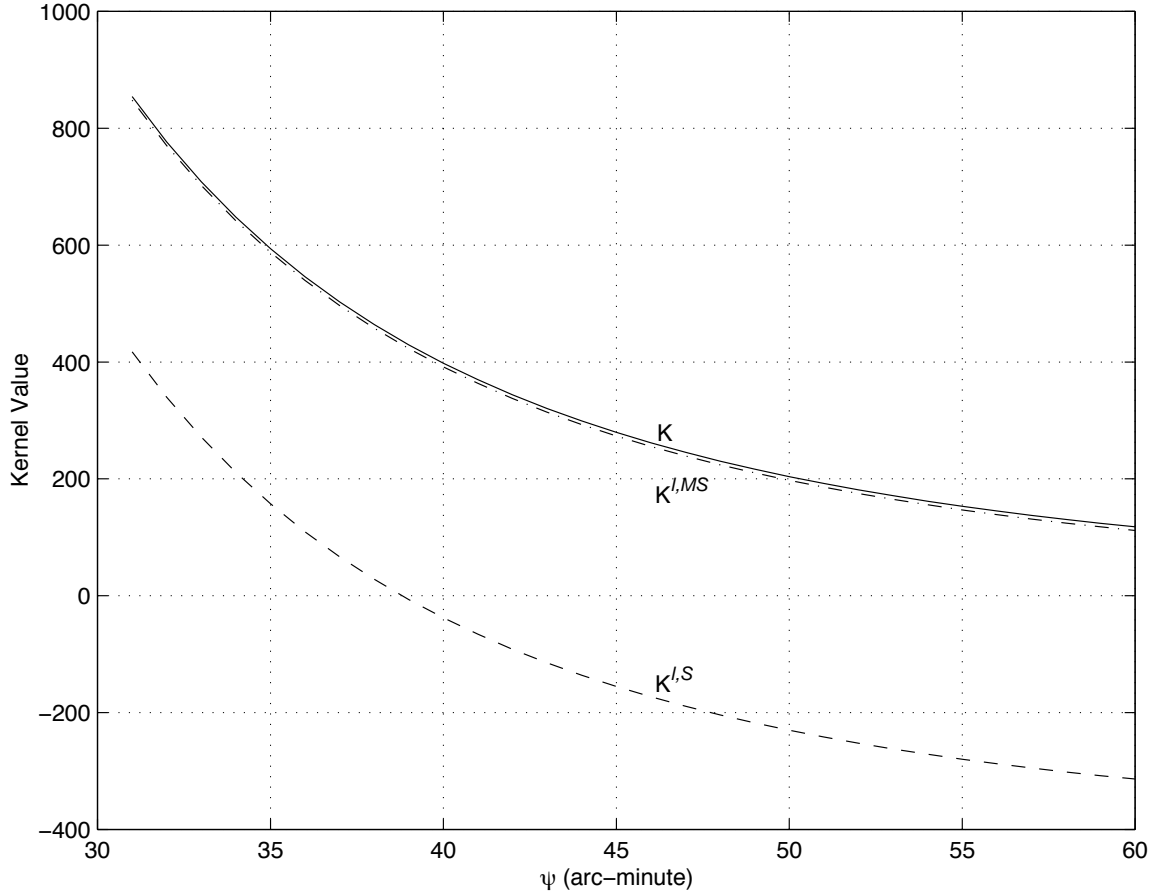


Figure 3.1: K , $K^{l,S}$ and $K^{l,MS}$ vs. ψ ($30' - 60'$). $H = 2$ km.

The standard deviation of the far-zone contribution can be derived from eqns.

¹Vaniček, 2000. personal communication.

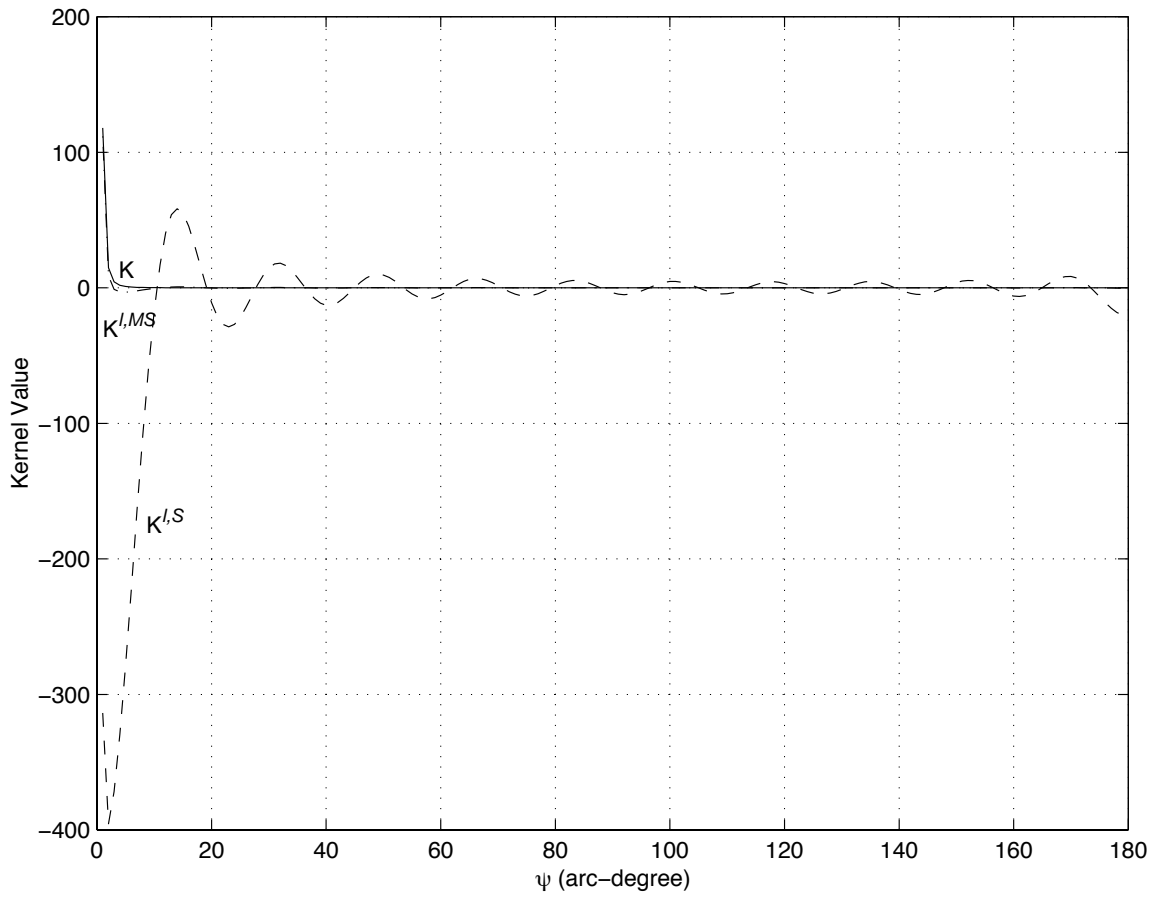


Figure 3.2: K , $K^{l,S}$ and $K^{l,MS}$ vs. ψ ($1^\circ - 180^\circ$). $H = 2$ km.

(3.6),(3.12) and (3.15) by propagation of variance as

$$m_F^I(r, \Omega) = \frac{R\gamma}{2r} \left(\sum_{n=l+1}^{\infty} (n-1)^2 (Q_n^I)^2(H, \psi_0) \sum_{m=-n}^n dC_{nm}^2 Y_{nm}^2 \right)^{\frac{1}{2}}, \quad (3.17)$$

where I indicate the type of kernel in use, and dC_{nm} are the standard deviations of the geopotential model coefficients.

3.1.2 Standard vs. Modified Kernels

The modified spheroidal Poisson kernel has been constructed as an improvement to the standard Poisson kernel in reducing the far-zone contribution. What is the efficiency of the improvement?

Figure 3.3 shows the truncation error coefficients of degree 21 to degree 360 for the standard, spheroidal and modified spheroidal Poisson kernels K , $K^{l, S}$ and $K^{l, MS}$ (Martinec, 1996; Vaníček et al., 1996). In the computation, $\psi_0 = 1^\circ$ and the 2 km height are assumed. The Q_n^S spectrum intersects with Q_n and Q_n^{MS} at about degree 220. For degrees smaller than 220, the Q_n^S are significantly larger than Q_n^{MS} . It suggests that the modified spheroidal Poisson kernel does reduce the real far-zone contribution for Δg^l , as expected. On the other hand, there are merely minor differences between Q_n and Q_n^{MS} indicating that the standard Poisson kernel performs almost as efficiently as the modified spheroidal Poisson kernel in reducing the real far-zone contribution for Δg^l . Figure 3.4 further demonstrates that the far-zone contribution of K displays an indistinguishable difference from the one of $K^{l, MS}$. At the same time, the real far-zone contribution for Δg^l is remarkably larger than the minimized one. Therefore, in view of reducing the far-zone contribution, $K^{l, S}$ should be avoided, while the standard Poisson kernel K may be used as an alternative to the modified spheroidal Poisson kernel.

Figures 3.4 and 3.5 also suggest that the far-zone contribution is precise enough compared to its standard deviation. It means that the current available geopotential

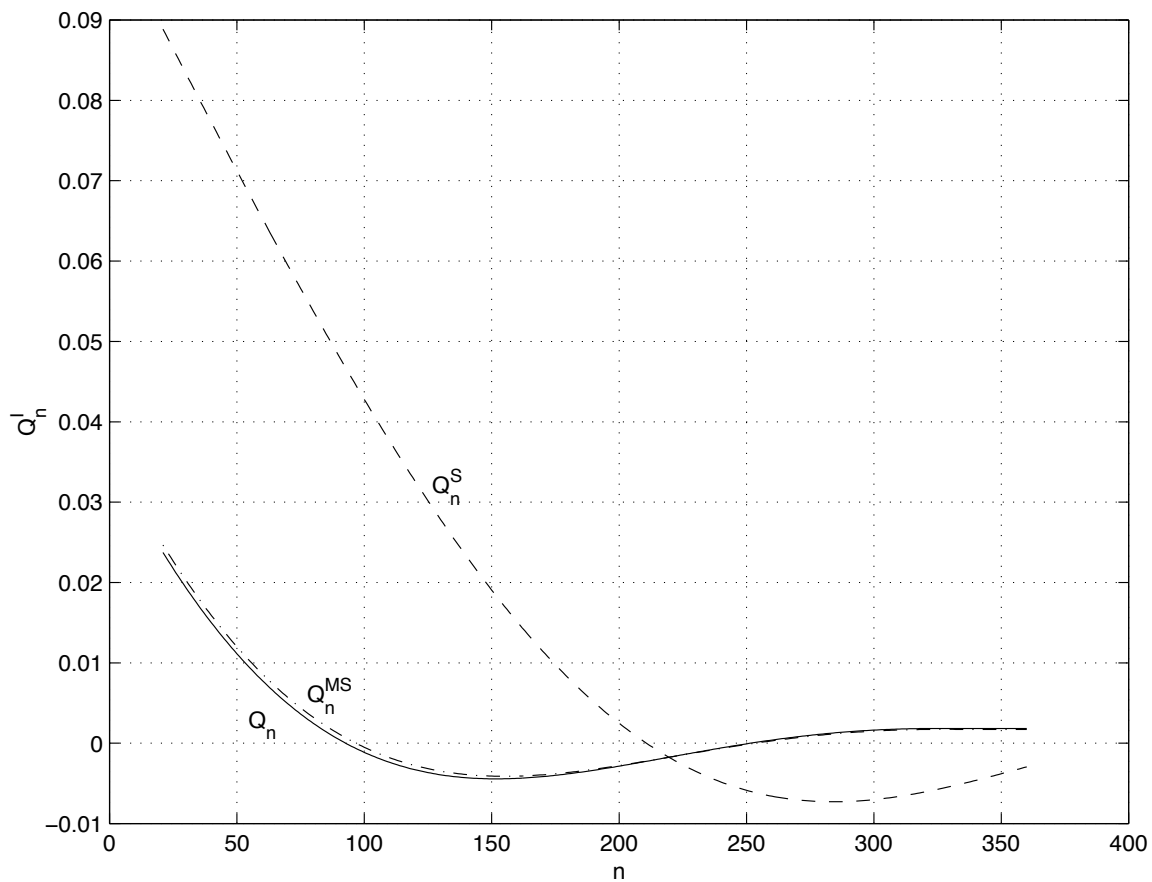


Figure 3.3: The truncation error coefficients Q_n^I . $\psi_0 = 1^\circ$, $H = 2$ km.

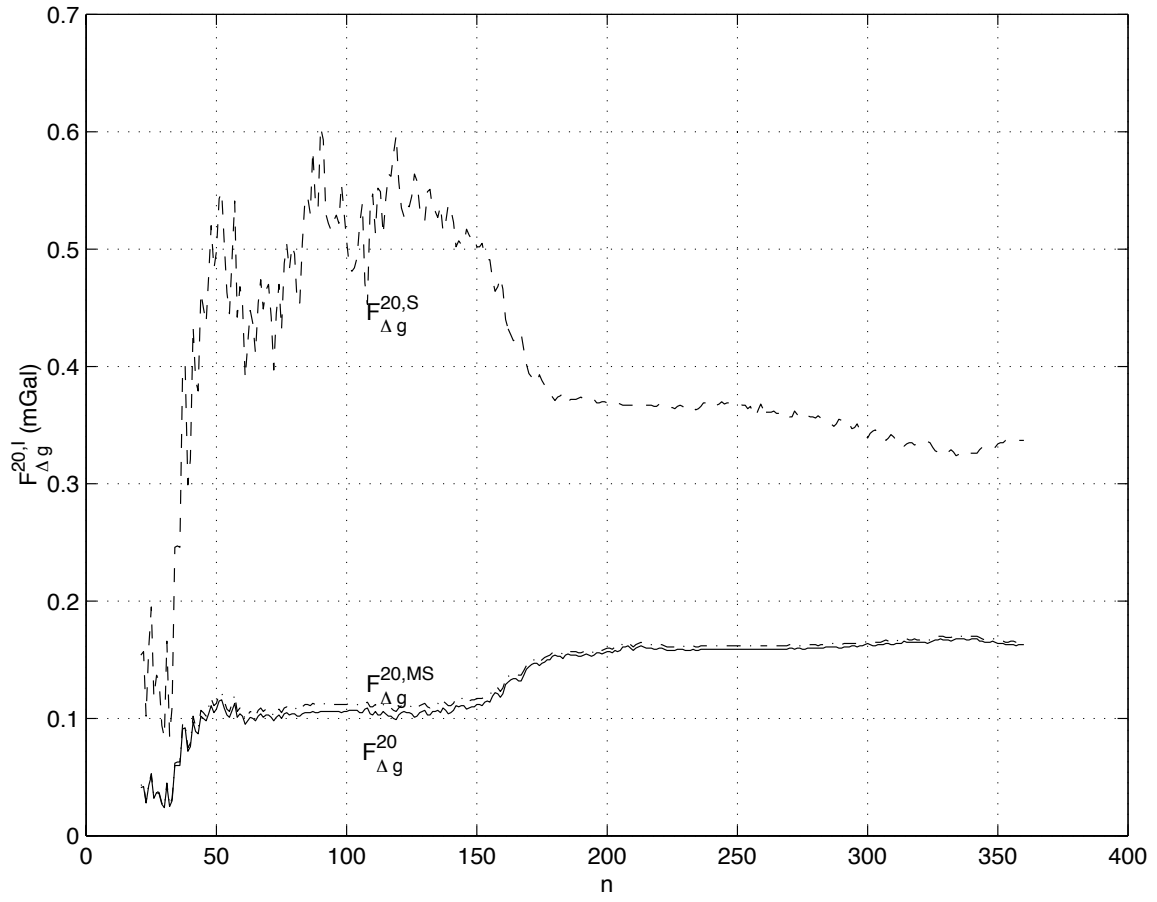


Figure 3.4: The far-zone contributions $F_{\Delta g}^{l,I}$ vs. degree n . $\psi_0 = 1^\circ$, $H = 2$ km.

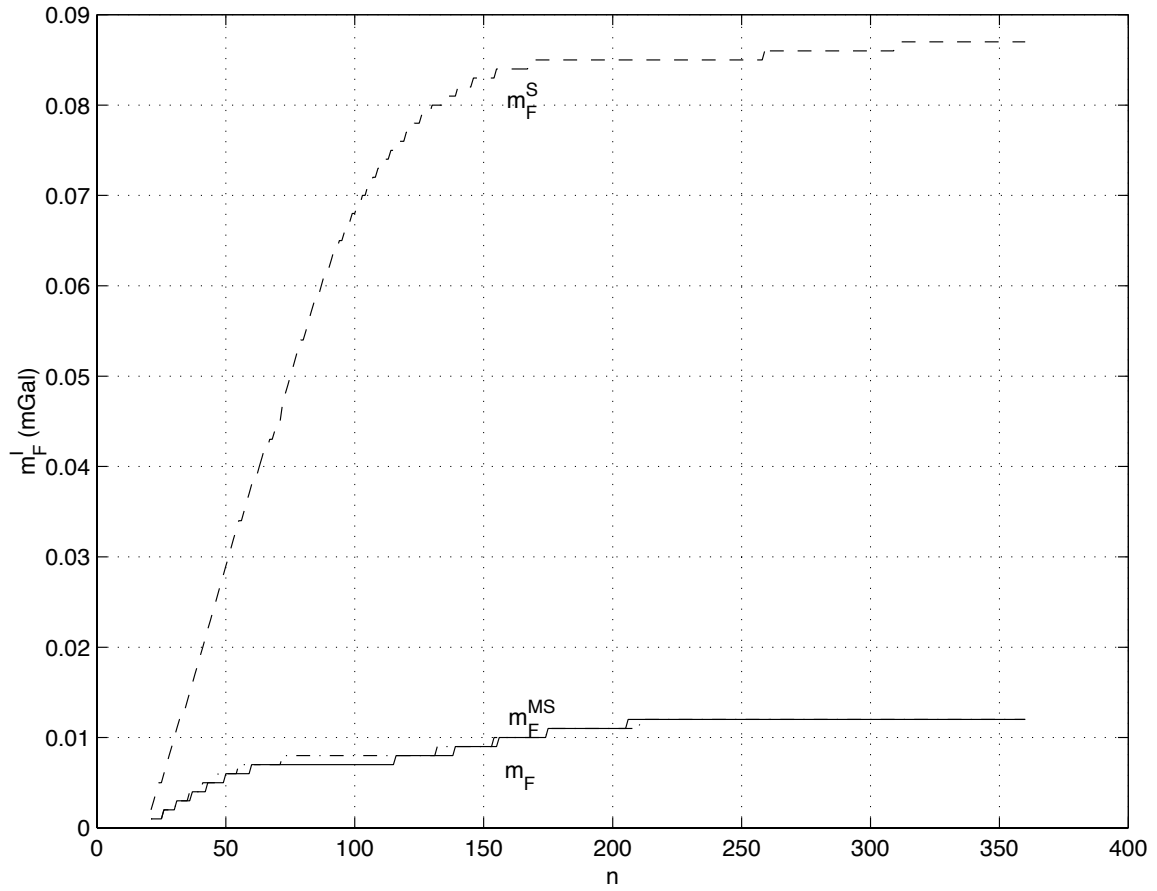


Figure 3.5: The standard deviation m_F^I vs. degree n . $\psi_0 = 1^\circ$, $H = 2$ km.

models are capable of providing an accurate estimation for the far-zone contribution when the 1-degree cap is chosen for a point at an elevation of 2 km. In other words, the far-zone contribution based on the current global geopotential model will improve the accuracy of the downward and upward continuation computations. Furthermore, the far-zone contribution displays a good convergence at lower degrees for all three kernels. After about degree 180, it shows negligible changes suggesting that the far-zone contribution can be evaluated from a global geopotential model taken to degree 180. This conclusion is consistent with Sun and Vaníček's (1998) one based on the results from GFZ93a.

Figure 3.6 shows the far-zone contribution effect on the geoid over the Rocky Mountains. In this region, the far-zone contribution to the geoid varies from $-1.1cm$ to $1.1cm$ in the geoid height.

3.1.3 Determination of The Critical Angular Radius of the Near-Zone Cap

The number of non-zero coefficients in a discrete Poisson integral equation depends on the spherical radius ψ_0 of the near-zone cap. The larger the radius ψ_0 is, the larger the number will be for a fixed grid step. Therefore, we wish to choose the spherical radius of the cap to be as small as possible to reduce the number of coefficients to be evaluated without compromising the accuracy of the downward continuation.

The criterion for determining the critical radius of the near-zone cap is that the far-zone contribution be accurately evaluated or be small enough to be considered negligible. If we assume $\overline{\Delta g}$ as the mean of the gravity anomalies over the far-zone, then by substituting it into eqn.(3.2) the far-zone contribution reduces to

$$F_{\Delta g}(r, \Omega) = \frac{R\overline{\Delta g}}{2r} \int_{\psi_0}^{\pi} K(r, \psi, R) \sin \psi d\psi. \quad (3.18)$$

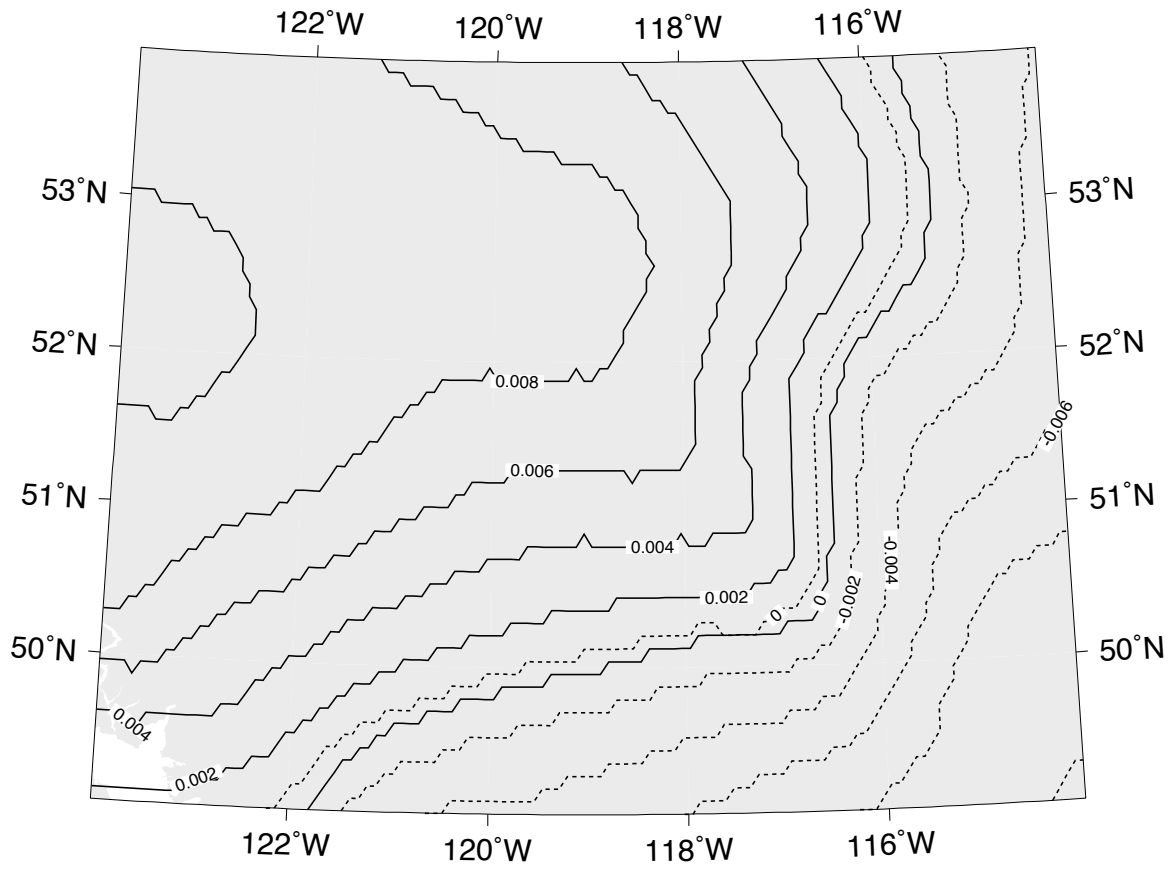


Figure 3.6: The far-zone contribution effect on geoid in the Rocky Mountains. $\psi_0 = 1^\circ$. Contour interval: 0.002 m.

We can easily get

$$F_{\Delta g} = \frac{R(r - R)}{2r^2} \left[\frac{R + r}{L(r, \psi_0, R)} - 1 \right] \overline{\Delta g} \doteq \frac{H}{L(R, \psi_0, R)} \overline{\Delta g}. \quad (3.19)$$

From this equation, it is easily seen that L (vs. eqn. (2.4)) must be chosen in such a way that it makes the ratio of H to L a constant if we wish to keep the far-zone contribution at the same small negligible magnitude at different elevations. On the other hand, the global mean value $\overline{\Delta g}$ of the $1^\circ \times 1^\circ$ free-air gravity anomalies used in developing EGM96 (Lemoine et al., 1996) is -0.24 mGal. Vaníček (2000, personal communication) pointed out that the reference ellipsoid appears 80 cm smaller rendering non-zero global mean. If this value is assumed for the far-zone, the far-zone contribution is negligibly small when L is chosen as large as 10 times H^0 . When we use the Poisson downward continuation, we must transform the gravity anomalies into a model space such as the Helmert space where the disturbing potential is harmonic above the geoid. If we transform the gravity anomalies in such a way so that their global mean is close to zero, the far-zone contribution tends to be small enough to be neglected. Otherwise, the far-zone contribution has to be taken into account.

An immediate question arises however: What is the critical ratio between the elevation of the computation point and the cap radius when the far-zone contribution needs to be evaluated? Heiskanen and Moritz (1967) suggest extending the integration only as far as 10 times the elevation if an accuracy of $1mGal$ is targeted in the upward and downward continuation. Martinec (1996) suggests that the ratio should satisfy the following condition

$$\frac{H}{L(r, \psi_0, R)} < \left(\frac{H}{R} \right)^{\frac{1}{2}}. \quad (3.20)$$

Condition (3.20) implies that the near-zone must extend to at least 1° in the Rocky Mountains.

As shown in Section 3.1.2, the far-zone contribution must be taken into consideration when a cm-geoid is targeted. Since the far-zone contribution is routinely evaluated through a global geopotential model, its accuracy depends on the accuracy

of the geopotential model. Therefore, the critical radius must be determined in terms of the accuracy of the geopotential model in use, which in turn is determined by the accuracy of the model coefficients and the maximum degree of it. Neither Heiskanen and Moritz's condition, nor Martinec's one take the accuracy of the model into consideration. Thus, they may lead to a cap radius either too large, or too small for evaluation of the far-zone contribution.

Presently, EGM96 (Lemoine, 1996) represents one of the best global geopotential models available. Its maximum degree is 360. When EGM96 is used to estimate the far-zone contribution, the critical radius must be determined in accordance with the accuracy of the model. Eqns. (3.3) and (3.17) show that the far-zone contribution and its standard deviation are dependent on the truncation error coefficients Q_n , the coefficients C_{nm} and their standard deviations dC_{nm} , and the maximum degree n .

Three different cap radii of 1° , 0.5° and 0.25° have been chosen to verify the validity of Heiskanen and Moritz's and Martinec's conditions. The 1° cap corresponds to the latter condition, while the 0.25° cap approximately meets the former one. Figure 3.7 shows that the truncation error coefficients Q_n for the 0.25° cap are significantly greater than Q_n for the 0.5° and 1° caps for $n < 360$. The coefficients Q_n for the 0.5° cap are larger than those for the 1° cap for $n < 210$. These features imply that the far-zone contribution is quite sensitive to the cap radius even though the ratio of the elevation to the cap radius is greater than 10. Figure 3.8 shows that the far-zone contributions for the 1° and 0.5° caps approach constant values. Furthermore, we find that the estimates of the far-zone contribution for the 1° and 0.5° caps are precise while that for the 0.25° cap may be completely wrong (v.s. Figures 3.8 and 3.9). Therefore, when EGM96 is used to estimate the far-zone contribution, Heiskanen and Moritz's condition may give a radius too small for a 1-cm geoid. On the other hand, Martinec's condition may give a radius unnecessarily large. Figures 3.7, 3.8 and 3.9 also imply that the 0.5° may be chosen as the near-zone cap radius in mountainous areas where the elevation doesn't exceed 2 km.

In Chapter 4, a synthetic test will be used to verify whether the 0.5° cap is large enough for the evaluation of the far-zone contribution at an accuracy of 1 cm.

3.1.4 An Efficient Algorithm of the Far-Zone Contribution

Rizos (1979) devised an efficient computer technique for the evaluation of gravity parameters such as T and Δg from a set of the spherical harmonic series. The technique is applicable only when the geopotential is not a function of height. Since the far-zone contribution under consideration refers to a point at the Earth surface, it is height-dependent. Rizos's technique is no longer applicable directly. An efficient algorithm for the evaluation of the far-zone contribution is thus developed in the sequel.

First, let us write the far-zone contribution in the spherical harmonic series form with the maximum degree k ,

$$F_{\Delta g}(H, \Omega) = \frac{R\gamma}{2r} \sum_{n=2}^k (n-1) Q_n(H, \psi_0) \sum_{m=0}^n (c_{nm} \cos m\lambda + d_{nm} \sin m\lambda) P_{nm}(\cos \theta). \quad (3.21)$$

By reversing the summation order, eqn.(3.21) can be expressed as

$$F_{\Delta g}(H, \Omega) = \frac{R\gamma}{2r} \sum_{m=0}^k \left[\cos m\lambda \sum_{n=m}^k (n-1) Q_n c_{nm} P_{nm} + \sin m\lambda \sum_{n=m}^k (n-1) Q_n d_{nm} P_{nm} \right]. \quad (3.22)$$

The longitude at all the points in a row of equally spaced points is given by

$$\lambda = \lambda_0 + j\Delta\lambda, \quad (3.23)$$

where $\Delta\lambda$ is the grid spacing. Then we have

$$\cos m\lambda = \cos m\lambda_0 \cos mj\Delta\lambda - \sin m\lambda_0 \sin mj\Delta\lambda, \quad (3.24)$$

$$\sin m\lambda = \sin m\lambda_0 \cos mj\Delta\lambda + \cos m\lambda_0 \sin mj\Delta\lambda. \quad (3.25)$$

Substituting the two expressions above into eqn. (3.22), we get

$$F_{\Delta g}(H, \Omega) = \frac{R\gamma}{2r} \sum_{m=0}^k [C_\alpha(m, H, \theta) \cos mj\Delta\lambda + C_\beta(m, H, \theta) \sin mj\Delta\lambda], \quad (3.26)$$

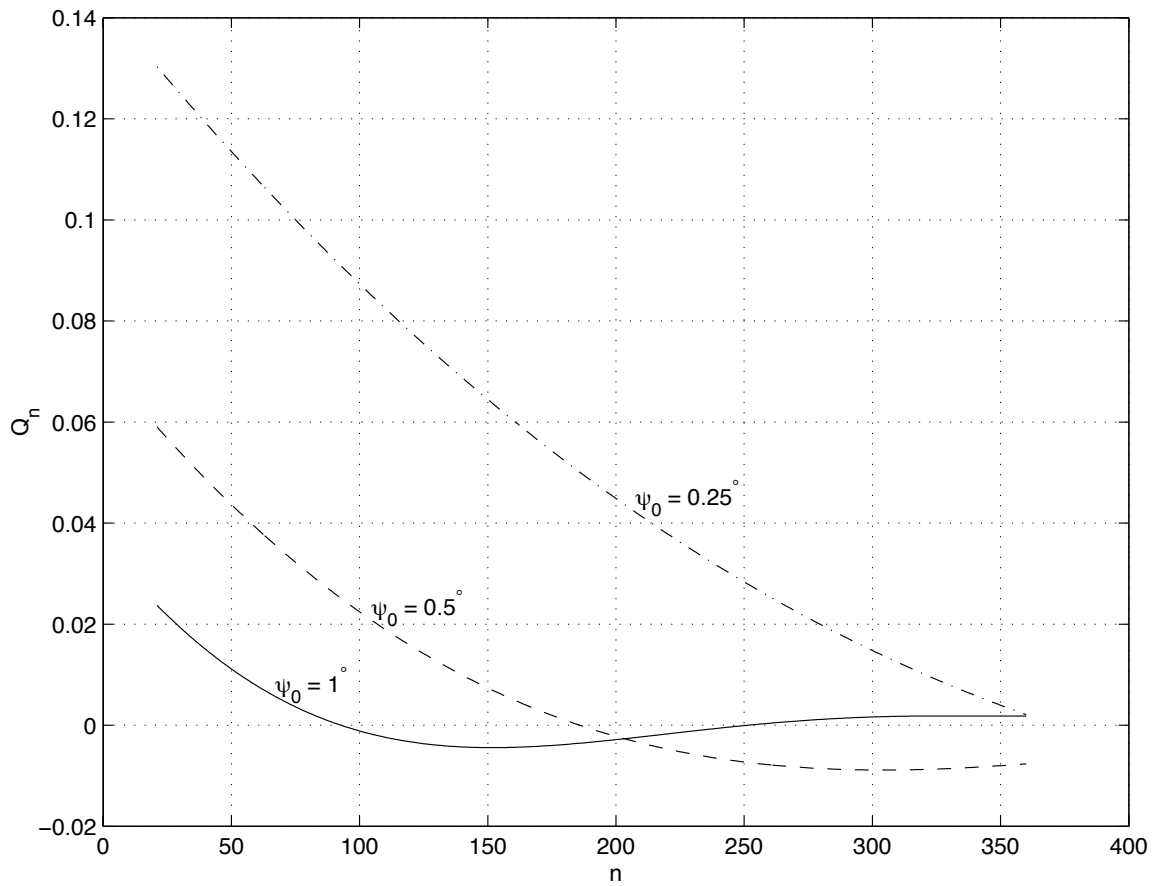


Figure 3.7: The truncation error coefficients Q_n of the standard Poisson kernel K for different radii ψ_0 . $H = 2$ km.

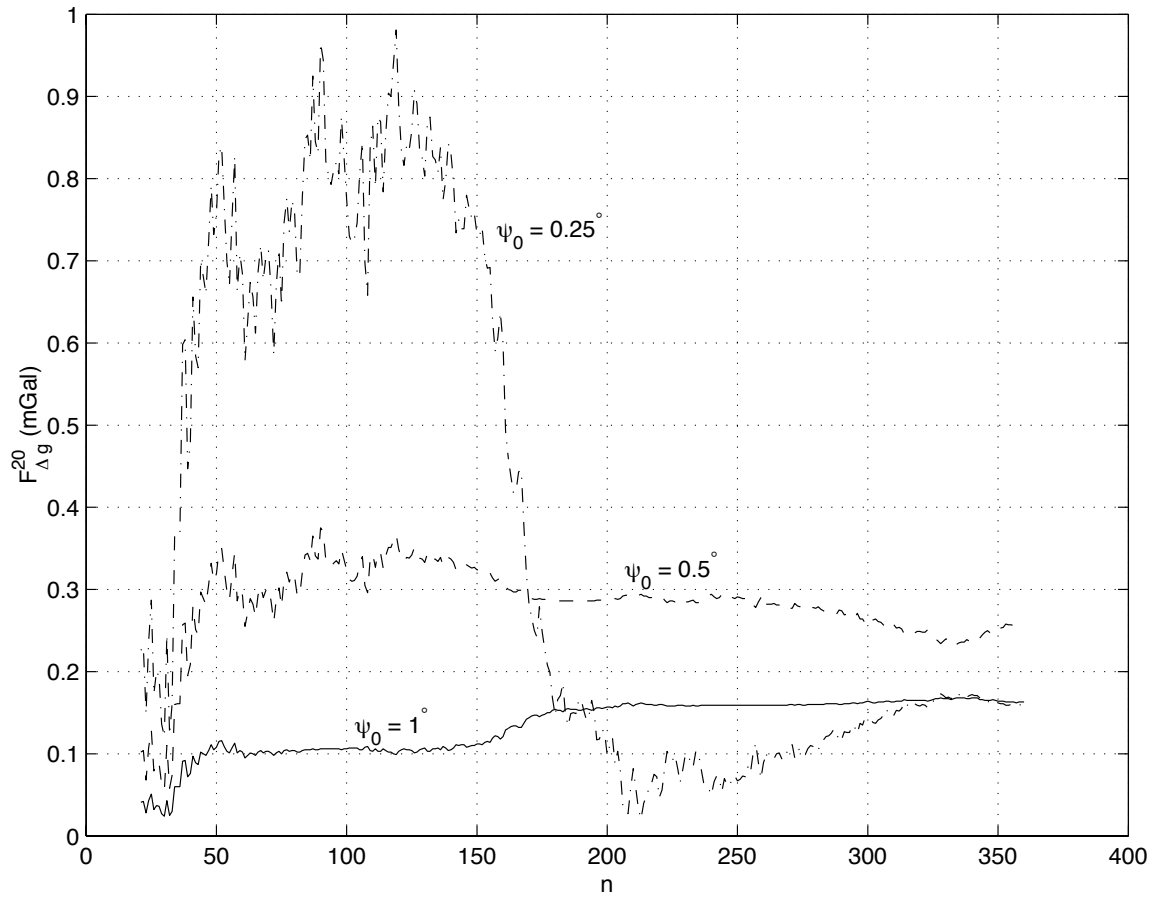


Figure 3.8: The far-zone contributions $F_{\Delta g}^{20}$ for different radii ψ_0 . $H = 2$ km.

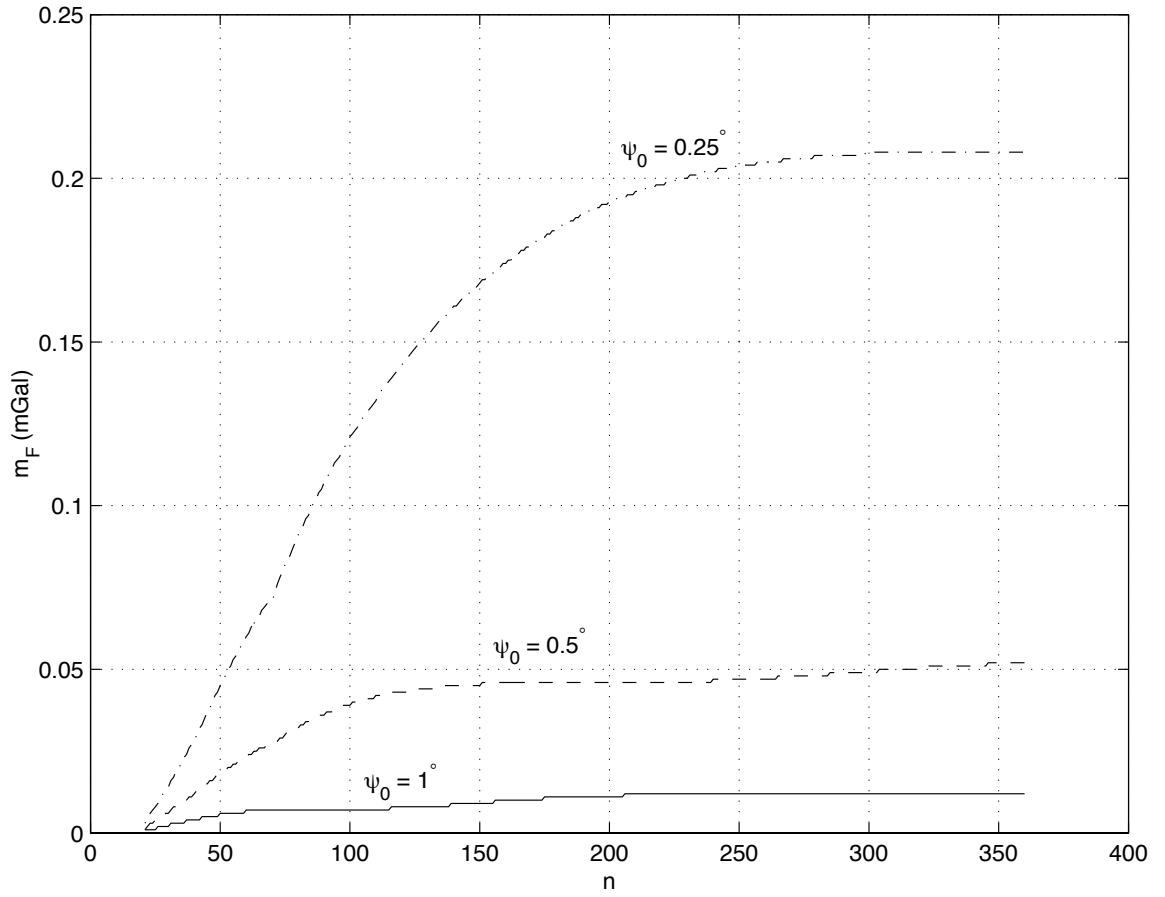


Figure 3.9: The standard deviations of the far-zone contributions m_F for different radii ψ_0 . $H = 2$ km.

where

$$C_\alpha(m, H, \theta) = \sum_{n=m}^k [(n-1)Q_n (c_{nm}P_{nm} \cos m\lambda_0 + d_{nm}P_{nm} \sin m\lambda_0)], \quad (3.27)$$

$$C_\beta(m, H, \theta) = \sum_{n=m}^k [(n-1)Q_n (-c_{nm}P_{nm} \sin m\lambda_0 + d_{nm}P_{nm} \cos m\lambda_0)]. \quad (3.28)$$

It is eqn. (3.26) that makes an efficient evaluation of spherical harmonics possible. When H and θ are both constant, the coefficients C_α and C_β are functions of the order m , which is independent of longitude. Therefore, for points at the same latitude they are only evaluated once. The double summation in eqn.(3.21) reduces to the single summation in eqn.(3.26). The computational efficiency is one order of magnitude higher than the standard method when a large number of points of the same latitude need be evaluated.

For the evaluation of the far-zone contribution under consideration, both C_α and C_β are height-dependent. This means that they are implicit functions of longitude. For every point of a specific height, they must be re-computed. Instead of re-computing them at each new point, we can pre-tabulate them for a number of representative heights, then interpolate their values at the height of individual point using the tabulated values. Simple linear interpolation can then be used to predict C_α and C_β for a non-tabulated height with sufficient accuracy (see Figure 3.10). A numerical test has shown that the maximum difference between the new algorithm and the standard algorithm is smaller than 0.001 mGal in the Rocky Mountains. By using interpolation, the improvement of speed is as good as that of the height-independent problem. The following recursive formula by Rizos (1979) can further speed up the summation.

$$\begin{aligned} a \cos m(j\Delta\lambda) + b \sin m(j\Delta\lambda) &= 2 \cos m\Delta\lambda [a \cos m(j-1)\Delta\lambda \\ &+ b \sin m(j-1)\Delta\lambda] - [a \cos m(j-2)\Delta\lambda + b \sin m(j-2)\Delta\lambda]. \end{aligned} \quad (3.29)$$

Figure 3.11 shows that the series $C_\alpha(m, H, \theta)$ attenuates rapidly with respect to

the order m revealing rapid convergence of the series (3.26) at the lower orders as well.

3.2 The Discrete Poisson Integral Equations

The Poisson downward continuation can be considered as a ‘projection’ in which the gravity anomalies observed on the Earth surface are ‘mapped’ to the geoid by satisfying the Poisson integral equation. The Poisson integral equation has no analytical solution, therefore, the ‘projection’ can be performed only by numerical methods that require discretization of it. On the other hand, the gravity data are usually observed at unevenly distributed discrete points. In the determination of the geoid, these data are routinely interpolated on an evenly spaced grid for convenience in the numerical computation. A variety of methods have been developed for the interpolation of gravity data (Heiskanen and Moritz, 1967; Moritz, 1980; Vaníček and Krakiwsky, 1986). The discussions of these interpolation methods are beyond the scope of this research. Here, it is assumed that gravity anomalies are already available at the evenly spaced node points representing either point values or mean values of their corresponding cells on the Earth surface, while the gravity anomalies at the corresponding cells on the geoid are sought. Consequently, the Poisson integral equation must be discretized in consistency with the grid data.

For the determination of the geoid, the mean gravity anomaly values are routinely evaluated at the Earth’s surface to smooth the gravity field and reduce the aliasing error (Vaníček et al., 1996; Featherstone, 2000). Therefore, the Poisson integral equation should be discretized based on the mean values. However, discussions of models based on the point values may give us a comprehensive insight on the downward continuation problem. Further, the point models are more suitable for the downward continuation of airborne gravity since these data are collected at regular spacing, i.e. as point values. With the increasing use of airborne gravimetry, point models

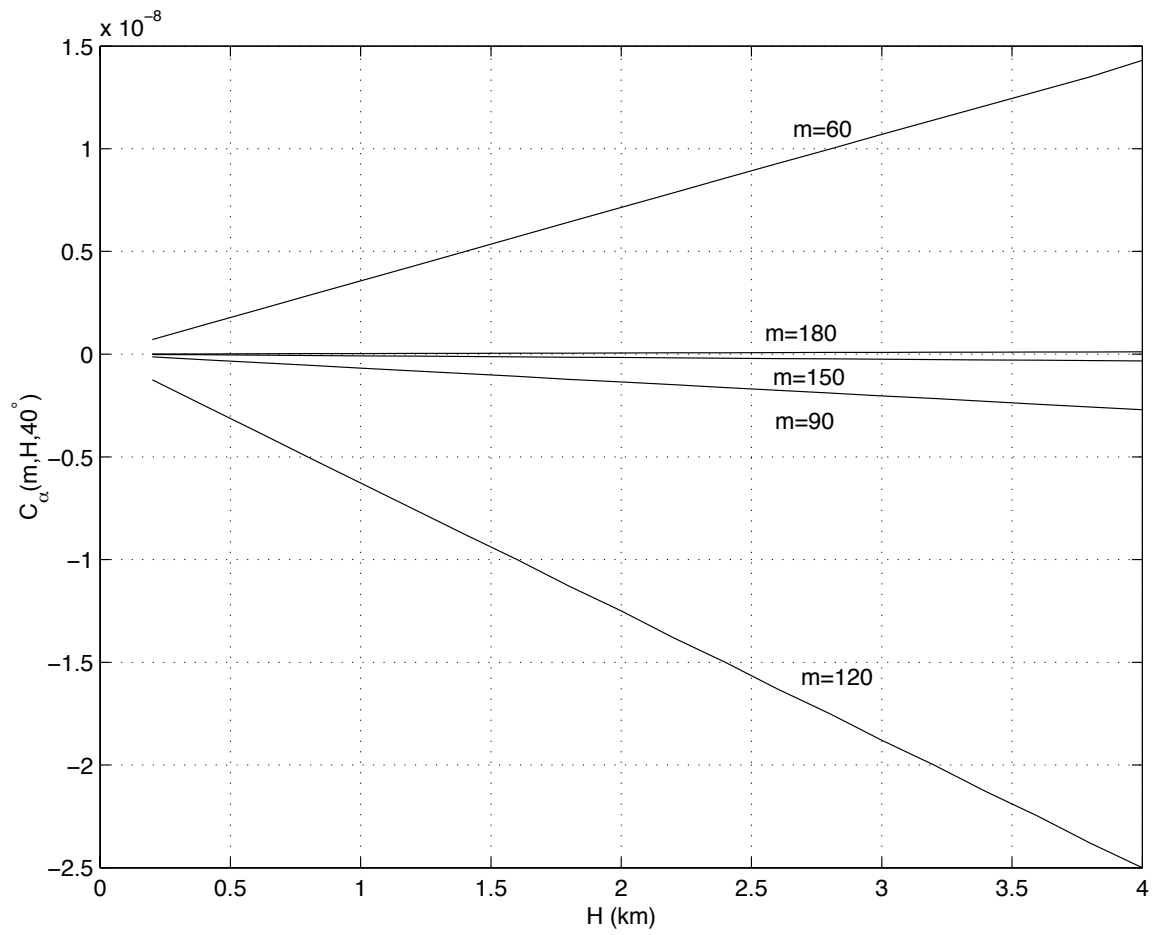


Figure 3.10: $C_\alpha(m, H, \theta)$ vs. H .

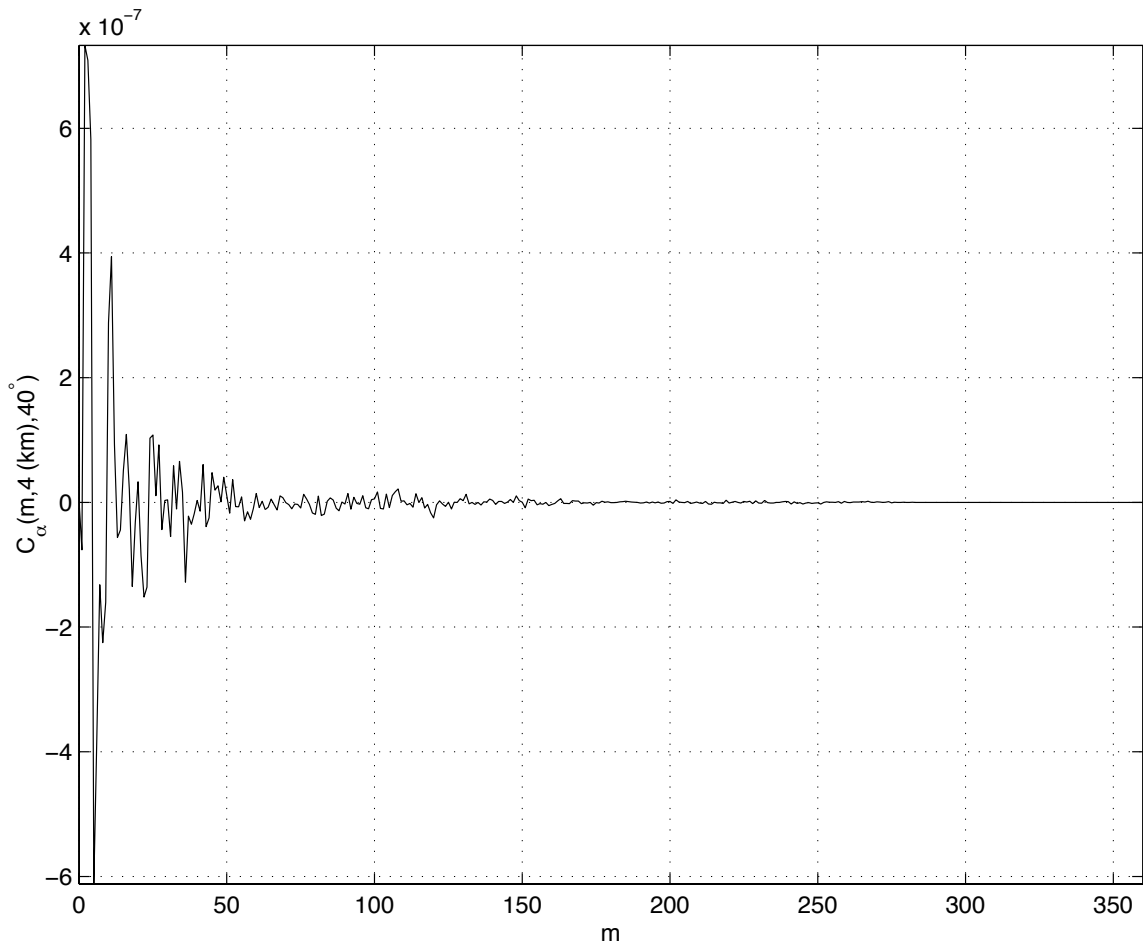


Figure 3.11: $C_\alpha(m, H, \theta)$ vs. m .

will be applied more frequently. Therefore, both the point and the mean models are discussed in this research.

3.2.1 The Point-Point Model

The point-point model assumes that the gravity anomalies on both the Earth's surface and the geoid are taken as point values at central points of appropriate cells. Based on this model, eqn. (3.5) is approximated by (Martinec, 1996)

$$\Delta g^l(r_i, \Omega_i) = \sum_{j=1}^M B_{ij} \Delta g^l(R, \Omega'_j) + F_{\Delta g}^l(r_i, \Omega_i) + d\epsilon_{pp} \quad (i = 1, 2, \dots, N), \quad (3.30)$$

where

$$\forall i \neq j \quad B_{ij} = \begin{cases} \frac{R}{4\pi r} w_j K(r_i, \psi_{ij}, R) & \text{if } \psi_{ij} \leq \psi_0 \\ 0 & \text{other,} \end{cases} \quad (3.31)$$

$$B_{ii} = \frac{R}{r} d^l(r_i, \psi_0, R) - \sum_{j=1, j \neq i}^M B_{ij}, \quad (3.32)$$

$$d^l(r, \psi_0, R) = \frac{1}{4\pi} \int_{\Omega'_0} K(r, \psi, R) d\Omega'. \quad (3.33)$$

The upper limit M represents the total number of cells within the near-zone cap. The upper limit N stands for the total number of the unknowns on the geoid. The weights w_j are taken as areas of integration cells for simplicity. Martinec (1996) gives d^l for the standard and spheroidal Poisson kernels K and $K^{l, S}$ as

$$d^l(r, \psi_0, R) = \frac{1}{2} \left[\frac{r+R}{r} \left(1 - \frac{r-R}{L(r, \psi_0, R)} \right) \right], \quad (3.34)$$

$$\begin{aligned} d^{l, S}(r, \psi_0, R) = & \frac{1}{2} \left[\frac{r+R}{r} \left(1 - \frac{r-R}{L(r, \psi_0, R)} \right) - \frac{R}{r} (1 - \cos \psi_0) \right. \\ & \left. + \sum_{n=1}^l (2n+1) \left(\frac{R}{r} \right)^{n+1} R_n(\cos \psi_0) \right]. \end{aligned} \quad (3.35)$$

For the modified spheroidal Poisson kernel $K^{l, MS}$, $d^{l, MS}$ can be easily derived

$$d^{l, MS}(r, \psi_0, R) = \frac{1}{2} \left[\frac{r+R}{r} \left(1 - \frac{r-R}{L(r, \psi_0, R)} \right) - \frac{t_0(H, \psi_0)}{2} (1 - \cos \psi_0) + \sum_{n=1}^l \frac{2n+1}{2} t_n(H, \psi_0) R_n(\cos \psi_0) \right], \quad (3.36)$$

where

$$R_n(x) = \frac{1}{2n+1} [P_{n+1}(x) - P_{n-1}(x)]. \quad (3.37)$$

The last term on the right side of eqn. (3.30) represents the discretization error. It can be expressed as

$$d\epsilon_{pp} = \sum_{j=1, j \neq i}^M \frac{R}{4\pi r_i} \int_{\Delta\Omega'_j} [K(r_i, \psi, R) \Delta g^l(R, \Omega') - K(r_i, \psi_{ij}, R) \Delta g^l(R, \Omega'_j)] d\Omega' + \frac{R}{4\pi r_i} \int_{\Delta\Omega'_i} K(r_i, \psi, R) [\Delta g^l(R, \Omega') - \Delta g^l(R, \Omega'_i)] d\Omega'. \quad (3.38)$$

The point-point model has an obvious advantage for the evaluation of the coefficients B_{ij} because the appropriate kernel needs to be evaluated only once for each coefficient. However, it is subject to an aliasing error due to a finite sampling step of data. For a strongly variable gravity field, the presence of the aliasing error may impose a serious difficulty in obtaining a reliable solution. Thus, it is necessary to adopt the foregoing procedure to smooth the gravity field. For example, using a filter or a proper condensation model reduces or eliminates the components beyond the highest distinguishable frequency of data π/Δ , where Δ is the data sampling step.

3.2.2 The Point-Mean Model

Eqn. (3.5) can discretely be expressed as

$$\Delta g^l(r_i, \Omega_i) = \sum_{j=1}^M \overline{B_{ij}} \overline{\Delta g^l}(R, \Omega'_j) + F_{\Delta g}^l(r_i, \Omega_i) + d\epsilon_{pm} \quad (i = 1, 2, \dots, N), \quad (3.39)$$

where

$$\overline{B_{ij}} = \begin{cases} \frac{R}{4\pi r} \int_{\Delta\Omega'_j} K(r_i, \psi_{ij}, R) d\Omega' & \text{if } \psi_{ij} \leq \psi_0, \\ 0 & \text{other.} \end{cases} \quad (3.40)$$

The $\overline{\Delta g^l}$ represent the ‘mean’ values for the corresponding cells on the geoid. The discretization error in eqn. (3.39) can be written as

$$d\epsilon_{pm} = \sum_{j=1}^M \frac{R}{4\pi r_i} \int_{\Delta\Omega'_j} K(r_i, \psi, R) [\Delta g^l(R, \Omega') - \overline{\Delta g^l}(R, \Omega'_j)] d\Omega'. \quad (3.41)$$

This model discretizes the gravity anomalies on the geoid as mean values but takes the point gravity anomalies at the central points of the appropriate cells on the Earth surface. Similar to the point-point model, its solution suffers from the aliasing errors too. Preprocessing of data is required to smooth the gravity field.

The physical interpretation of this model is that it allows an upward continuation of point values if the mean values $\overline{\Delta g^l}$ are known on the geoid. Conversely, the mean values on the geoid can be determined by the downward continuation when the proper preprocessing of the point values is done.

3.2.3 The Mean-Mean Model

By taking the average of both sides of eqn. (3.30) with respect to the cells $\Delta\Omega_i$ on the Earth surface, we get (Vaníček et al., 1996):

$$\overline{\Delta g^l}(r_i, \Omega_i) = \sum_{j=1}^M \overline{B_{ij}} \overline{\Delta g^l}(R, \Omega'_j) + \overline{F_{\Delta g}^l}(r_i, \Omega_i) + d\epsilon_{mm} \quad (i = 1, 2, \dots, N), \quad (3.42)$$

where

$$\overline{\Delta g^l}(r_i, \Omega_i) = \frac{1}{A_i} \int_{\Delta\Omega_i} \Delta g^l(r, \Omega) d\Omega, \quad (3.43)$$

$$\overline{B_{ij}} = \frac{1}{A_i} \int_{\Delta\Omega_i} B_{ij}(r, \Omega) d\Omega, \quad (3.44)$$

$$\overline{F_{\Delta g}^l}(r_i, \Omega_i) = \frac{1}{A_i} \int_{\Delta\Omega_i} F_{\Delta g}^l(r, \Omega) d\Omega. \quad (3.45)$$

A_i are the areas of the cells on the Earth surface. The discretization error, or more precisely the averaging error $d\epsilon_{mm}$, can be written as²

$$d\epsilon_{mm} = \frac{1}{A_i} \int_{\Delta\Omega_i} \sum_{j=1}^M \frac{R}{4\pi r} \int_{\Delta\Omega'_j} K(r, \psi, R) [\Delta g^l(R, \Omega') - \overline{\Delta g^l}(R, \Omega'_j)] d\Omega' d\Omega. \quad (3.46)$$

²Vaníček, 2001, personal communication.

In this model, both the known and unknown gravity anomalies are expressed as the mean values over the cells on both the Earth's surface and on the geoid. If the mean gravity anomalies are used, this model is directly applicable. It is a model for the upward and downward continuations from mean to mean values.

3.2.4 Analysis of the Discrete Models

The matrix coefficients for the three discrete models described above can be expressed in spherical harmonic form. By substituting eqn. (2.10) into eqns. (3.32) and (3.31) the coefficients of the point-point model can be written as

$$\begin{aligned} B_{ii} &= \frac{1}{4\pi} \sum_{n=0}^{\infty} \lambda_n \sum_{m=-n}^n Y_{nm}(\Omega_i) \overline{Y_{nm}}(\Omega_i) A_i, \\ B_{ij} &= \frac{1}{4\pi} \sum_{n=0}^{\infty} \lambda_n \sum_{m=-n}^n Y_{nm}(\Omega_i) Y_{nm}(\Omega_j) w_j \quad \text{if } i \neq j, \end{aligned} \quad (3.47)$$

where

$$\overline{Y_{nm}}(\Omega_k) = \frac{1}{A_k} \int_{\Delta\Omega_k} Y_{nm}(\Omega) d\Omega, \quad (3.48)$$

is called the mean of spherical harmonics in cells $\Delta\Omega_k$. By substituting eqn. (2.10) into eqn. (3.40), the coefficients of the point-mean model can be written as

$$\overline{B_{ij}} = \frac{1}{4\pi} \sum_{n=0}^{\infty} \lambda_n \sum_{m=-n}^n Y_{nm}(\Omega_i) \overline{Y_{nm}}(\Omega_j) A_j. \quad (3.49)$$

By substituting eqn. (2.10) into eqn. (3.44), the coefficients of the mean-mean model can be written as

$$\overline{\overline{B_{ij}}} = \frac{1}{4\pi} \sum_{n=0}^{\infty} \lambda_n \sum_{m=-n}^n \overline{Y_{nm}}(\Omega_i) \overline{Y_{nm}}(\Omega_j) A_j. \quad (3.50)$$

The mean of spherical harmonics $\overline{Y_{nm}}$ are considerably smoother than Y_{nm} due to the averaging which tends to suppress the high-frequency variation of Y_{nm} . Therefore, the matrix coefficients for the mean-mean model are systematically smoother than the matrix coefficients for both the point-point and the point-mean models because of the double uses of the mean of the spherical harmonics. One would expect that

the roughest continuation results be produced from the mean-mean model if the same data are input into the three models. Accordingly, the point-mean model will generate rougher results than the point-point model.

However, the degree of roughness by no means gives any information on the accuracy of a model and its closeness to reality. From the spectral point of view, the mean-mean model is preferable to the other two models since it tends to reduce the high-frequency aliasing error being suffered by the other two models. In practice, gravity anomalies used in the determination of geoid are often in the form of mean values. If they represent true mean values, the mean-mean model will provide the best solution theoretically. The practice of using the true mean values in the point-point model, or the point-mean model brings biases into the solution because of the misuse of the models.

Sun and Vaníček (1998) discuss numerical differences between the mean and the point models. It deserves to be pointed out that their conclusions do not reflect the discussions here since by the point model they use a different definition from either the point-point model and the point-mean model introduced here. In Sun and Vaníček's discussions, the coefficients for the central cells are evaluated from the point kernel values, while here they are evaluated from the mean kernel values in the point-point model.

The above analysis is more or less heuristic, and does not answer the important question: Are the coefficient matrices for the discrete models singular or close to being singular? Alternatively, what is the condition of the coefficient matrices? A powerful technique for dealing with sets of equations or matrices that are either singular or numerically very close to being singular is known as *singular value decomposition*, or SVD. It will not only diagnose the system, but it will also solve it. If the matrix B is square, its inverse can be constructed as (Golub and Van Loan, 1983)

$$B^{-1} = V\Sigma^{-1}U^T. \tag{3.51}$$

The matrices U and V are column-orthonormal. Σ is a diagonal matrix with positive or zero elements σ_i , called *singular values*. If one of σ_i is zero, or small enough to be considered as roundoff error, the system becomes singular or extremely unstable. The condition number of a matrix is defined as the ratio of the largest singular value σ_{max} to the smallest singular value σ_{min} . A matrix is singular if its condition number is infinite, and it is ill-conditioned if its condition number is so large that its reciprocal approaches the floating-point precision of a computer system. The larger the condition number, the less stable the system.

Table 3.2: Statistics of the mean $5' \times 5'$ DEM in the test regions. Unit: m.

Region	Min	Max	Mean	StdDev	RMS
A ($49^\circ N - 52^\circ N$, $114^\circ W - 119^\circ W$)	459	2682	1599	431	1656
B ($46^\circ N - 49^\circ N$, $68^\circ W - 73^\circ W$)	0	942	316	202	376
C ($49^\circ N - 52^\circ N$, $104^\circ W - 109^\circ W$)	488	1122	684	122	694

Table 3.3: Condition numbers in the test regions by using the mean $5' \times 5'$ DEM.

Region	Point-Point	Point-Mean	Mean-Mean
A	2.612	3.146	6.483
B	1.315	1.409	2.219
C	1.396	1.514	2.436

We have selected three regions for analysis using SVD: region A covers the roughest part of the Rocky Mountains, region B covers the southern part of Quebec, and region C covers the southern part of Manitoba. The statistical information of the $5' \times 5'$ DEM is shown in Table 3.2. The SVDCMP routine is used to compute the SVD of the coefficient matrices (Press, et al., 1992).

Figure 3.12 shows the singular values spectrum of the three discrete models in the test regions in ascending order. A common feature among these regions is that the mean-mean model possesses the biggest condition number tending to produce the

roughest solution for each region, while the point-point model displays the smallest condition number tending to produce the smoothest solution for each region (see Table 3.3). Region A has the largest condition number for each discrete model, implicating that the elevation is the dominant factor in determining the condition of the coefficient matrix. Region B with more rugged relief but smaller mean elevation than region C has a smaller condition number for each discrete model than Region C. It implies that the mean elevation of the region rather than the relative relief determines the condition of the coefficient matrix. These results also show that the $5' \times 5'$ downward continuation appears to be a stable problem in Canada regardless of the discrete model being applied

3.3 Summary

Discretization of Poisson's integral is a process of approximating the continuous Poisson integral in a discrete form that is expected to best use the available data and to efficiently eliminate errors and biases in the evaluation of continuation. The discretization comprises the following issues: **a)** evaluation of the far-zone contribution, **b)** modification of the Poisson kernel, **c)** combination of terrestrial data with a satellite geopotential model, **d)** truncation of the Poisson integral, and **e)** discretization of the Poisson integral in the near-zone.

The far-zone contribution was formulated by using the Molodenskii-type harmonic expansion technique based on the standard, spheroidal and modified spheroidal Poisson kernels.

The efficiency of reducing the real far-zone contribution for the spheroidal Poisson kernel was studied when the modified spheroidal Poisson kernel was adopted. The numerical results showed that the modified spheroidal Poisson kernel significantly reduces the real far-zone contribution. In the meantime, the standard Poisson kernel performs as efficiently as the modified spheroidal Poisson kernel in reducing the real

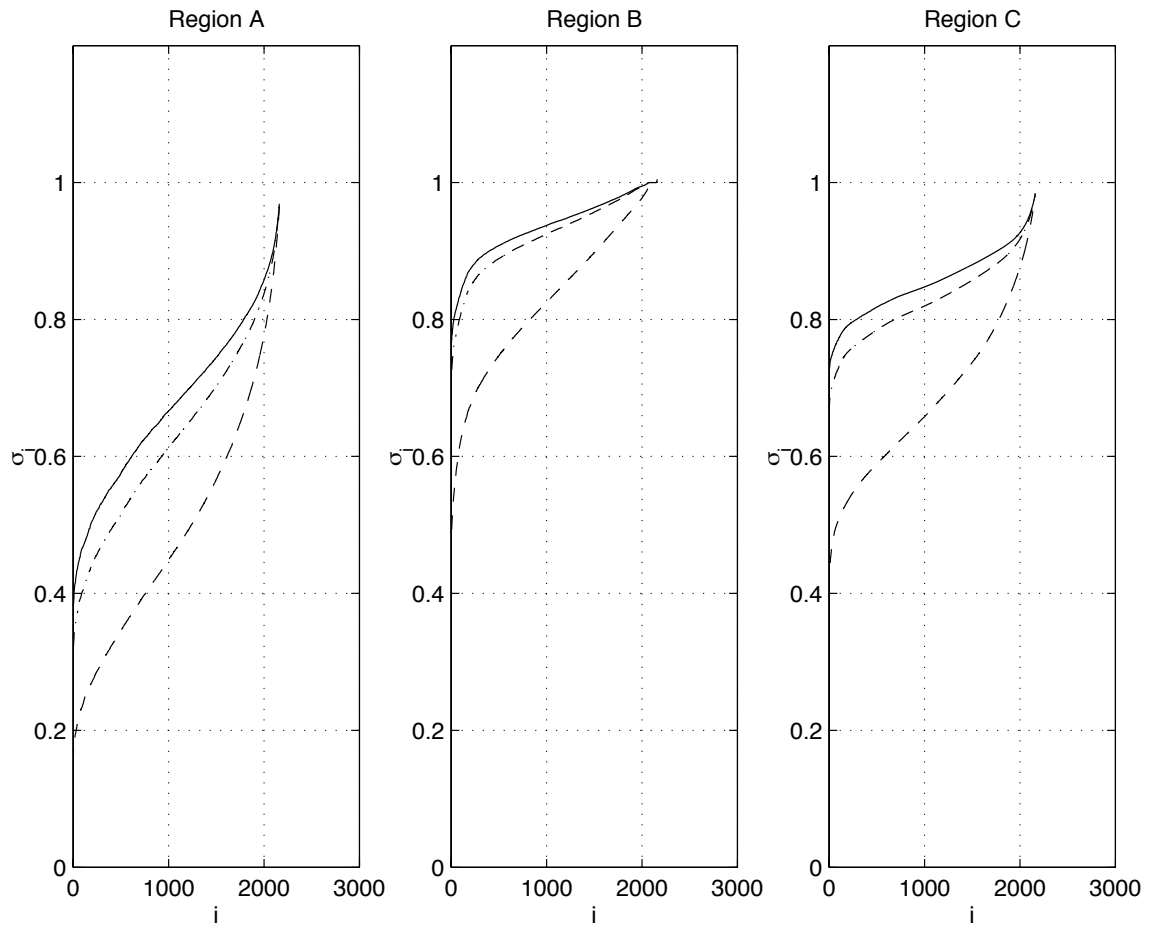


Figure 3.12: The singular value spectrum of the coefficient matrices for the point-point model (solid lines), the point-mean model (dotdashed lines), and the mean-mean model (dashed lines) of $5' \times 5'$.

far-zone contribution.

The determination of the critical radius for the near-zone cap was discussed. The results suggested that Heiskanen and Moritz's condition gives a radius that is too small for the determination of the 1-cm geoid while Martinec's condition gives a radius that is unnecessarily large.

An efficient algorithm for evaluation of the far-zone contribution was developed. The new algorithm is one order of magnitude faster than the standard algorithm while providing sufficient accuracy.

The three discrete models for Poisson's integral were formulated. The analysis for these models indicated that the mean-mean model tends to produce the roughest solution, while the point-point model tends to give the smoothest solution among the three models. Furthermore, the topographical elevation rather than the relative relief determines the condition of the coefficient matrix for a discrete model. The numerical tests in different regions within Canada showed that the $5' \times 5'$ downward continuation is a very stable problem regardless of the discrete model used.

Chapter 4

Solution of the Discrete Poisson Integral Equations

There is a variety of methods for solving a linear system of equations. The most straightforward method is by computing the inverse of a matrix, followed by multiplication by the data vector. Because of its inefficiency, this method appears more frequently in theoretical formulation as a concise operator rather than in practical computation. The most common method for numerical computation is known as Gaussian elimination. It is the standard method for the geodetic least-squares adjustment calculation. If the coefficient matrix has the properties of symmetry and regularity, Gaussian elimination can efficiently solve the system of equations. Another class of methods are the iterative ones. These methods are preferred to Gaussian elimination for a sparse and ill-conditioned coefficient matrix. When the coefficient matrix is sparse, computer memory requirements are more economical. Furthermore, they may reduce the round-off error introduced by the elimination method. Because of the sparseness and ill-conditioning of the coefficient matrix of the inverse Poisson problem, the iterative approach is most suitable. It usually takes less time than Gaussian elimination to lead to a solution. However, if the problem of interest is extremely ill-conditioned, the iterative approach will fail to give a meaningful solution. In this case,

the regularization technique is usually used to produce a reasonable approximation to the true solution. Among various regularization techniques, the truncated singular value decomposition is superior to others for the Poisson downward continuation, while mathematical similarity holds among them (Hansen, 1987, 1990, 1992).

In Chapter 3, the three discrete models were formulated and discussed. Each of them introduces the discretization error (in the case of the mean-mean model, it is specifically referred as the averaging error) into the appropriate model. It is necessary to assess the numerical accuracy of these models. In other words, we expect to know the accuracy of these models. A synthetic approach has been used to simulate and assess the accuracy of the Stokes integration, and to simulate satellite gravity missions (Novák et. al., 2000; Jekeli et. al., 2000). In this research, we will use synthetic data to study the accuracy of the three discrete models.

The coefficient matrix of the discrete Poisson equation is large and sparse. With increasing resolution, difficulty of solving it becomes even more evident. An efficient algorithm is needed to optimize the computational procedure.

In this chapter, the Combined Iterative method is suggested to deal with the inverse Poisson problem. The synthetic approach is used to assess the accuracy of Poisson's integral equation solution for each discrete model, and to determine the critical truncation radius of the Poisson integral. An efficient algorithm is developed to perform the downward continuation computation. The truncated singular value decomposition is introduced to solve the ill-conditioned system.

4.1 The Combined Iterative Method

The two most frequently used iteration methods are the Jacobi and Gauss-Seidel methods. The Gauss-Seidel method converges more rapidly than the Jacobi method (Faddeev and Faddeev, 1963; Gerald and Wheatley, 1994). In order to perform the downward continuation computation more efficiently, a combined iterative method

is suggested by associating the Jacobi iterative form with the Gauss-Seidel iterative procedure.

Let B represent the coefficient matrix, \mathbf{g} the gravity anomaly vector corrected by the far-zone contribution on the Earth surface, and \mathbf{f} the gravity anomaly vector on the geoid. The discrete models can then be expressed as a linear system of equations.

$$B\mathbf{f} = \mathbf{g}. \quad (4.1)$$

By substituting $B = I - A$ into eqn.(4.1), it is transformed into the Jacobi iterative form.

$$\mathbf{f} = A\mathbf{f} + \mathbf{g}. \quad (4.2)$$

This equation means that the downward continuation solution \mathbf{f} is equal to the corresponding known \mathbf{g} plus a correction accounting for the change of \mathbf{g} from the Earth surface to the geoid. By following the Gauss-Seidel iterative procedure, the first iteration is expressed as

$$\begin{aligned} f_1^1 &= a_{11}f_1^0 + a_{12}f_2^0 + a_{13}f_3^0 + \dots + a_{1n}f_n^0 + g_1 \\ f_2^1 &= a_{21}f_1^1 + a_{22}f_2^0 + a_{23}f_3^0 + \dots + a_{2n}f_n^0 + g_2 \\ f_3^1 &= a_{31}f_1^1 + a_{32}f_2^1 + a_{33}f_3^0 + \dots + a_{3n}f_n^0 + g_3 \\ &\dots \\ f_n^1 &= a_{n1}f_1^1 + a_{n2}f_2^1 + a_{n3}f_3^1 + \dots + a_{nn}f_n^0 + g_n, \end{aligned} \quad (4.3)$$

where $\mathbf{f}^0 = \mathbf{g}$. In the process of iteration, the most recent f -values are always used in improving the subsequent f -values. The second and subsequent iterations follow the same approach until the Tchebyshev norm of the difference between two consecutive f -values $f^{(i)}$, $f^{(i+1)}$ is smaller than a specified threshold value. Advantages of the combined iterative procedure include a) no memory is needed to store the f -values from the previous iteration, b) the data vector \mathbf{g} remains unchanged through the entire process, and c) a faster rate of convergence.

4.2 Synthetic Geopotential Models

In Chapter 3, three distinct discretization models for the evaluation of the Poisson integral were presented. Each of them can generate an approximation to the true solution. However, we are not able to evaluate their accuracy because there is usually no true solution available to compare it against. An experimental approach with regard to the evaluation of their accuracy is the synthetic test for which a synthetic gravity model is required. As a synthetic model, it must meet two essential experimental requirements:

1. be a physically realistic representation of the real field;
2. provide means to evaluate all parameters mathematically.

For testing of the downward continuation methods, a spherical harmonic geopotential model with sufficiently high frequency components fulfills the requirements. By ‘sufficient’ we mean that the degree and order of the spherical harmonics must be compatible with the sampling interval of data. According to the sampling theorem, the spherical harmonic model of degree and order 360 matches the $30' \times 30'$ data spacing, and the spherical harmonic model of degree and order 2160 matches the $5' \times 5'$ data spacing.

The latest NASA global geopotential model - Earth Gravitational Model 1996 (EGM96) is complete up to degree and order 360 (Lemoine et al., 1997). It may be used to test the $30' \times 30'$ downward continuation. But it is too smooth to test the $5' \times 5'$ downward continuation because of the absence of the high-degree components. Wenzel (1998) developed two ultra-high degree geopotential models GPM98a and GPM98b complete to degree and order 1800. Both models use EGM96 to degree and order 20, whereas the rest comes from the mean $5' \times 5'$ gravity anomalies. The difference between GPM98a and GPM98b is that different $5' \times 5'$ data sets and different computational procedures were adopted in developing them. The research group at

the Curtin University of Technology, Australia, developed an approach to generate a synthetic Earth gravity model complete up to degree and order 5400 (Holmes and Featherstone, 1999). In this approach, all synthetic geoid heights and gravity anomalies were referenced to the Geodetic Reference System 1980 (GRS80). Geopotential coefficients for degrees $n = 2$ to 360 were taken from EGM96, while coefficients of degrees $n = 361$ to 1800 were adopted from GPM98. For degrees $n = 1801$ to 5400, the coefficients of EGM96 were repeatedly re-scaled and recycled to generate values for all the high degree synthetic coefficients. Synthetic gravity anomalies of realistic magnitude and variability were obtained by scaling the synthetic coefficients conforming to Tscherning-Rapp model (1974) at the mean radius of the Earth. This model has been used to test the performance of different modification methods to the Stokes kernel (Holmes and Featherstone, 1999; Novák et al., 2001).

The anomaly degree variances of EGM96 and GPM98a are plotted in Figure 4.1 against Tscherning-Rapp's anomaly degree variances. One would expect that synthetic coefficients beyond degree 1800 conforming to Tscherning-Rapp's degree variance model would add no significant contribution to the gravity field and the geoid since the anomaly degree variances above degree 1000 would have been attenuated to smaller than 1 mGal^2 . Therefore, GPM98a is an acceptable choice for the experimental test of the downward continuation as it is a realistic geopotential model. In this research, GPM98a was used to assess the discrete models of Poisson's integral, and to determine the critical truncation radius of the integral. It is acknowledged that other synthetic models (eg. Haagmans, 2000) may better serve our purposes, but they were not available when this research was done.

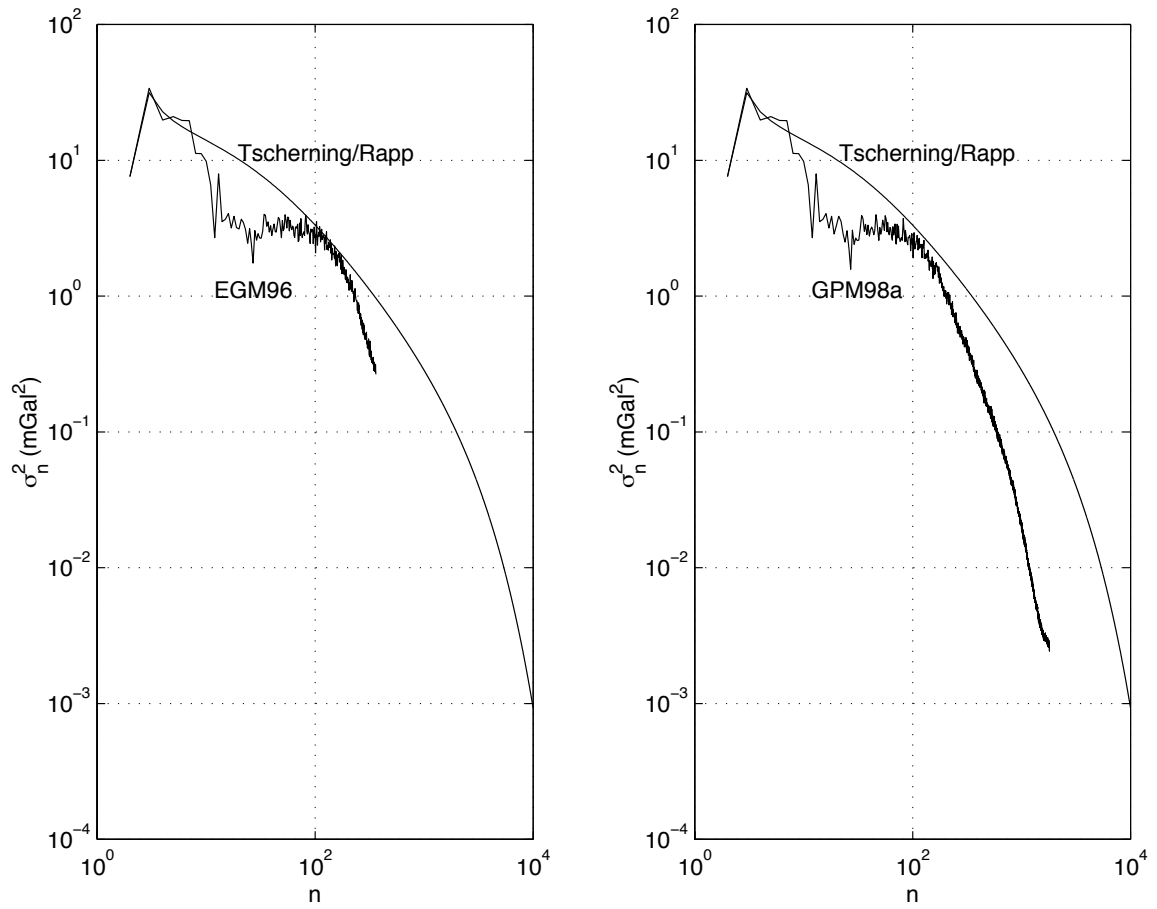


Figure 4.1: Anomaly degree variances σ_n^2 of the Tscherning/Rapp degree variance model, EGM96 and GPM98a.

4.3 Synthetic Tests of Discrete Models for Poisson's Integral Equation

In Chapter 3, the three discrete models for Poisson's integral equation were formulated: the mean-mean model, the point-mean model and the point-point model. This section focuses on testing the three models against synthetic data generated from GPM98a to learn how the discretization error affects accuracy of the downward continuation for each model, and to find the proper method to deal with it if necessary.

The test region is located in the Rocky Mountains, delimited by latitudes of 49°N-52°N and longitudes of 114°W-119°W, where the mean 5' × 5' heights range from 459 m to 2684 m with a mean of 1599 m and a standard deviation of 431 m. Two data sets were generated from GPM98a: **a)** The mean 5' × 5' gravity anomalies on the Earth's surface and on the geoid were computed from point values evaluated on a grid of 30'' × 60''. The mean 30'' × 60'' DEM was used to represent the 'true' Earth's surface on which the 30'' × 60'' point gravity anomalies were evaluated; **b)** The point 5' × 5' gravity anomalies were computed on the geoid and on the Earth's surface where the mean 5' × 5' DEM was used. The statistical information of these synthetic data is shown in the first rows of Tables 4.1-4.3.

Tables 4.1-4.3 show the test results for the GPM98a synthetic data. The over-bar indicates mean value. Superscript 'syn' indicates synthetic data, 'ddc' shows the discrete Poisson downward continuation, $D\Delta g$ is the downward continuation correction, and δ indicates the error of the Poisson downward continuation. The mean 5' × 5' DEM was used for evaluating coefficients B_{ij} and $\overline{B_{ij}}$ of the point-point and point-mean models, while the mean 30'' × 60'' DEM was used for evaluating coefficients $\overline{\overline{B_{ij}}}$ of the mean-mean model. In other words, the same DEMs were consistently used for both the synthetic data and the downward continuations to eliminate approximation errors originated from the use of the DEMs.

Table 4.1: The $5' \times 5'$ point-point downward continuation of the synthetic field of degree 21 to degree 1800 derived from GPM98a. $\psi_0 = 1^\circ$. Unit: mGal.

Parameter	Min.	Max.	Mean	StdDev	RMS.
Δg_q^{syn}	-12.109	-0.901	-7.624	2.244	7.947
Δg_q^{ddc}	-12.108	-0.887	-7.622	2.242	7.945
$D\Delta g^{syn}$	-1.260	0.135	-0.233	0.242	0.335
$D\Delta g^{ddc}$	-1.218	0.113	-0.231	0.234	0.328
$F_{\Delta g}^{20}$	-0.103	0.052	-0.021	0.034	0.041
δ	-0.042	0.022	-0.002	0.010	0.010

Table 4.2: The $5' \times 5'$ point-mean downward continuation of the synthetic field of degree 21 to degree 1800 derived from GPM98a. $\psi_0 = 1^\circ$. Unit: mGal.

Parameter	Min.	Max.	Mean	StdDev	RMS.
$\overline{\Delta g}_q^{syn}$	-12.107	-0.833	-7.621	2.243	7.944
$\overline{\Delta g}_q^{ddc}$	-12.109	-0.929	-7.622	2.244	7.946
$D\overline{\Delta g}^{syn}$	-1.143	0.090	-0.230	0.216	0.316
$D\overline{\Delta g}^{ddc}$	-1.295	0.141	-0.231	0.248	0.339
$F_{\Delta g}^{20}$	-0.103	0.052	0.021	0.034	0.041
δ	-0.054	0.152	0.001	0.036	0.036

Table 4.3: The $5' \times 5'$ mean-mean downward continuation of the synthetic field of degree 21 to degree 1800 derived from GPM98a. $\psi_0 = 1^\circ$. Unit: mGal.

Parameter	Min.	Max.	Mean	StdDev	RMS.
$\overline{\Delta g}_q^{syn}$	-12.107	-0.833	-7.621	2.243	7.944
$\overline{\Delta g}_q^{ddc}$	-12.172	-1.109	-7.623	2.241	7.946
$\overline{D\Delta g}^{syn}$	-1.240	0.120	-0.233	0.230	0.333
$\overline{D\Delta g}^{ddc}$	-1.375	0.187	-0.235	0.283	0.368
$F_{\Delta g}^{20}$	-0.103	0.052	-0.021	0.034	0.041
δ	-0.083	0.276	0.002	0.055	0.055

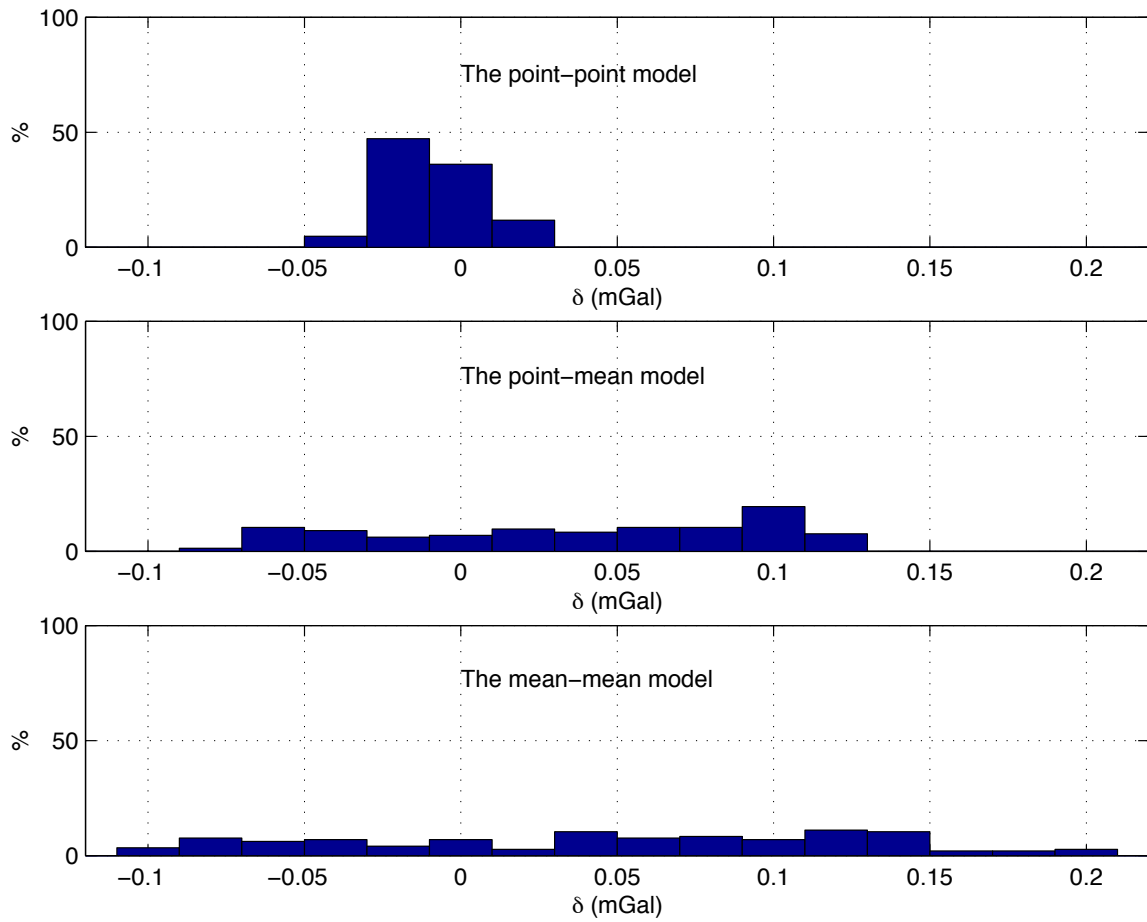


Figure 4.2: Error distribution of the downward continuation using the GPM98a synthetic data.

Observing the results from these three discrete models, we can see that the point-point model gives a result very close to the point-point synthetic solution, while the mean-mean downward continuation result shows significantly worse conformity to the mean-mean synthetic solution (see Figure 4.2).

There are four different sources that may have caused the downward continuation errors shown in Tables 4.1-4.3: numerical errors related to the conditions of the coefficient matrices, iterative errors, data errors and the discretization errors. The downward continuation error for each model is independent from the condition of the appropriate matrix because the $5' \times 5'$ downward continuation is a well-conditioned problem regardless of the model used. It is also independent from the iterative errors because the Tchebyshev norm of the solution differences between two consecutive iterations was chosen as 0.001 mGal. As for the data errors, the DEMs were consistently used for evaluating both the synthetic data and the downward continuation to avoid the approximation errors from the uses of the DEMs, and the synthetic gravity data were evaluated at an accuracy of 0.001 mGal. Therefore, the discretization errors are the sources that render the downward continuation errors shown in Tables 4.1-4.3. This conclusion implies that the averaging error for the mean-mean model affects the downward continuation more significantly than the discretization error for the point-point model does. In order to verify this conclusion, the averaging error for the mean-mean model (3.42) has been evaluated by using eqn. (3.46) from the $30'' \times 60''$ point synthetic data on the geoid, and shown in Table 4.4. After correcting for this error, the mean-mean downward continuation error reduces to a level that represents the numerical noise of the $30'' \times 60''$ point-point upward continuation. This result confirms the implication above.

To further learn the characteristics of the averaging error and its effect on the mean-mean downward continuation, synthetic tests with respect to different grid steps have been conducted. In the tests, the mean $2' \times 5'$ and $2' \times 2'$ synthetic data were formed from the $30'' \times 60''$ point synthetic data on both the geoid and the

Earth's surface, respectively. Table 4.5 shows the averaging errors and their downward continuations with respect to different grid steps. It is evident that the averaging error decreases with the decreasing grid step. Table 4.6 shows the mean-mean downward continuation errors with and without the corrections of the averaging errors with respect to different grid steps. After correcting for the averaging errors, the downward continuation errors for all grid steps reduce to the noise level of the $30'' \times 60''$ point-point upward continuation.

Table 4.4: The $5' \times 5'$ mean-mean downward continuation of the synthetic field of degree 21 to degree 1800 derived from GPM98a *with the correction of the averaging error*. $\psi_0 = 1^\circ$. Unit: mGal.

Parameter	Min.	Max.	Mean	StdDev	RMS.
$\overline{\Delta g}_q^{syn}$	-12.107	-0.833	-7.621	2.243	7.944
$\overline{\Delta g}_q^{ddc}$	-12.101	-0.839	-7.618	2.241	7.941
$\overline{D\Delta g}^{syn}$	-1.240	0.120	-0.233	0.230	0.333
$\overline{D\Delta g}^{ddc}$	-1.242	0.124	-0.230	0.239	0.332
$F_{\Delta g}^{20}$	-0.103	0.052	-0.021	0.034	0.041
$d\epsilon_{mm}$	-0.152	0.055	-0.006	0.039	0.040
δ	-0.012	0.006	-0.003	0.004	0.005

Table 4.5: The averaging errors and their downward continuation of the mean-mean model for different grid steps. $\psi_0 = 1^\circ$. Unit: mGal.

Grid	Min.	Max.	Mean	StdDev	RMS.	Comment
$5' \times 5'$	-0.152	0.055	-0.006	0.039	0.040	on the Earth's surface
$2' \times 5'$	-0.085	0.053	0.002	0.022	0.022	
$2' \times 2'$	-0.033	0.011	0.001	0.009	0.009	
$5' \times 5'$	-0.270	0.082	-0.005	0.053	0.054	continued on the geoid
$2' \times 5'$	-0.140	0.115	0.003	0.032	0.032	
$2' \times 2'$	-0.062	0.039	0.001	0.014	0.014	

Even though the point-point model appears to be more accurate than the mean-mean model, it is arguable that the point-point model leads to a better solution.

Table 4.6: The mean-mean downward continuation errors for different grid steps with and without the correction of the averaging errors. $\psi_0 = 1^\circ$. Unit: mGal.

Grid	Min.	Max.	Mean	StdDev	RMS.	Comment
$5' \times 5'$	-0.083	0.276	0.002	0.055	0.055	without the correction of $d\epsilon_{mm}$
$2' \times 5'$	-0.115	0.139	-0.003	0.032	0.032	
$2' \times 2'$	-0.038	0.060	-0.001	0.013	0.013	
$5' \times 5'$	-0.012	0.006	-0.003	0.004	0.005	with the correction of $d\epsilon_{mm}$
$2' \times 5'$	-0.004	0.004	-0.000	0.001	0.001	
$2' \times 2'$	-0.013	0.014	0.000	0.004	0.004	

When the point-point model is applied to the downward continuation of actual terrestrial gravity data, it will be seriously affected by the aliasing error in mountainous areas (Featherstone and Kirby, 2000). For example, a point value at the central point of a $5' \times 5'$ cell often contains very strong high-frequency local signals produced by the terrain near the point in mountainous area. When this point value is used as a representative value of the cell, it introduces a quite large aliasing error into the solution. In practice, we use only the grid mean gravity anomalies for the determination of the geoid, the mean-mean model should be used for the downward continuation of the mean gravity anomalies from the Earth's surface to the geoid. However, the averaging error should be minimized and (or) accounted for to improve the accuracy of the mean-mean model. From eqn. (3.46), we can observe that a smoother gravity field tends to reduce this error and its effect on the mean-mean downward continuation. On the other hand, when the point gravity anomalies from which the mean anomalies are formed are available, they can be used to approximately estimate and correct for the averaging error.

4.4 Some Numerical Characteristics of the Mean-Mean Model

There are four different grids involved in the solution of the mean-mean downward continuation problem:

- Grid 1 is the grid on which mean anomalies on the Earth's surface are given (eg. $5' \times 5'$ in the section 4.3).
- Grid 2 is the grid on which topographical heights are given (eg. $30'' \times 60''$ in the section 4.3).
- Grid 3 is the grid on which one generates the downward continued point anomalies on the geoid (eg. $30'' \times 60''$ in the section 4.3).
- Grid 4 is the grid on which one computes the mean anomalies ready for the Stokes integration on the geoid (eg. $5' \times 5'$ in the section 4.3).

This section focuses on studying the effects of changing the steps of Grid 2, 3 and 4 on the downward continuation. Both the far-zone contribution and the averaging error are taken into account in the computation to isolate the effect of interest.

Table 4.7 shows the mean-mean downward continuation errors caused by using different DTMs for evaluating the coefficients $\overline{\overline{B_{ij}}}$, i.e. the effect of changing the step of Grid 2. These results indicate that the mean-mean downward continuation is sensitive to the DTM, and that the DTM corresponding to Grid 3 must be used to give an accurate result.

Table 4.8 shows that the mean-mean downward continuation errors caused by using different number of point values within each $5' \times 5'$ cell to evaluate the mean anomaly of the cell on the Earth's surface, i.e. the effect of changing the step of Grid 3. The same $30'' \times 60''$ DTM was used in the computations. The results suggest

Table 4.7: The $5' \times 5'$ mean-mean downward continuation errors of the synthetic field of degree 21 to degree 1800 derived from GPM98a due to using different DTMs for evaluating the coefficients $\overline{\overline{B_{ij}}}$. $\psi_0 = 1^\circ$. Unit: mGal.

DTM	Min.	Max.	Mean	StdDev	RMS.
$30'' \times 60''$	-0.012	0.006	-0.003	0.004	0.005
$1' \times 1'$	-0.012	0.007	-0.003	0.004	0.005
$2' \times 2'$	-0.056	0.051	-0.003	0.014	0.014
$5' \times 5'$	-0.099	0.124	-0.004	0.027	0.027

that the mean anomaly of each cell be computed by as many point values as possible within the cell to derive the accurate mean anomalies on the geoid.

Table 4.8: The $5' \times 5'$ mean-mean downward continuation errors of the synthetic field of degree 21 to degree 1800 derived from GPM98a due to using different grids of point values for evaluating the mean anomalies on the Earth's surface. Unit: mGal.

No. of Point Values	Min.	Max.	Mean	StdDev	RMS.
50 ($30'' \times 60''$)	-0.012	0.006	0.003	0.004	0.005
25 ($1' \times 1'$)	-0.286	0.093	-0.013	0.047	0.049
15 ($1' \times 1'40''$)	-0.261	0.098	-0.012	0.049	0.050
9 ($1'40'' \times 1'40''$)	-0.274	0.111	-0.013	0.054	0.055
4 ($2.5' \times 2.5'$)	-0.378	0.221	-0.004	0.078	0.078

Table 4.9 shows the errors of the downward continued mean gravity anomalies between using two different continuation steps, i.e. the effect of changing the step of Grid 4. The mean $2.5' \times 5'$ and $2.5' \times 2.5'$ mean gravity anomalies were derived from the mean $5' \times 5'$ one by simple spatial reference, i.e. simply meshing the mean $5' \times 5'$ data into the $2.5' \times 5'$ and the $2.5' \times 2.5'$. The purpose of this test is to find the best step of the mean-mean downward continuation if only the mean $5' \times 5'$ anomalies are available. Distinction must be made between the cases shown in Table 4.6 and the cases here. The former uses the different means for the appropriate grid steps, while the latter uses the same mean but meshes them into different grids introducing

the aliasing error into the input data. The same $30'' \times 60''$ DTM was used in all computations. The results show that a finer step significantly worsens the accuracy of the $5' \times 5'$ mean-mean downward continuation results. It means that the step of the mean-mean downward continuation must be identical to that of the mean gravity data (Grid 1) to avoid the aliasing error from misusing the ‘rougner’ mean as the ‘finer’ mean. In other words, when the mean $5' \times 5'$ anomalies are used to represent the mean $2.5' \times 2.5'$ on the Earth’s surface, the resulted downward continued mean $2.5' \times 2.5'$ anomalies on the geoid are significantly aliased.

Table 4.9: The mean-mean downward continuation errors of the synthetic field of degree 21 to degree 1800 derived from GPM98a due to using different grids for evaluating the downward continuation. Unit: mGal.

Step	Min.	Max.	Mean	StdDev	RMS.
(1) $5' \times 5'$	-0.012	0.006	0.003	0.004	0.005
(2) $2.5' \times 5'$	-0.105	0.633	0.013	0.089	0.090
(3) $2.5' \times 2.5'$	-0.406	0.878	0.015	0.213	0.213

4.5 Synthetic Test for The Critical Radius of the Near-Zone Cap

The same GPM98a synthetic data set as the one generated in Section 4.3 is used to verify whether the 0.5° can be taken as the radius of the near-zone cap (when the maximum mean height is 2 km). Table 4.10 shows the test results. In the test, the far-zone contribution is evaluated from 0.5° to 180° , summing up the harmonic terms in eqn. (3.6) to degree and order 360. We can see that the far-zone contribution increases significantly with respect to the one for the 1° cap, but the error level is comparable with the 1° cap results shown in Table 4.1. These results imply that a radius of 0.5° for the near-zone cap may be chosen without affecting the accuracy of

Table 4.10: The point-point downward continuation of the synthetic field of degree 21 to degree 1800 derived from GPM98a for $\psi_0 = 0.5^\circ$. Unit: mGal.

Parameter	Min.	Max.	Mean	StdDev	RMS.
Δg_q^{syn}	-12.109	-0.901	-7.624	2.244	7.947
Δg_q^{ddc}	-12.109	-0.860	-7.626	2.245	7.950
$D\Delta g^{syn}$	-1.260	0.135	-0.233	0.242	0.335
$D\Delta g^{ddc}$	-1.192	0.105	-0.235	0.227	0.327
$F_{\Delta q}^{20}$	-0.277	0.470	-0.002	0.159	0.159
δ	-0.068	0.034	0.002	0.017	0.017

the downward continuation if the height of the computation cell is below 2 km.

4.6 Algorithm

The most time consuming part of constructing the linear system of equations is attributed to the evaluation of the doubly averaged modified Poisson kernel in eqn.(3.42). For each equation, there is an average of about 500 coefficients for a grid of $5' \times 5'$, corresponding to 500 evaluations of the kernel. Even for the elementary area of $3^\circ \times 5^\circ$, it takes about one week of CPU time using *Sun Ultra 1 (clock frequency 168MHz)* to evaluate the coefficients.

A more efficient method can be achieved by producing a three-dimensional table for every grid line at the same latitude (see Figure 4.3). The vertical dimension represents height. The doubly averaged kernel values in eqn.(3.44) at different heights for the same latitude and longitude can be approximated by a low degree polynomial with the relative accuracy of better than 1×10^{-4} (cf. Figure 4.4). For the $5' \times 5'$ grid, six tables for the doubly averaged Poisson kernel evaluated at 6 heights ($0.1km$, $0.5km$, $1.0km$, $2.0km$, $3.0km$, $4.0km$) are used to interpolate the doubly averaged kernel values between these heights with the relative accuracy of 1×10^{-4} . For each constant height, there is a two-dimensional table. Each two-dimensional table contains at most

23×28 entries for the $5' \times 5'$ grid, each of which is a product of the doubly averaged modified Poisson kernel and the factor $R/(4\pi(R + H))$. The higher the latitude, the larger the number of entries. This three-dimensional table is then used to compute the coefficients of the system of equations for any height between 0 and 4 km at this latitude by interpolation in real time. The number of the three-dimensional tables is determined by the grid step in latitude and the range of latitude for the area of interest. For example, if the area of interest ranges from 50 to 60 degrees, and the step is $5'$, the range of the tables will be from 49 to 61 degrees, resulting in 144 tables. The additional two degrees are necessary to eliminate the edge effects on the northern and southern borders.

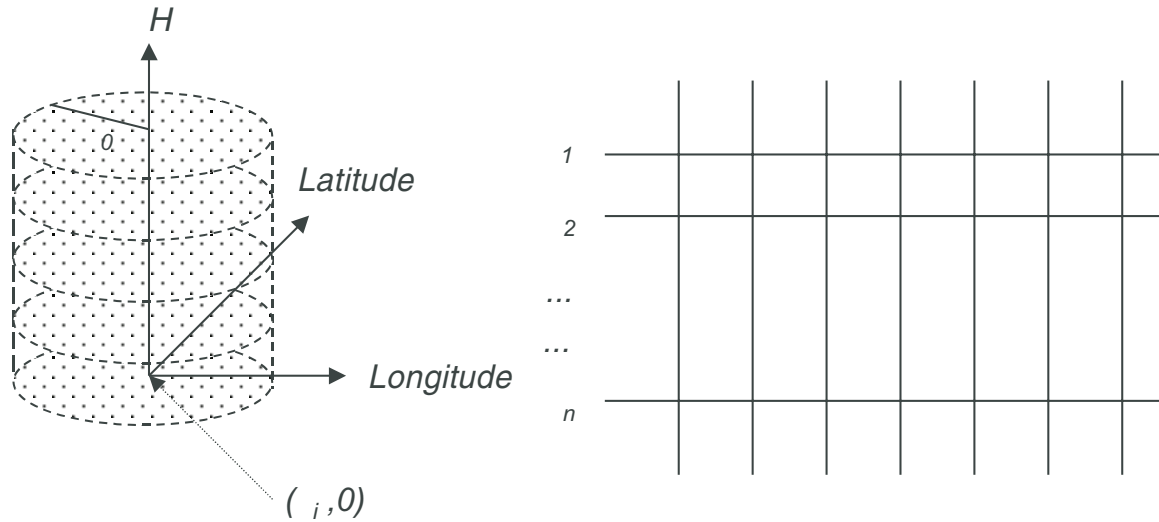


Figure 4.3: The 3-D table for the doubly averaged kernel coefficients $\overline{\overline{B_{ij}}}$.

The discretization of eqn. (3.42) yields one equation for each computation cell. Thus the dimension of the system to be solved depends on the number of cells in the area of interest. In the downward continuation for the geoid determination, we usually deal with a large area and a large system of equations. For example, for an area of $10^\circ \times 10^\circ$ and a grid of $5' \times 5'$, the total number of equations is 14400. If

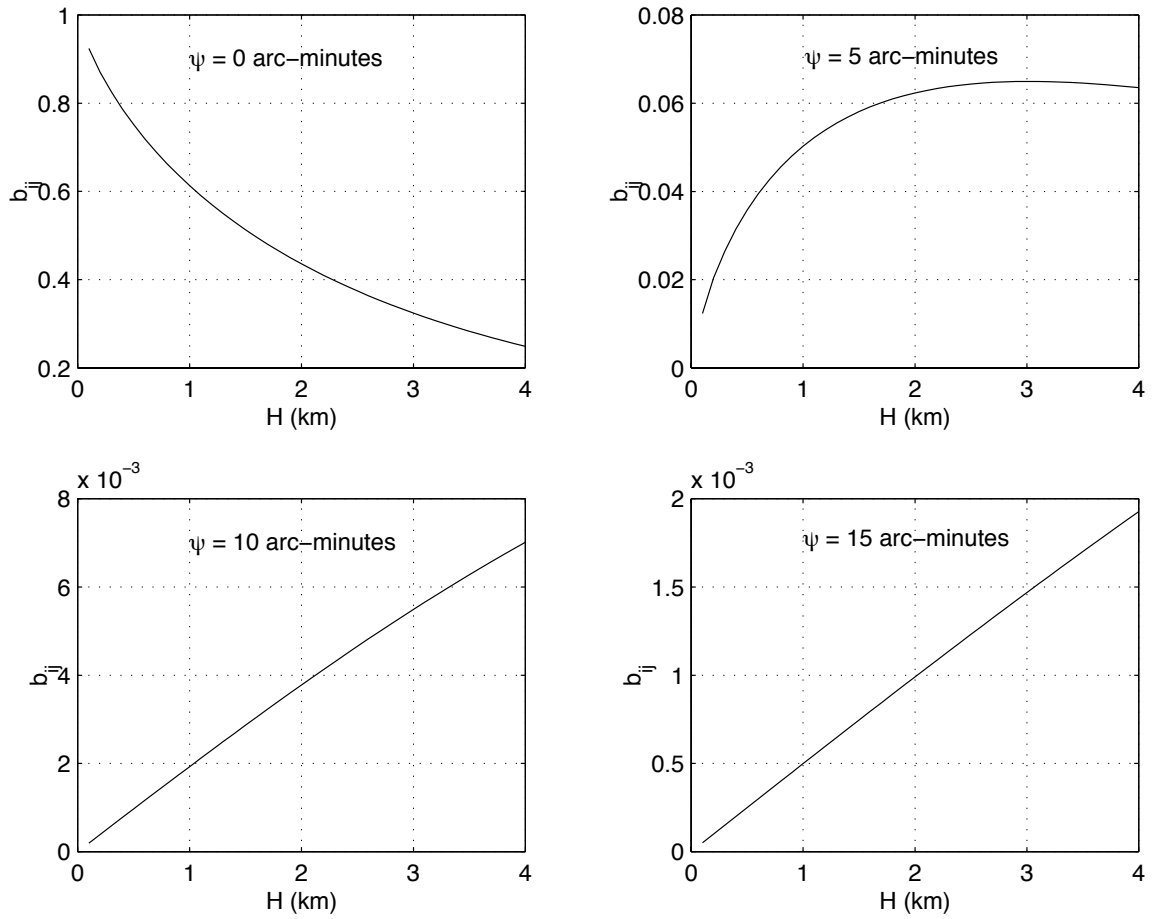


Figure 4.4: The matrix coefficients of the discrete Poisson equation $b_{ij}(= \overline{\overline{B_{ij}}})$ vs. H for different ψ .

each entry in the coefficient matrix were defined as a real type variable (*4Bytes*), the memory size to store the matrix of the system of equations would be almost *800MB*. Even when a compressing technique is adopted, the matrix is still enormous.

In order to avoid handling large matrices, a block-wise approach is adopted here. A block of $3^\circ \times 5^\circ$ is taken as the minimum required area of surface gravity data which results in a block of $1^\circ \times 1^\circ$ of downward continued anomalies. The one-degree border in latitude and the two-degree border in longitude are used to shield the results in the $1^\circ \times 1^\circ$ blocks from the edge effect (Vaníček et al., 1996). The block then moves 1° at a time and goes through the whole area. (see Figure 4.5).

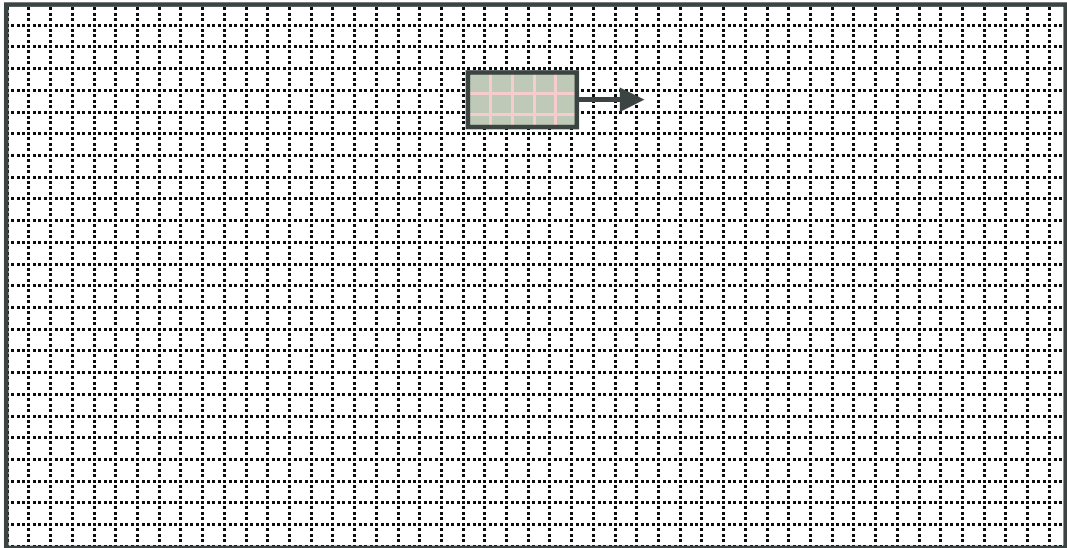


Figure 4.5: The block-wise approach.

For a block of $3^\circ \times 5^\circ$ and a grid of $5' \times 5'$, 2160 linear equations have to be solved. The coefficient matrix of the system is sparse and non-symmetrical. A one-dimensional array is used to store only the non-zero entries of this matrix. This technique saves memory and speeds up computation.

4.7 Implementation: DOWN'97

A software package, DOWN'97 was developed to compute the downward continuation of the mean $5' \times 5'$ residual gravity anomalies ($n > 20$) from the Earth surface to the geoid. The package consists of five separate routines.

1. *tj20.f* (9KB) computes the table of the modified Poisson kernel coefficients.
2. *mQj20.f* (7KB) computes the table of the truncation error coefficients.
3. *dakctbl.f* (32KB) computes the tables of the doubly averaged modified Poisson kernel.
4. *tdgt.f* (10KB) computes truncation errors and prepares the mean gravity anomaly and height files for downward continuation.
5. *down.f* (14KB) downward continues the mean gravity anomalies to the geoid.

The programming language is Fortran77, and a compiler in a UNIX operating system was used to compile all routines during the development of the package.

4.8 The Truncated Singular Value Decomposition Method

For a certain grid step, if the problem becomes ill-conditioned (Martinec, 1996), there is always a way of “regularizing” the solution. There has been a great deal of work devoted to regularization techniques (Tikhonov and Arsenin, 1977; Schwarz, 1978; Rummel et al, 1979; Tarantola, 1987; Xu and Rummel, 1992; Rauhut, 1992; Engels et al., 1993). One common feature among the various techniques is the enforcement of constraints on the solution to produce a stable approximation. These constraints serve as either mathematical conditions or as a-priori information for the solution

being sought. If they are selected in such a way so as to conform to the physical reality, the regularized solution will represent a good approximation to the true one. Another common feature among these techniques is that they are formulated in combination with the least-squares method to reduce random errors in data. For the downward continuation of gravity we do not have redundant data, i.e., the degree of freedom is zero. Thus, the least-squares method does not reduce data random errors in the data, while it increases the mathematical complexity.

Hansen (1987, 1990, 1992) suggested another regularization method in his series of papers. This method is called the Truncated Singular Value Decomposition (TSVD) and is solidly based on both the Singular Value Expansion (SVE) and the Singular Value Decomposition (SVD). The TSVD is particularly suitable for the inverse Poisson problem. The superiority of the TSVD is that it provides the best approximation to the true solution from the spectral point of view, while taking into consideration the data errors. It is the spectral property that makes this method theoretically and practically more tangible than other methods for the application of the downward continuation, because it makes regularization solution physically and mathematically more meaningful.

Let B be a matrix of $n \times n$, that has a singular value decomposition in the form (Golub and Van Loan, 1989)

$$B = U\Sigma V^T = \sum_{i=1}^n \sigma_i \mathbf{u}_i \mathbf{v}_i^T, \quad (4.4)$$

where the left and right singular vectors \mathbf{u}_i and \mathbf{v}_i are the orthonormal columns of the matrices $U \in \mathcal{R}^{n \times n}$ and $V \in \mathcal{R}^{n \times n}$, and the singular values σ_i are the elements of the diagonal matrix $\Sigma \in \mathcal{R}^{n \times n}$. They satisfy $\sigma_1 \geq \sigma_2 \geq \dots \geq \sigma_n$. Then the truncated singular value decomposition solution of the downward continuation can be constructed as

$$\mathbf{f} = \sum_{i=1}^k \frac{\langle \mathbf{u}_i^T, \mathbf{g} \rangle}{\sigma_i} \mathbf{v}_i \quad i = 1, \dots, n; \quad k \leq n, \quad (4.5)$$

where k is the truncation parameter. It has a similar form to the truncated solution of the continuous inverse Poisson problem

$$g(R, \Omega) = \sum_{n=0}^k \sum_{m=-n}^k \frac{\langle Y_{nm}(\Omega), g(r, \Omega) \rangle}{\lambda_n} Y_{nm}(\Omega), \quad (4.6)$$

where \langle, \rangle indicates the inner product.

The SVD of B is related to the SVE of the Poisson kernel K in the sense that σ_i and $\langle \mathbf{u}_i^T, \mathbf{g} \rangle$ correspond to λ_n and $\langle Y_{nm}(\Omega), g(r, \Omega) \rangle$, respectively (Hansen, 1992). This similarity establishes a heuristic link between the discrete and continuous inverse Poisson problems, and calls for a physical interpretation of the discrete Poisson downward continuation problem. First of all, it means that larger σ_i correspond to low-degree components, while smaller σ_i correspond to high-degree components. Secondly, the small amount of information in \mathbf{g} associated with all the small singular values is lost due to the presence of errors. Hence, one can say that the system is essentially underdetermined or ill-conditioned, because we are only able to recover the information associated with the larger singular values of B . The truncation parameter k is determined in such a way so that the noise-dominated high-degree components are filtered out of the solution. Thirdly, the left and right singular vectors \mathbf{u}_i and \mathbf{v}_i tend to oscillate more frequently with increasing i .

Therefore, the TSVD regularization provides a stepwise way to approach the true solution from low-degree components to high-degree components. In practice, we increase k until the residual quadratic norm is of the same size as the quadratic norm of the errors $\|\mathbf{e}\|^2$.

4.9 Summary

The inverse Poisson problem can be reduced to a linear system of algebraic equations for a discrete model. The coefficient matrix of the system is large and sparse. The iterative method is the most efficient to solve the system. The combined iterative

method was proposed to speed up convergence.

The synthetic approach was used to evaluate the point-point, point-mean and mean-mean models. GPM98a was adopted to generate synthetic data. The tests showed that the mean-mean model gives a result sufficiently close to the mean-mean synthetic solution when the averaging error is accounted for. Synthetic tests also show that the 0.5° may be chosen as the radius of the near-zone cap when the maximum elevation does not exceed 2 km.

A block-wise technique was developed to avoid solving a large system of equations, and to improve the computational speed of the discrete Poisson downward continuation. The coefficient interpolation method was implemented to reduce the CPU time when evaluating the doubly averaged Poisson kernel.

The software package DOWN'97 was developed to evaluate the discrete Poisson downward continuation of the mean $5' \times 5'$ gravity anomalies.

When the coefficient matrix is very close to singular, the iterative approach may fail to give a useful solution. The truncated singular value decomposition (TSVD) was proposed to provide an optimal solution from noisy data. The TSVD is superior to other regularization methods since it makes the process of solving the system physically and mathematically meaningful.

Chapter 5

Analytical Downward Continuation

5.1 Theory

The analytical downward continuation (ADC) is based on the Taylor series expansion of the gravity anomaly. One open question is whether it leads to a solution that is as good as the discrete Poisson downward continuation (DDC) when the disturbing potential is harmonic in the domain above the geoid. In this chapter, a numerical analysis is conducted to answer this question.

If $\Delta g(r_g, \Omega)$ is known on the geoid at r_g and has derivatives of all orders $\Delta g^{(n)}(r_g, \Omega)$ in the closed interval $[r_g, r]$, then

$$\Delta g(r, \Omega) = \sum_{n=0}^{\infty} \frac{\Delta g^{(n)}(r_g, \Omega)}{n!} \Big|_{r=r_g} H^n. \quad (5.1)$$

This series may be symbolically written as

$$\Delta g(r, \Omega) = U \Delta g(r_g, \Omega), \quad (5.2)$$

where the symbol U denotes the upward continuation operator which is applied to the function $\Delta g(r, \Omega)$ at r_g .

Given $\Delta g(r_t, \Omega)$ at the Earth surface, the solution of $\Delta g(r_g, \Omega)$ on the geoid can

be expressed as follows (Moritz, 1980, section 45)

$$\Delta g(r_g, \Omega) = \sum_{n=0}^{\infty} g_n, \quad (5.3)$$

where

$$\begin{aligned} g_0 &= \Delta g(r_t, \Omega), \\ g_1 &= -H \cdot L_1(g_0), \\ g_2 &= -H \cdot L_1(g_1) - H^2 \cdot L_2(g_0), \\ &\dots \\ g_n &= -\sum_{r=1}^n H^r \cdot L_r(g_{n-r}). \end{aligned} \quad (5.4)$$

with an L operator

$$L(g) = \frac{R^2}{2\pi} \int_{\Omega'} \frac{g - g_p}{d^3} d\Omega' - \frac{1}{R} g_p, \quad (5.5)$$

$$L_n = \frac{1}{n!} L^n = \frac{1}{n} L L_{n-1}, \quad (5.6)$$

and $d = 2R \sin(\psi/2)$ is the distance between the computation point P and an integration point.

The operator L may be interpreted as a vertical gradient on a spherical surface if the gravity anomaly is known on the surface. However, for the downward continuation, it merely represents the first-order approximation to the gradient since the gravity anomaly is known on the irregular Earth surface. Eqn. (5.6) shows that the higher-order terms L_n can be recursively evaluated from the lower-order terms L_{n-1} . This relation can be used in the computation.

The analytical downward continuation is a forward problem. It is divergent with increasing resolution¹. What kind of relation exists between the instability of the inverse Poisson problem and the divergence of the analytical continuation is still an open question. As far as the convergence is concerned, a deep and extensive discussion can be found in the literature (Moritz, 1980; Jekeli, 1983). This issue will not be discussed here. The main question to be answered by this research is whether both methods are numerically equivalent.

¹Vaníček, 2000. personal communication.

5.2 Computational Method

The analytical downward continuation requires a number of evaluations of the convolution integral (5.5) depending on the number of terms taken. If we take n up to 5, the integral (5.5) will be evaluated 15 times in the region of interest. Thus, an efficient numerical algorithm is needed for its evaluation.

Similar to the Stokes kernel, the L operator kernel is a function of the spherical distance ψ which can be expressed as

$$\psi = \arccos [\sin \phi \sin \phi' + \cos \phi \cos \phi' \cos (\lambda' - \lambda)], \quad (5.7)$$

where ϕ and λ are the latitude and longitude of the computation point P, respectively, ϕ' and λ' are the latitude and longitude of the integration point, respectively. The 1-D FFT was applied by Sideris (1987) for the evaluation of the integral (5.5).

Recently, an alternative algorithm was suggested to evaluate this type of integral (Huang et al., 2000). Its computational complexity is $O(N)$ in contrast to $O(N \log N)$ of the FFT. Its practical speed is comparable to the FFT technique. The basic idea is to make use of the isotropic and symmetrical properties of the kernel with respect to longitude. It can be seen that the spherical distance does not depend on the longitude of the computation and integration points; it only depends on the longitude difference between the two points. This means that the kernel values need only be computed once for the evenly spaced points at the same latitude. In other words, all computation points at the same latitude use the same set of kernel values. In addition, the kernel values are symmetrical with respect to the meridian of the computation point, and thus only one-half of the kernel values need be evaluated. Furthermore, for constant grid steps $d\lambda'$, $d\phi'$, the surface element $d\sigma = \cos \phi' d\lambda' d\phi'$ evidently depends only on the latitude of the integration point, and needs be computed only once for each integration latitude. Compared to the 1-D FFT, this method is more straightforward and suitable for the evaluation of the L integral. It has been implemented in a computer software package for the evaluation of the analytical downward continuation

in this research.

5.3 Numerical Comparisons with the Discrete Poisson Downward Continuation

The point-point model of the Poisson downward continuation is used for the comparisons to be consistent with the analytical downward continuation that is usually formulated as the point-point model.

5.3.1 Synthetic Comparisons

Two synthetic data sets were generated from EGM96 and GPM98a, respectively, on a $5' \times 5'$ grid as point values. The synthetic data from EGM96 were evaluated from degree and order 21 to degree and order 360, while the synthetic data from GPM98a were computed from degree and order 21 to degree and order 1800. Each data set includes the synthetic gravity anomalies both on the Earth surface and on the geoid. The synthetic data evaluated on the Earth surface were used as input to the downward continuation computation, while the synthetic data evaluated on the geoid were used to verify the accuracy of the computation. The first 20 degrees of harmonic components were excluded from the computation by following the combined technique shown in eqn. (3.5).

The test region covers the Rocky Mountains, delimited by latitudes $41^\circ N$ and $62^\circ N$ and longitudes $100^\circ W$ and $138^\circ W$. The mean $5' \times 5'$ heights range from 0 m to 3576 m with a mean of 711 m and a standard deviation of 622 m. The first rows in Tables 5.1 and 5.4 contain statistical information of the two synthetic data sets on the geoid.

Table 5.1 shows the point-point DDC results from the EGM96 synthetic data. In the Table, superscript ‘syn’ indicates synthetic data, ‘ddc’ indicates discrete Poisson

downward continuation, $D\Delta g$ indicates downward continuation contribution, and δ indicates the error of the downward continuation. From this table, we can see that the DDC gives the results that agree with the synthetic data within (-0.15 mGal, 0.16 mGal).

After the downward-continued synthetic gravity anomalies are transformed into geoid heights by Stokes integration, the maximum error of the geoid heights is about 0.3 cm, while the maximum downward continuation contribution is about 21 cm (see Figure 5.1 and Table 5.3). Figure 5.2 shows the effect of the DDC on the geoid heights in the Rocky Mountains. The geoid results are restricted to a region of $5^\circ \times 10^\circ$ (49°N - 54°N , 114°W - 124°W). Their spatial pattern is highly correlated with the geoid heights in the region, characterized by dominant long-wavelength features.

Table 5.2 shows the ADC results. Superscript ‘adc’ indicates analytical downward continuation. In the computation, the L integral was truncated to 6° . It can be seen that the ADC demonstrates a rapid convergence to the synthetic data from the g_1 to g_3 term within an error range of (-0.48 mGal, 0.95 mGal). The maximum ADC error on the geoid heights is about 2 cm, six times greater than the DDC one (see Figure 5.1 and Table 5.3). This error may be caused by the truncation of the series, the truncation of the L integral and the ADC method itself. Figure 5.3 shows effects of the ADC on the geoid in the Rocky Mountains. It is very similar to the DDC results shown in Figure 5.2.

The same comparison was carried out using GPM98a up to degree 1800. In the DDC computation, the far-zone contribution was summed up to degree 360 instead of 1800. The results (Tables 5.4, 5.5 and 5.6; Figures 5.4, 5.5 and 5.6) simply reconfirm the conclusions drawn from the previous EGM96 comparison. The main reason for the similar conclusions from both the EGM96 and GPM98a tests is that the higher degree components of GPM98a do not produce a significant contribution to the Earth geopotential. This is also the limitation of any synthetic geopotential model based on the Kaula-type degree-variance models of the Earth gravity field (Kaula, 1966;

Table 5.1: The point-point DDC of the synthetic field of EGM96 (21-360) in the test region. Unit: mGal.

Parameter	Min.	Max.	Mean	StdDev	RMS.
Δg_q^{syn}	-73.219	88.868	0.125	14.088	14.089
Δg_q^{ddc}	-73.073	88.717	0.124	14.081	14.082
$D\Delta g^{syn}$	-4.851	8.732	0.051	0.515	0.517
$D\Delta g^{ddc}$	-4.705	8.576	0.051	0.504	0.506
Dg_T	-0.144	0.181	0.004	0.027	0.027
δ	-0.146	0.163	0.001	0.012	0.012

Table 5.2: The ADC of the synthetic field of EGM96 (21-360) in the test region. Unit: mGal.

Parameter	Min.	Max.	Mean	StdDev	RMS.
Δg_q^{syn}	-73.219	88.868	0.125	14.088	14.089
Δg_q^{adc}	-72.754	88.049	0.118	14.049	14.049
$D\Delta g^{syn}$	-4.851	8.732	0.051	0.515	0.517
g_1	-4.168	7.259	0.044	0.443	0.445
g_2	-0.203	0.765	0.000	0.021	0.021
g_3	-0.043	0.142	0.000	0.003	0.003
$D\Delta g^{adc}$	-4.386	7.868	0.044	0.461	0.463
δ	-0.480	0.952	0.007	0.056	0.056

Table 5.3: Accuracy of the point-point DDC and the ADC by using the synthetic field of EGM96 (21-360) in the test region. Unit: m.

Parameter	Min.	Max.	Mean	StdDev	RMS.
N_{dc}^{syn}	0.015	0.209	0.064	0.030	0.071
δ_N^{ddc}	0.000	0.003	0.001	0.001	0.001
δ_N^{adc}	0.000	0.020	0.007	0.04	0.008

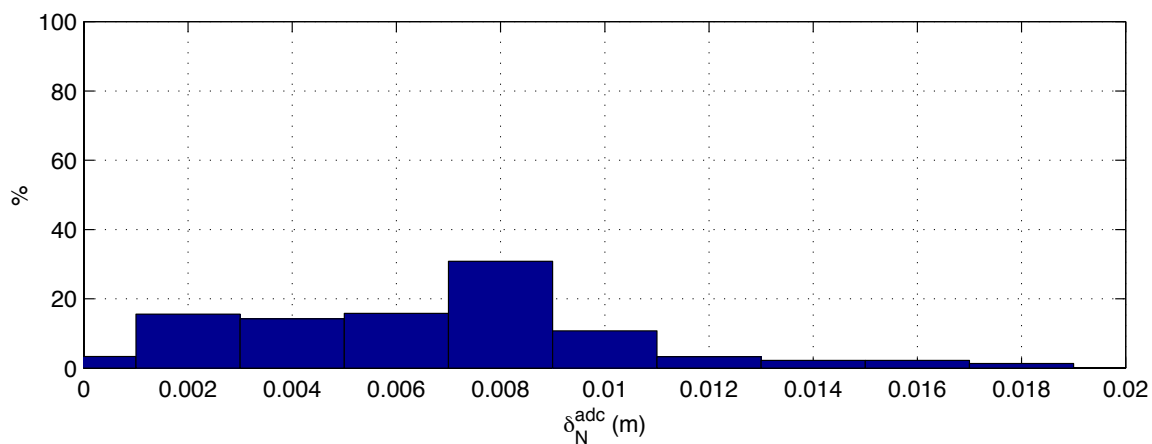
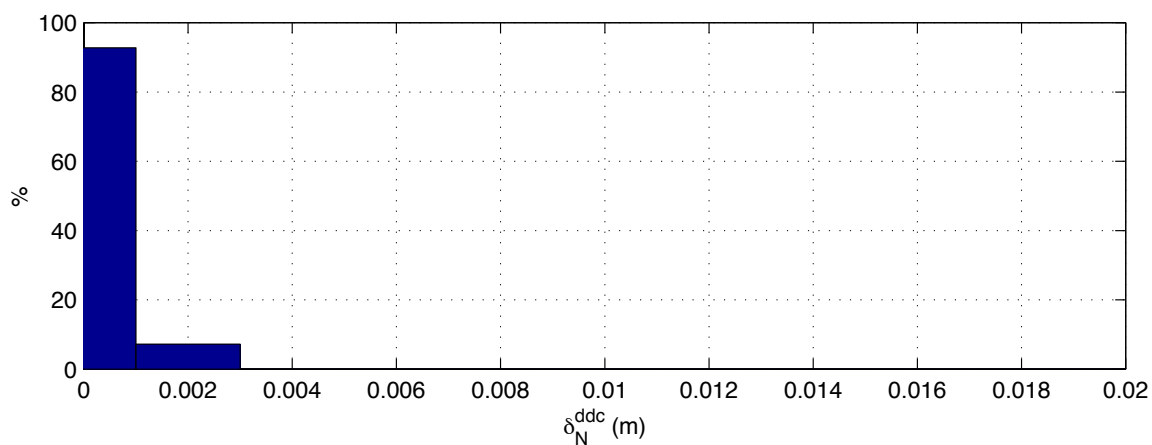


Figure 5.1: The geoid height error distribution for the DDC and ADC of the EGM96 synthetic data.

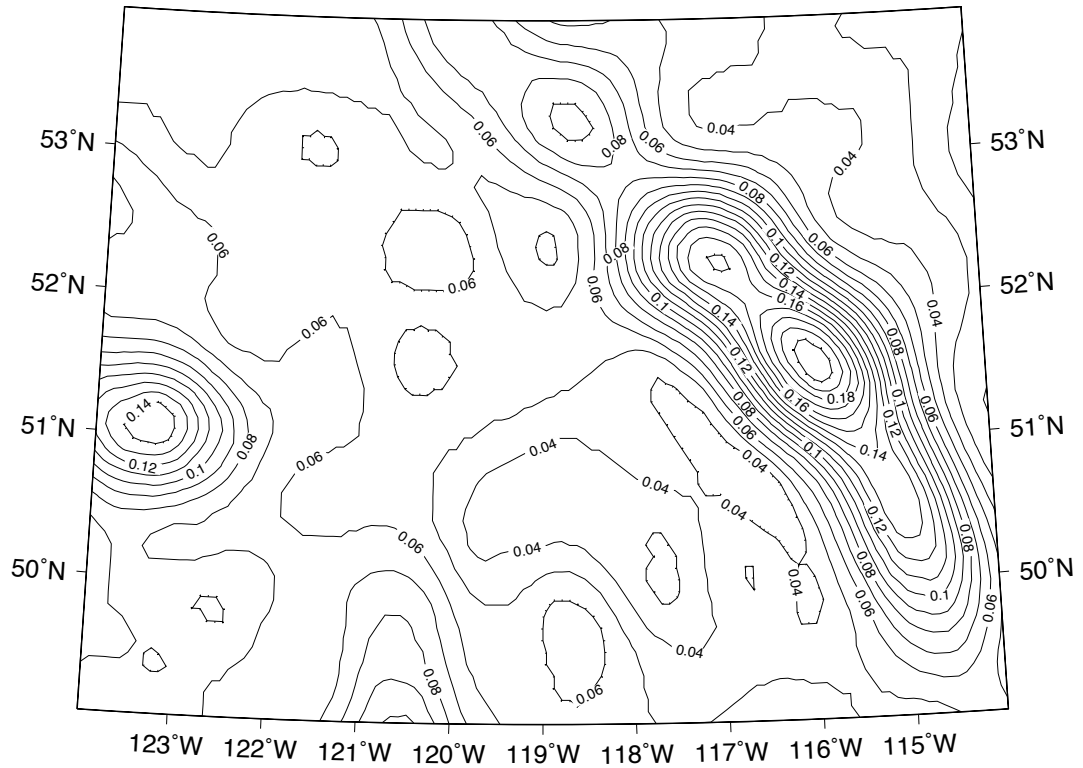


Figure 5.2: The point-point DDC effect on the geoid from the synthetic gravity data of EGM96 (21-360). Contour interval: 0.01 m.

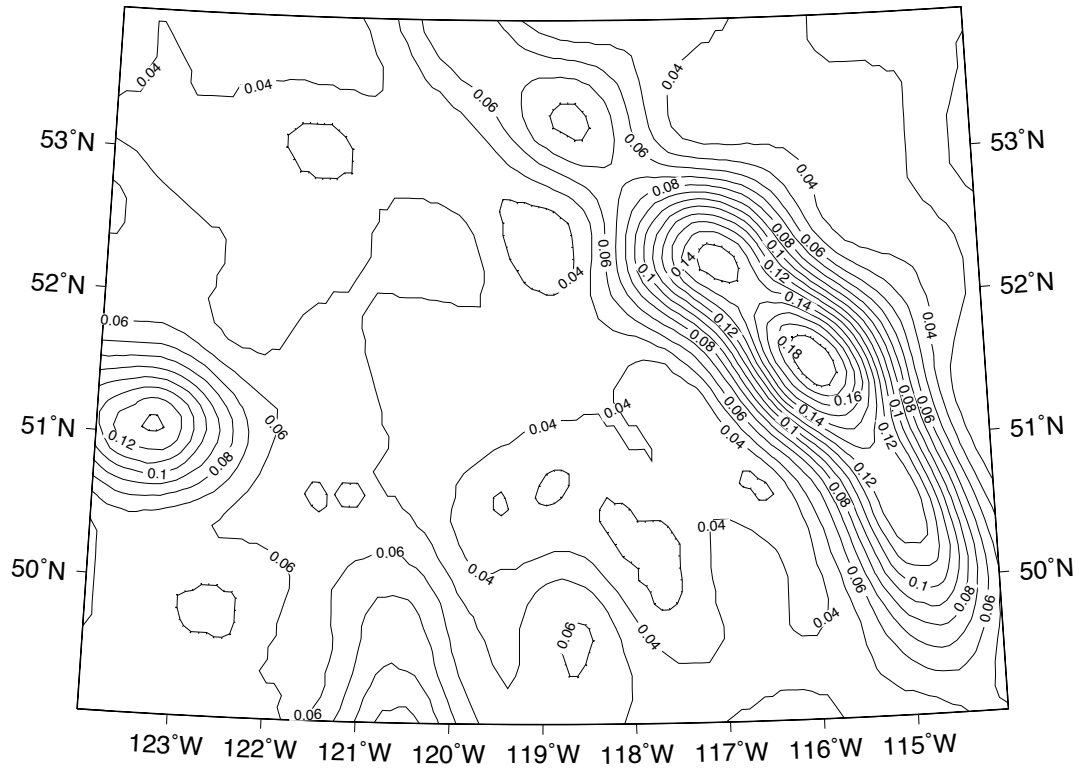


Figure 5.3: The ADC effect on the geoid from the synthetic gravity data of EGM96 (21-360). Contour interval: 0.01 m.

Tscherning and Rapp, 1974; Jekeli, 1978). For instance, these degree-variance models may not be applicable as models for the gravity anomaly based on the Helmert 2nd condensation. In the next section, the Helmert gravity anomaly will be used to further study the relation between the two methods.

Table 5.4: The point-point DDC of the synthetic field of GPM98a (21-1800) in the test region. Unit: mGal.

Parameter	Min.	Max.	Mean	StdDev	RMS.
Δg_q^{syn}	-69.692	124.378	0.176	13.986	13.987
Δg_q^{ddc}	-69.268	124.096	0.175	13.971	13.973
$D\Delta g^{syn}$	-7.271	16.048	0.046	0.760	0.762
$D\Delta g^{ddc}$	-6.881	15.588	0.045	0.728	0.729
Dg_T	-0.196	0.192	0.003	0.026	0.026
δ	-0.726	0.726	0.000	0.046	0.046

Table 5.5: The ADC of the synthetic field of GPM98a (21-1800) in the test region. Unit: mGal.

Parameter	Min.	Max.	Mean	StdDev	RMS.
Δg_q^{syn}	-69.292	124.378	0.176	13.986	13.987
Δg_q^{adc}	-69.263	122.935	0.170	13.929	12.931
$D\Delta g^{syn}$	-7.271	16.048	0.046	0.760	0.762
g_1	-5.344	12.495	0.040	0.615	0.617
g_2	-0.719	1.452	0.000	0.049	0.049
g_3	-0.096	0.263	0.000	0.005	0.005
$D\Delta g^{adc}$	-6.150	13.864	0.040	0.659	0.660
δ	-1.288	2.324	0.006	0.110	0.110

Table 5.6: Accuracy of the point-point DDC and the ADC by using the synthetic field of GPM98a (21-1800) in the test region. Unit: m.

Parameter	Min.	Max.	Mean	StdDev	RMS.
N_{dc}^{syn}	0.004	0.141	0.040	0.021	0.045
δ_N^{ddc}	-0.001	0.002	0.000	0.000	0.000
δ_N^{adc}	-0.003	0.013	0.003	0.003	0.005

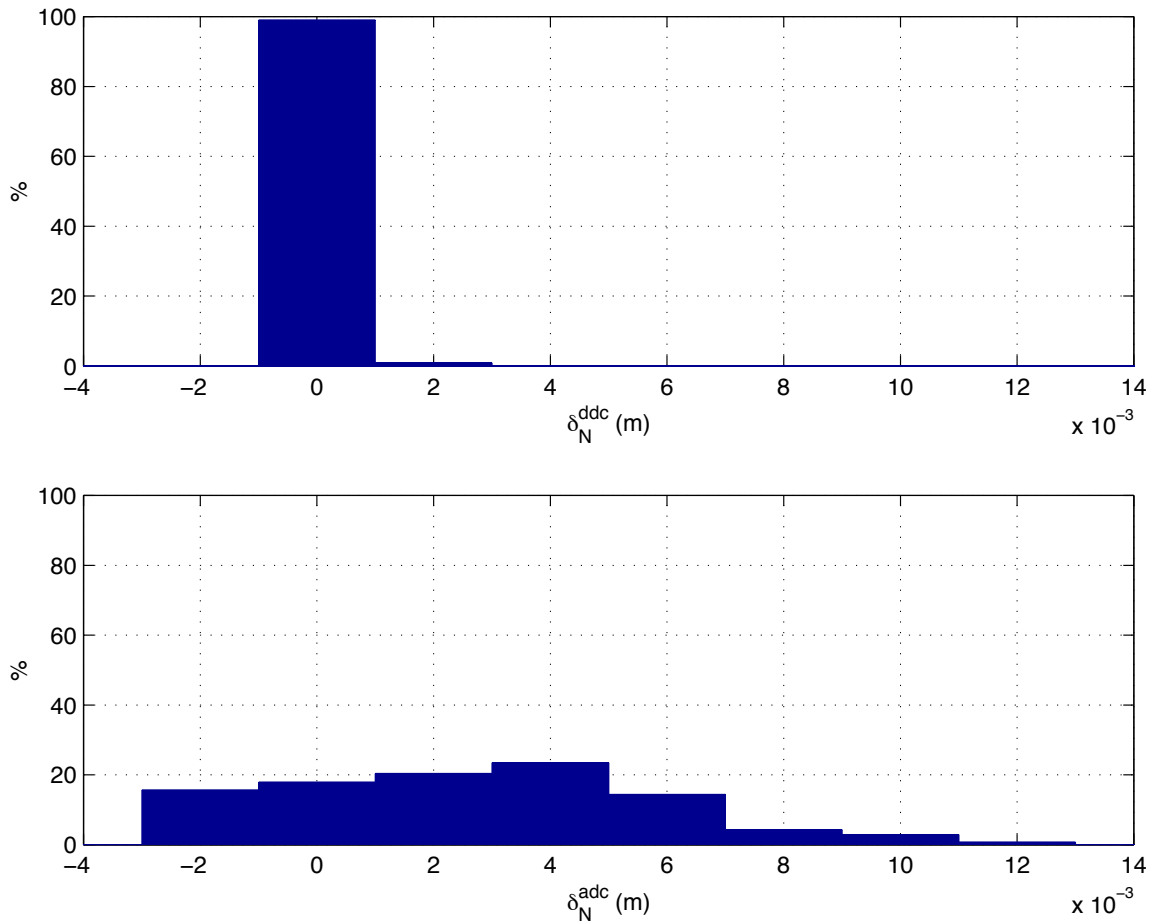


Figure 5.4: The geoid height error distribution for the DDC and ADC of the GPM98a synthetic data.

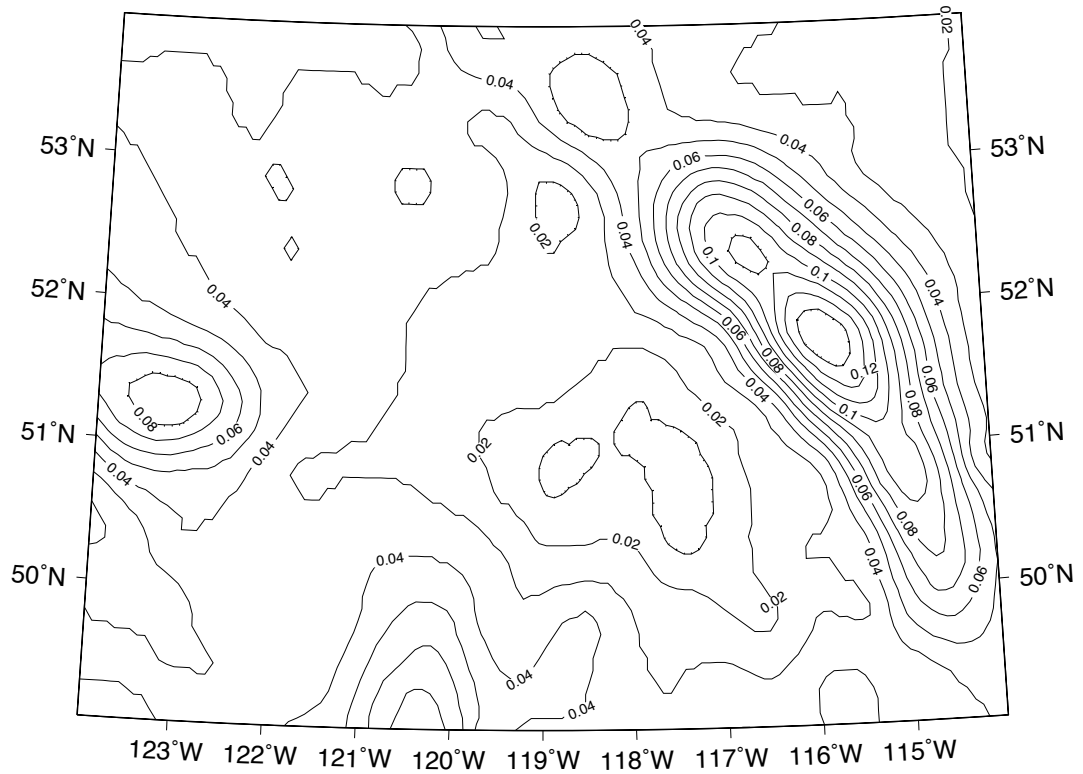


Figure 5.5: The point-point DDC effect on the geoid from the synthetic gravity data of GPM98a (21-1800). Contour interval: 0.01 m.

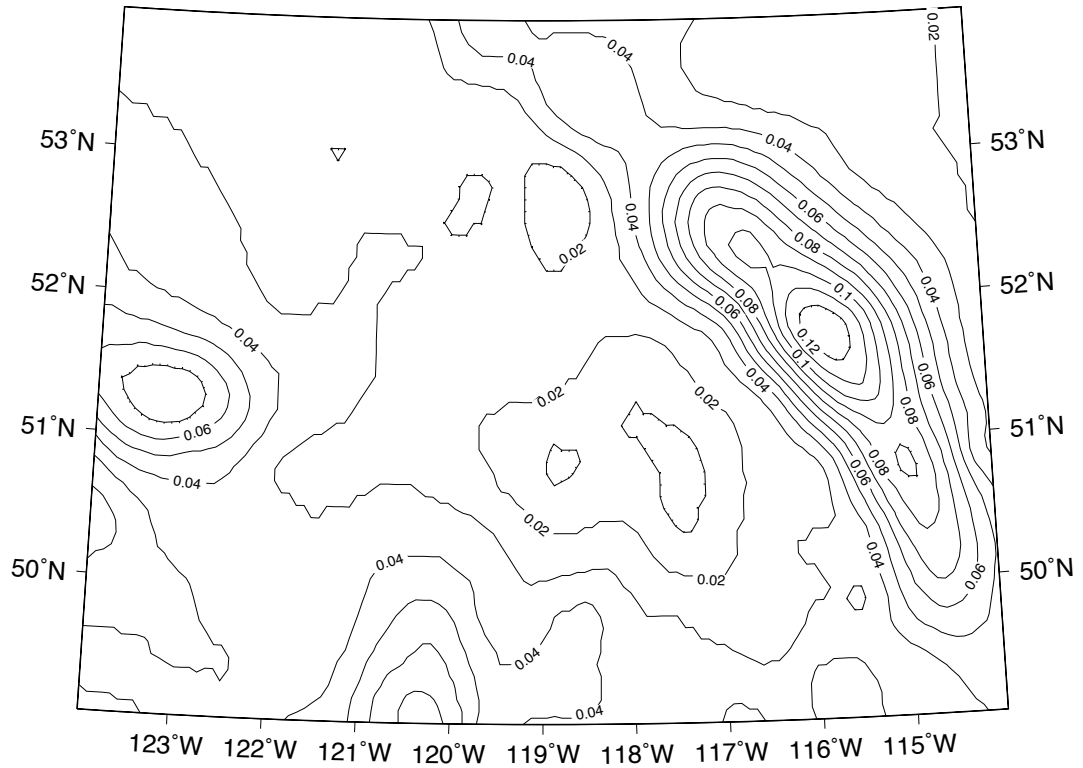


Figure 5.6: The ADC effect on the geoid from the synthetic gravity data of GPM98a (21-1800). Contour interval: 0.01 m.

5.3.2 Comparisons Using the Helmert Gravity Anomaly

Helmert's 2nd condensation has been used in the practical determination of the geoid (Vaníček and Kleusberg, 1987; Véronneau, 1996; Smith and Milbert, 1999). Following this approach, the Helmert gravity anomaly needs to be downward continued from the Earth surface to the geoid. The procedure and formulae for evaluation of the Helmert gravity anomaly can be found in Vaníček et al. (1999). In this section, the DDC and the ADC are compared by using the Helmert gravity anomaly.

The mean $5' \times 5'$ Helmert gravity anomalies were retrieved from the UNB Helmert gravity data set in the same region as the one for the synthetic comparisons ². The mean $30'' \times 30''$ DEM data were used for the evaluation of the mean $5' \times 5'$ Helmert gravity anomalies. Table 5.7 shows statistical information of the residual Helmert gravity anomalies above degree 20 and the DEM data in the test region. Compared to the synthetic data generated from the global geopotential models, the residual Helmert gravity anomaly is significantly larger in both magnitude and RMS.

Table 5.8 shows the DDC and the ADC gravity results. In the DDC, the far-zone contribution was neglected since it required the Helmertized global geopotential model that was not available. This omission results in a larger DDC effect as expected. The far-zone contribution from the non-Helmertized EGM96 is about 1 cm on average in the test region as shown in Figure 3.6. Further work is needed to estimate the far-zone contribution from the Helmertized global geopotential model. The ADC was truncated up to the 5th term, displaying a rapid convergence. In the computation, the L integral was truncated to 6° . Since the ADC is a forward problem, omission of the far-zone effect may weaken the ADC effect, therefore, the ADC may appear smaller than what it should be. The last row in Table 5.8 shows the statistics of the differences between the DDC and ADC gravity results. It shows that the ADC is about 10% smaller than the DDC on average.

Table 5.9 shows the effects of the DDC and the ADC on the geoid. It is noticeable

²Janák, J. (2000). personal communication.

that the ADC geoid result converges significantly faster than the ADC gravity one. The terms above the 3rd are invisible in the geoid result at the millimeter level. The DDC geoid result is 5 cm larger, on average, than the ADC one (see Figures 5.7, 5.8 and 5.9).

Table 5.7: Statistics of the residual Helmert gravity anomaly above degree 20 of EGM96 and the height data in the test region.

Parameter	Min.	Max.	Mean	StdDev	RMS.
$\Delta g_t^h (mgal)$	-132.620	260.181	-2.241	23.623	23.729
$H(m)$	0	3567	711	623	945

Table 5.8: The gravity results of the DDC and the ADC from the residual Helmert gravity anomaly in the test region. Unit: mGal.

Parameter	Min.	Max.	Mean	StdDev	RMS.
$D\Delta g^{ddc}$	-23.086	56.582	0.355	3.506	3.524
g_1	-16.533	38.775	0.320	2.639	2.659
g_2	-3.370	6.891	0.000	0.374	0.374
g_3	-0.566	1.349	0.000	0.052	0.052
g_4	-0.112	0.246	0.000	0.007	0.007
g_5	-0.021	0.039	0.000	0.001	0.001
$D\Delta g^{adc}$	-19.500	47.300	0.320	3.010	3.027
$D\Delta g^{ddc} - D\Delta g^{adc}$	-4.569	10.132	0.035	0.549	0.550

5.4 Summary

In addition to the discrete Poisson downward continuation (DDC), there exists a well-developed method, called the analytical downward continuation (ADC) that is based on the Taylor series expansion of the gravity anomaly.

The synthetic tests on the basis of EGM96 and GPM98a show that the ADC introduces an error of about 10% of the downward continuation effect, while the

Table 5.9: The geoid height results of the DDC and the ADC from the residual Helmert gravity anomaly in the test region. Unit: m.

Parameter	Min.	Max.	Mean	StdDev	RMS.
N_{ddc}	0.175	0.798	0.542	0.124	0.556
N_{g_1}	0.172	0.703	0.494	0.103	0.506
N_{g_2}	-0.013	0.018	-0.002	0.003	0.004
N_{g_3}	-0.002	0.003	0.000	0.000	0.000
N_{g_4}	0.000	0.000	0.000	0.000	0.000
N_{g_5}	0.000	0.000	0.000	0.000	0.000
N_{adc}	0.171	0.712	0.492	0.109	0.504
$N_{ddc}-N_{adc}$	0.004	0.092	0.050	0.017	0.053

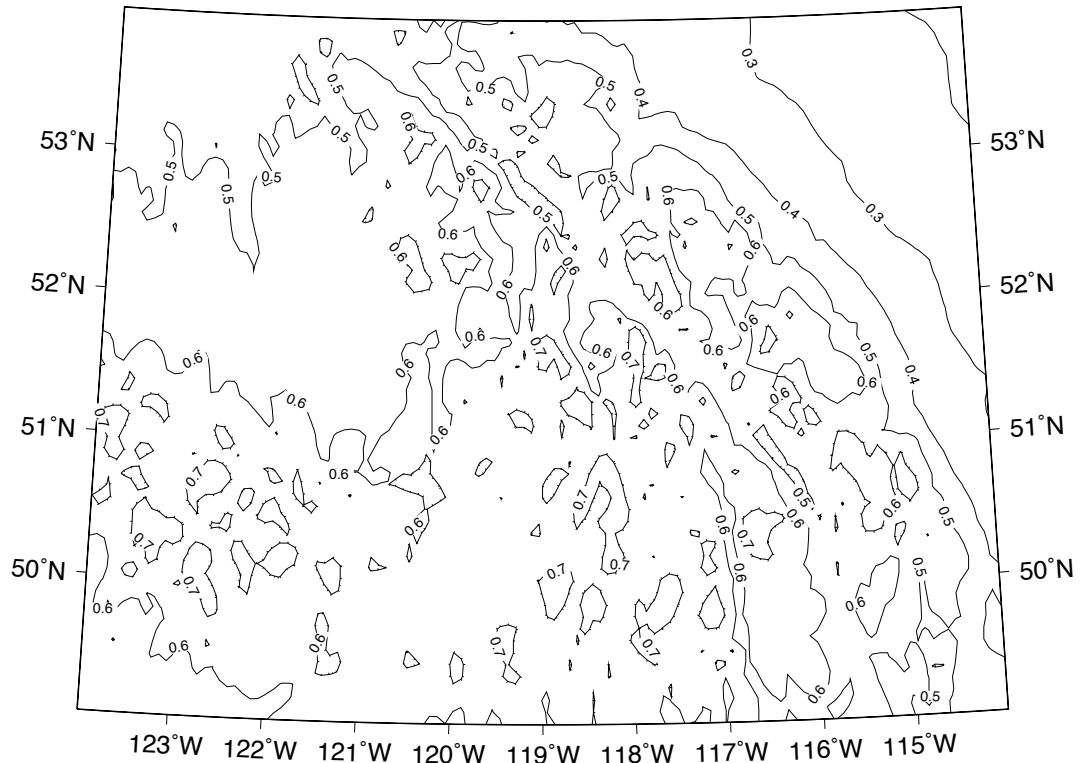


Figure 5.7: The point-point DDC effect on the geoid, using the residual Helmert gravity anomalies above degree 20 of EGM96. Contour interval: 0.1 m.

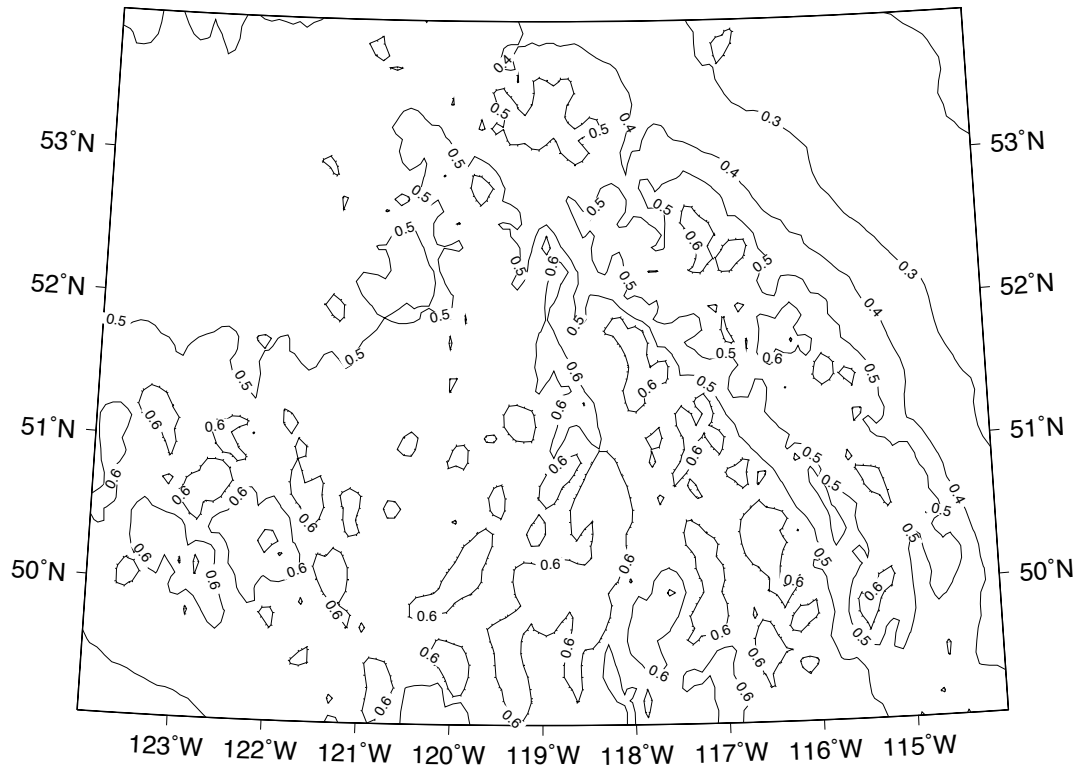


Figure 5.8: The ADC effect on the geoid, using the residual Helmert gravity anomalies above degree 20 of EGM96. Contour interval: 0.1 m.

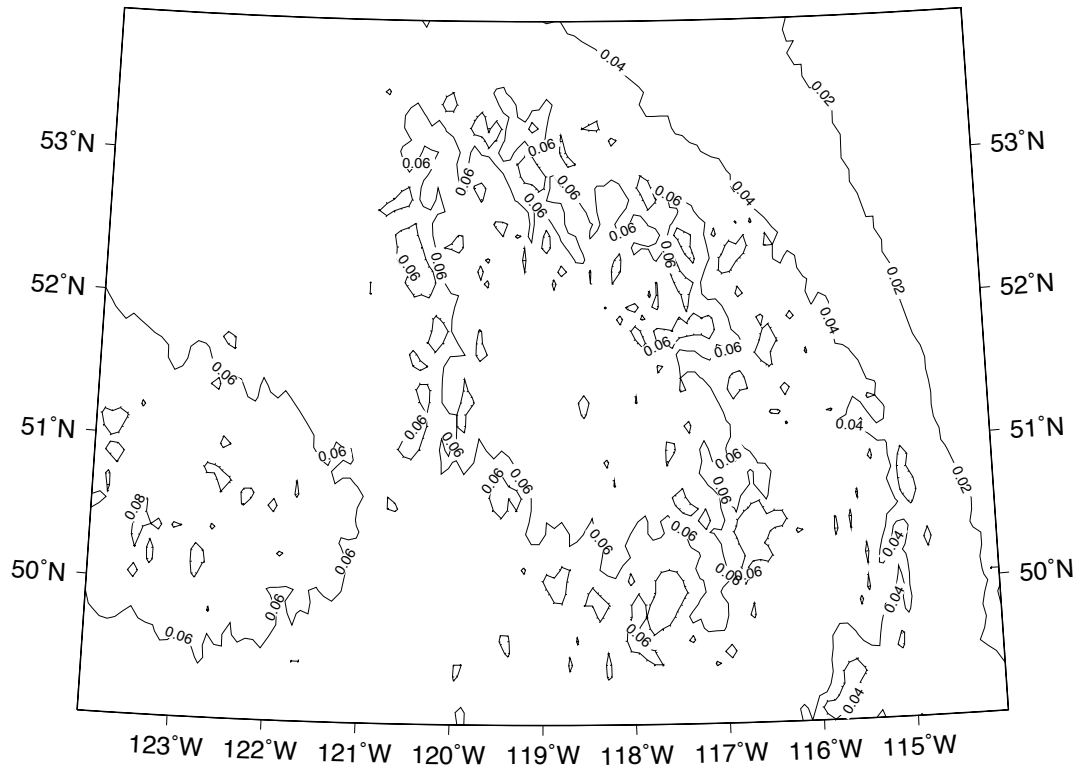


Figure 5.9: The difference between the DDC and ADC effects on the geoid, using the residual Helmert gravity anomalies. Contour interval: 0.02 m.

error of the DDC is smaller than 1 cm in the geoid height. The test using the residual Helmert anomaly in the Rocky Mountains shows that the maximum difference between the two methods can reach 10 mGal in gravity, and about 10 cm in the geoid height. The DDC values are 5 cm larger than the ADC ones on average in the geoid height. The difference accounts for about 10% of the downward continuation contribution.

An ultra-high degree synthetic global geopotential model constrained to the Kaula-type degree-variance models is too smooth to simulate the Helmert gravity anomaly, especially in mountainous areas.

Chapter 6

Topographical Density Variation Effects on Gravity and the Geoid

6.1 Introduction

The existence of topography and atmosphere above the geoid violates the basic assumption of the Stokes formula for the determination of the geoid. However, Helmert's 2nd condensation method can be applied to satisfy the requirements of the Stokes formula (cf. Figure 1.2).

Helmert's 2nd condensation method has been used to determine the geoid in Canada and the US (Vaníček et al. 1995; Véronneau 1996; Smith and Milbert 1999). This approach conceptually consists of the following steps (Najafi, 1996; Vaníček et al. 1999):

1. Transformation of the 'observed gravity anomaly' Δg_t on the Earth surface from the real space into Helmert's gravity anomaly Δg_t^h , in Helmert's space.
2. Downward continuation of Δg_t^h to the Helmert co-geoid.
3. Solution of the boundary value problem in Helmert's space, i.e., solution for the

Helmert co-geoid using the generalized Stokes formula (Vaníček and Sjöberg 1991).

4. Transformation of the co-geoid (in Helmert's space) to the geoid (in real space) by evaluating the primary indirect topographical effect (PITE).

The transformation of the gravity anomalies from the real space to Helmert's space is given by (omitting atmospherical effects) (Vaníček et al. 1999)

$$\Delta g^h(r_t, \Omega) = \Delta g(\Omega) + \frac{2}{R}H(\Omega)\Delta g^B(\Omega) + \delta A(r_t, \Omega) + \delta\gamma(r_t, \Omega), \quad (6.1)$$

where Δg is the free-air gravity anomaly, the second term is a correction for the difference between the quasigeoid and the geoid, δA is the direct topographical effect (DTE), $\delta\gamma$ is the secondary indirect topographical effect (SITE), Δg^B is the simple Bouguer gravity anomaly. The DTE is a correction to gravity for condensing the topographical mass to the Helmert layer. The SITE is a correction to gravity for the change of the telluroid due to condensation of the topographical mass. Sjöberg (Eqs. (70)-(73), 2000) formulates an identical transformation to eqn. (6.1), but the second term of eqn. (6.1) is not explicitly given.

In this approach, topography affects geoid modeling through the terms DTE, SITE, and PITE. The evaluation of these terms requires a digital elevation model (DEM) and a digital topographical density model (DTDM). While DTM of high resolution are readily available, this is not the case for the DTDM. This is the reason the constant topographical density (2.67 g/cm^3) has been used in practice to approximate the real density. The real density varies from 1.0 g/cm^3 (water) to 2.98 g/cm^3 (gabbro). The use of a constant density introduces systematic errors in the reduced Helmert gravity anomalies, and consequently, in the geoid.

Martinec (1993) showed theoretically that the lateral density variation of the topographical masses may introduce errors on the geoid at the decimeter level. Fraser et al. (1998) developed a prototype GIS-based system to calculate terrain corrections

using the real topographical rock density values. They showed that in the Skeena Region of British Columbia, Canada, the terrain corrections to gravity can change by a few mGals when real topographical density is used. Subsequently, Pagiatakis et al. (1999) showed that the effect of lateral density variations on the geoid can reach nearly 10 *cm* in the Skeena Region BC and several millimeters in New Brunswick, where the terrain is moderate (hilly). However in their study they considered only the effect of terrain corrections to gravity. Concurrently to this research, Kuhn (2000a, 2000b) studied the density effect on the geoid based on several isostatic models. His results show that the anomalous density effect on the geoid can reach the decimeter level in South-west Germany without taking the downward continuation with the real gravity gradient into account.

In this work, the topographical mass density variation effects on the geoid are systematically investigated by following Helmert's 2nd condensation regularization. The Canadian Rocky Mountains have the largest relief and density variations in Canada. Thus, the determination of the geoid is affected by the topographical density effects the most in this area: the results shown here represent the largest effects on gravity and geoid in Canada.

6.2 Digital Topographical Density Model

A digital topographical density model (DTDM) is a representation of density distribution in the topography. Strictly speaking, a three-dimensional model would be needed to represent real topographical density distribution. It would require that a three-dimensional geological model of topography be available. At present, the available geological information in Canada and the US comes from two-dimensional geological maps and only lateral variation of density can thus now be modeled.

In 1997, the Geological Survey of Canada published the Digital Geological Map of Canada, which displays bedrock formations at or near the Earth surface (Wheeler

et al., 1997). The bedrock units are grouped according to composition and geological age. The digital version of the geological map digitized from the paper geological map of scale 1 : 5,000,000 facilitates its use greatly, by allowing a direct import into a GIS. About 16,000 geometrical polygons are used to delimit bedrock units over Canada. The area of individual polygons varies from 0.02 km^2 to about $800,000 \text{ km}^2$ depending on the geological complexity of the region. These polygons form the fundamental density units. The U.S. Geological Survey published a similar geological map in a digital version over the US in 1998.

Pagiatakis and Armenakis (1999) described the principles and the procedure of generating the two-dimensional topographical mass density map using the digital geological maps in a GIS. This procedure includes the following steps:

1. Compilation of topographical mass density tables in which each geological unit is assigned a range of densities or a unique density value according to existing geological studies.
2. Assignment of the mean value of the density range as a representative density value to each geological unit.
3. Overlay of the topographical mass density tables onto the digital geological map layer to generate the geological density map.

In this study, we used the density tables for Canada that were compiled by Fraser et al.(1998) and an approximate density table over the north-west part of the US that was compiled by R.O. Castle¹

In order to characterize the errors inherent in the DTDM, a standard deviation was associated with each representative density value. By assuming the uniform probability distribution of densities over the assigned density range $2q$ within each geological unit, the standard deviation $\sigma_{\bar{p}}$ was estimated by the following formula

¹1998, personal communication.

(Vaníček 1971 page 21):

$$\sigma_{\bar{p}} = q/\sqrt{3}. \quad (6.2)$$

A DTDM and the associated standard deviations were generated on a $30'' \times 30''$ geographical grid in the area of the Rocky Mountains by rasterizing the geological maps of the density distribution and its standard deviation. This area covers the North-west part of the US and the South-west part of Canada ($49^\circ - 62^\circ\text{N}$, $221^\circ - 261^\circ\text{E}$, see Figures 6.1 and 6.2).

6.3 Mathematical Formulation

The more realistic topographical mass density can now be expressed as the sum of the constant value $\rho_0 = 2.67\text{g}/\text{cm}^3$ and the lateral variation $\delta\bar{p}(\Omega)$:

$$\bar{p}(\Omega) = \rho_0 + \delta\bar{p}(\Omega), \quad (6.3)$$

where the over-bar indicates lateral variation of density. This equation means that the topographical mass density varies only with respect to horizontal locations. Martinec (1993) and Martinec and Vaníček (1994a, 1994b) derived formulae for the quantities of interest, namely the DDE, SIDE and PIDE defined as follows:

The *direct density effect* (DDE) - the part of DTE caused by lateral topographical mass density variation with respect to the constant density can be written as

$$\begin{aligned} \delta A_D(r_t, \Omega) = & G \int_{\Omega'_0} \delta\bar{p}(\Omega') \left[\frac{\partial \tilde{K}(r, \psi, r'_t)}{\partial r} - \frac{\partial \tilde{K}(r, \psi, R)}{\partial r} \right. \\ & \left. - R^2 \tau(H^0(\Omega')) \frac{\partial L^{-1}(r, \psi, R)}{\partial r} \right] \Big|_{r=r_t} d\Omega', \end{aligned} \quad (6.4)$$

where

$$\begin{aligned} \tilde{K}(r, \psi, r') = & \frac{1}{2}(r' + 3r \cos \psi)L(r, \psi, r') + \\ & + \frac{r^2}{2}(3 \cos^2 \psi - 1) \ln |r' - r \cos \psi + L(r, \psi, r')| + C, \end{aligned} \quad (6.5)$$

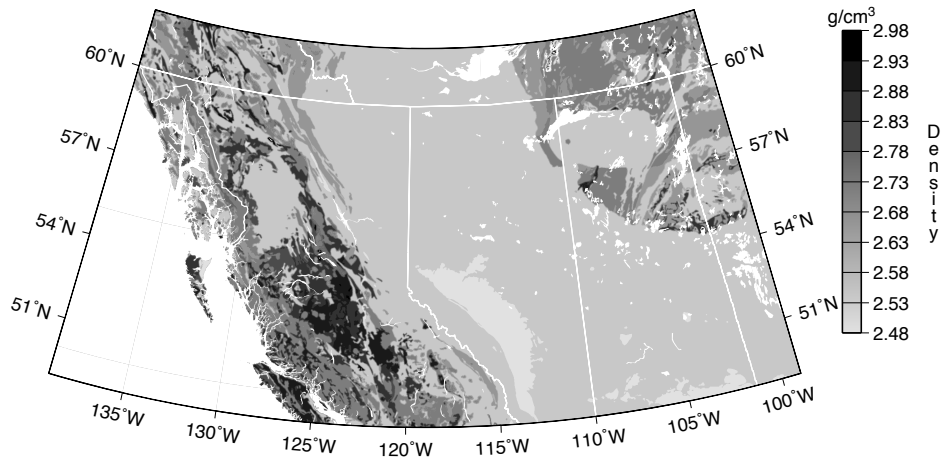


Figure 6.1: The lateral topographical mass density map in the Rocky Mountains. White areas indicate water bodies and geographical boundaries. Unit: g/cm^3 .

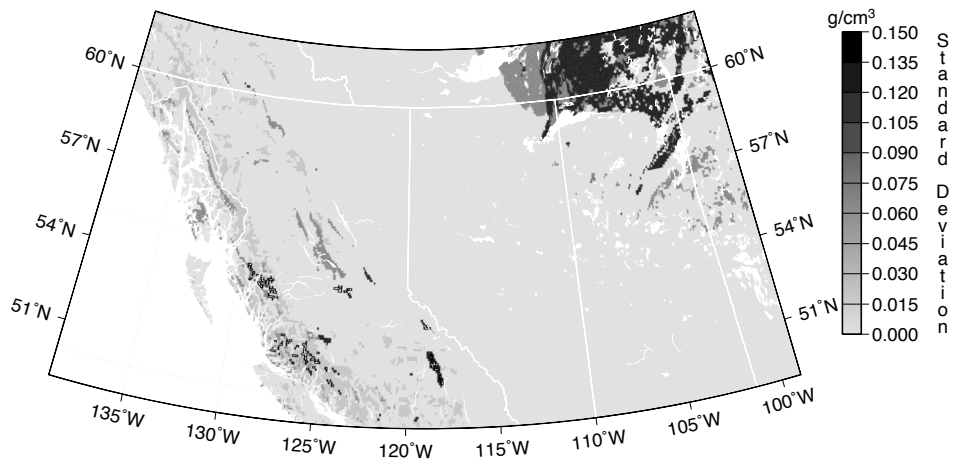


Figure 6.2: The standard deviation of the topographical mass density in the Rocky Mountains. White areas indicate water bodies and geographical boundaries. Unit: g/cm^3 .

$$\tau(H^0) \doteq H^0. \quad (6.6)$$

Here, $\tilde{K}(r, \psi, r')$ is the primitive function of the Newtonian kernel $L^{-1}(r, \psi, r')$ with respect to r' , i.e. $L^{-1}(r, \psi, r')$ is a partial derivative of $\tilde{K}(r, \psi, r')$, and τ is a coefficient function of the surface mass density for the Helmert layer.

The *secondary indirect density effect* (SIDE) - the part of SITE caused by lateral topographical mass density variation with respect to the mean density reads

$$\begin{aligned} \delta\gamma_D(r_t, \Omega) = & \frac{2G}{R} \int_{\Omega'_0} \delta\bar{\rho}(\Omega') \left[\tilde{K}(r_t, \psi, r'_t) - \tilde{K}(r_t, \psi, R) \right. \\ & \left. - R^2 \tau(H^0(\Omega')) L^{-1}(r_t, \psi, R) \right] d\Omega'. \end{aligned} \quad (6.7)$$

The *primary indirect density effect* (PIDE) - the part of PITE caused by lateral topographical mass density variation is ²

$$\begin{aligned} \delta N_D(\Omega) = & \frac{G}{\gamma} \int_{\Omega'_0} \delta\bar{\rho}(\Omega') \left[\tilde{K}(R, \psi, r'_t) - \tilde{K}(R, \psi, R) \right. \\ & \left. - R^2 \tau(H^0(\Omega')) L^{-1}(R, \psi, R) \right] d\Omega'. \end{aligned} \quad (6.8)$$

Integrals (6.4), (6.7) and (6.8) become singular when the computation point coincides with the integration point, but the singularity is weak and removable (see Martinec 1993).

The errors of the derived DDE, SIDE and PIDE can be estimated from the errors of topographical height and density data. Only the topographical density errors will be considered here. The errors in the topographical heights may significantly affect the DDE, PIDE and SIDE results. Their effect needs to be studied in the future. To facilitate the derivation, let us write eqns. (6.4), (6.7) and (6.8) in their generic form:

$$\delta d(r_t, \Omega) = c \int_{\Omega'} \delta\bar{\rho}(\Omega') D(r_t, \psi, r'_t) d\Omega', \quad (6.9)$$

where $D(r_t, \psi, r'_t)$ stands for the appropriate integration kernel. Then, the individual

²This equation is different from eqn. (6.10) by Martinec (1998) whose equation requires the integration to be carried out globally to derive an accurate estimate of δN_D because the far-zone contribution can reach the same magnitude as the near-zone contribution in his eqn. (6.10).

error of any of these effects is given by

$$\epsilon_\delta(r_t, \Omega) = c \int_{\Omega'} \epsilon_d(\Omega') D(r_t, \psi, r'_t) d\Omega', \quad (6.10)$$

where $\epsilon_d(\Omega')$ stands for the error in the topographical density of the integration point.

The variance σ_δ^2 of ϵ_δ can be expressed as (Heiskanen and Moritz; 1967, eqn. 7-74)

$$\sigma_\delta^2(r_t, \Omega) = c^2 \int_{\Omega'} \int_{\Omega''} \sigma_{\bar{\rho}}(\Omega', \Omega'') D(r_t, \psi', r'_t) D(r_t, \psi'', r''_t) d\Omega'' d\Omega', \quad (6.11)$$

where $\sigma_{\bar{\rho}}(\Omega', \Omega'')$ is the covariance of the topographical density $\bar{\rho}(\Omega)$ between two integration points located at Ω' and Ω'' , and $\sigma_{\bar{\rho}}(\Omega, \Omega) = \sigma_{\bar{\rho}}^2(\Omega)$.

The discrete form of eqn. (6.11) can be written as

$$\sigma_\delta^2(r_t, \Omega_i) = c^2 \sum_j \sum_k \int_{\Delta S'_j} \int_{\Delta S''_k} \sigma_{\bar{\rho}}(\Omega'_j, \Omega''_k) D(r_t, \psi'_{ij}, r'_t) D(r_t, \psi''_{ik}, r''_t) d\Omega'' d\Omega', \quad (6.12)$$

where $\Delta S'_j$ and $\Delta S''_k$ represent the discrete surface elements around points Ω' and Ω'' , respectively. If the errors between two different discrete cells are assumed to be independent, eqn. (6.12) becomes

$$\sigma_\delta^2(r_t, \Omega_i) = c^2 \sum_j \sigma_{\bar{\rho}}^2(\Omega'_j) \left(\int_{\Delta S'_j} D(r_t, \psi'_{ij}, r'_t) d\Omega' \right)^2. \quad (6.13)$$

Thus under the assumption that the errors between two different cells are uncorrelated, the variances of DDE, SITE and PIDE for discrete integral can be evaluated using the following discretized equations:

$$\begin{aligned} \sigma_{\delta A}^2(r_t, \Omega_i) = & G^2 \sum_j \sigma_{\bar{\rho}}^2(\Omega'_j) \left(\left[\frac{\partial \tilde{K}(r, \psi_{ij}, r'_t)}{\partial r} - \frac{\partial \tilde{K}(r, \psi_{ij}, R)}{\partial r} \right. \right. \\ & \left. \left. - R^2 \tau(H^0(\Omega'_j)) \frac{\partial L^{-1}(r, \psi_{ij}, R)}{\partial r} \right] \Big|_{r=r_t} \Delta S'_j \right)^2, \end{aligned} \quad (6.14)$$

$$\begin{aligned} \sigma_{\delta \gamma}^2(r_t, \Omega_i) = & \left(\frac{2G}{R} \right)^2 \sum_j \sigma_{\bar{\rho}}^2(\Omega'_j) \left([\tilde{K}(r_t, \psi_{ij}, r'_t) - \tilde{K}(r_t, \psi_{ij}, R) \right. \\ & \left. - R^2 \tau(H^0(\Omega'_j)) L^{-1}(r_t, \psi_{ij}, R)] \Delta S'_j \right)^2, \end{aligned} \quad (6.15)$$

$$\begin{aligned} \sigma_{\delta N}^2(\Omega_i) = & \left(\frac{G}{\gamma} \right)^2 \sum_j \sigma_{\bar{\rho}}^2(\Omega'_j) \left([\tilde{K}(R, \psi_{ij}, r'_t) - \tilde{K}(R, \psi_{ij}, R) \right. \\ & \left. - R^2 \tau(H^0(\Omega'_j)) L^{-1}(R, \psi_{ij}, R)] \Delta S'_j \right)^2. \end{aligned} \quad (6.16)$$

6.4 Numerical Results

As in the case of the DTE and SITE, the DDE and SIDE should be added to the Helmert anomalies at the Earth surface. If the mean Helmert anomalies are used, then mean values of the DDE and SIDE have to be evaluated; they should be computed for the cells of the same size as the mean Helmert anomalies represent. For Canada, the mean Helmert gravity anomalies for $5' \times 5'$ cells are being used to determine the geoid. Thus the mean values of $5' \times 5'$ DDE and SIDE must be evaluated and added to the gravity anomalies.

The PIDE is the correction to the geoid height that is evaluated as the point value, thus the point value of PIDE must be evaluated. In our computation, the $30'' \times 60''$ DTDM and DEM are used as input data for the evaluation of the point PIDE in the spacing of $5' \times 5'$.

As described in Section 6.2, the representative density value for each geological unit is taken as the mean value of the density range. The standard deviations of the DDE and PIDE are evaluated in this study, while the SIDE contribution is too small to be taken into account. Its amplitude is about 2.5% of the SITE evaluated on the geoid.

Numerical tests show that the density effects on the geoid heights evaluated from integration over 1° , 2° and 3° caps differ by less than 1 *mm* in absolute value even for an extreme density variation of 0.3 g/cm^3 . Therefore, a spherical cap with the radius of 1° was used to evaluate the DDE and PIDE. The far-zone contribution of the lateral density variation effects is not estimated due to lack of a global coverage of density data. Since the mean global value of $\delta\rho(\Omega)$ is 0, the far-zone contribution is likely to be very small. Further studies are needed to evaluate the impact of the far-zone.

6.4.1 Mean Direct Density Effect

When a mean value of the DDE is evaluated in a cell, a certain number of point values must be used to compute the average. For example, a mean $5' \times 5'$ cell value can be evaluated by using 5, 10, 50 or more point values within the cell. The question is: how many point values are required to give a sufficiently accurate mean value? Since the final product is the geoid, it is appropriate to set the criterion in terms of geoid height accuracy. Figure 6.3 shows that for height data on a $30'' \times 60''$ grid, 50 points regularly spaced within the $5' \times 5'$ cell, will generate an accurate enough approximation to the mean DDE of the cell. The maximum difference between the geoid heights evaluated from the mean DDE values of 50 and 100 point values is 0.6 cm . The test profile ($49^\circ N$), which passes through the roughest part of the Canadian Rocky Mountains, suggests that when the point values are evaluated at a step equal to, or smaller than the input height step, the geoid height cannot be improved significantly. In Figure 6.3, the numerical labels stand for the number of point values used to evaluate the mean value.

The mean $5' \times 5'$ DDE values are summarized in Table 6.1. The DDE range is about 5% of the DTE range, which is $[-54.3, 79.5] \text{ mGal}$ (Vaníček et al., 1995). The DDE standard deviations were estimated only as point values based on eqn. (6.14) because of the sheer volume of computation for the mean standard deviations. These point values are theoretically greater than the standard deviations of the mean values. In terms of the given standard deviations, the DDE estimates appear precise enough (see Figures 6.4 and 6.5). On the other hand, these point values may overestimate the accuracy of the point DDE because the topographical mass densities within the same geological unit are correlated positively.

After performing the downward continuation to the geoid using the DOWN'97 software (Vaníček et al., 1997), the mean DDE on the geoid is between -12.7 mGal and 9.8 mGal with the mean of -0.007 mGal (see Figure 6.6). More than 99% of DDE values are within the range of $[-4, 4] \text{ mGal}$. After conversion to geoid heights

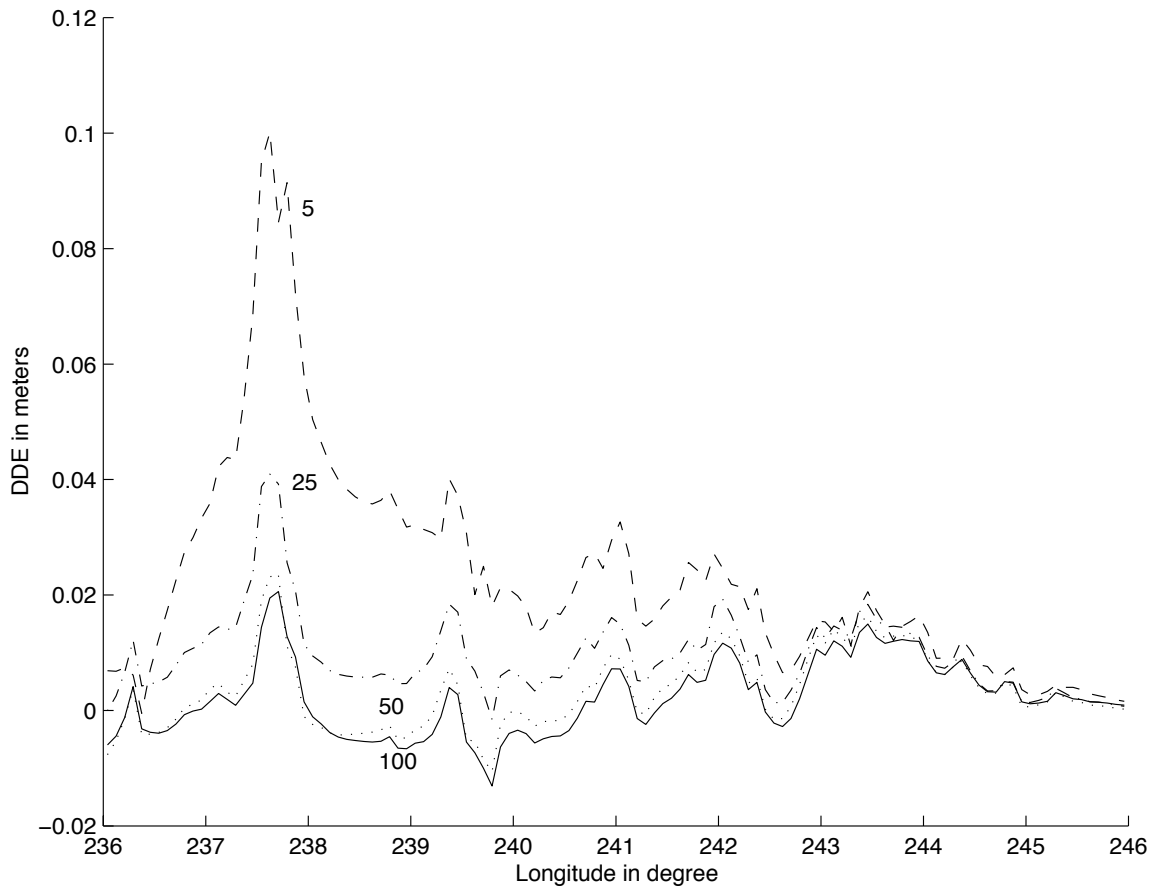


Figure 6.3: Geoid correction profiles due to the mean DDE computed from different number of point values.

Table 6.1: Direct topographical lateral density variation effects on gravity at the Earth surface in mGal.

TERM	MIN	MAX	Mean	r.m.s.
DDE	-4.5	2.3	0.0	0.3
StD	0.0	2.4		0.1

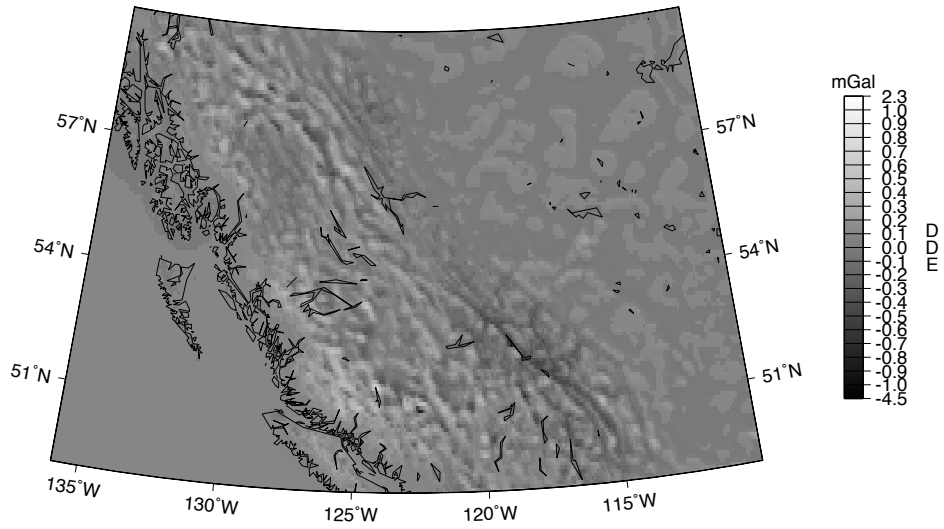


Figure 6.4: The mean DDE $\overline{\delta A_D}$ on gravity at the Earth surface in the Canadian Rocky Mountains in mGal. The solid lines delimit water bodies.

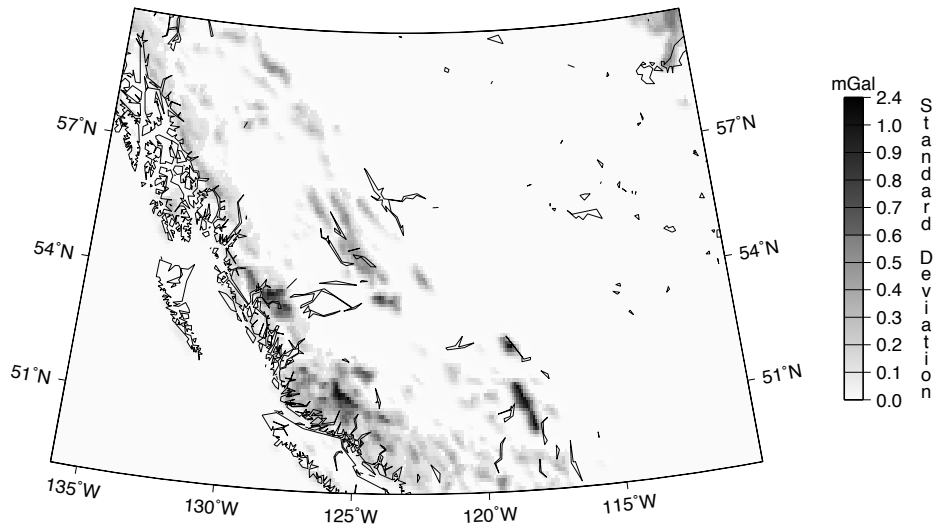


Figure 6.5: The point standard deviation of the DDE $\sigma_{\delta A}$ in the Canadian Rocky Mountains in mGal. The solid lines delimit water bodies.

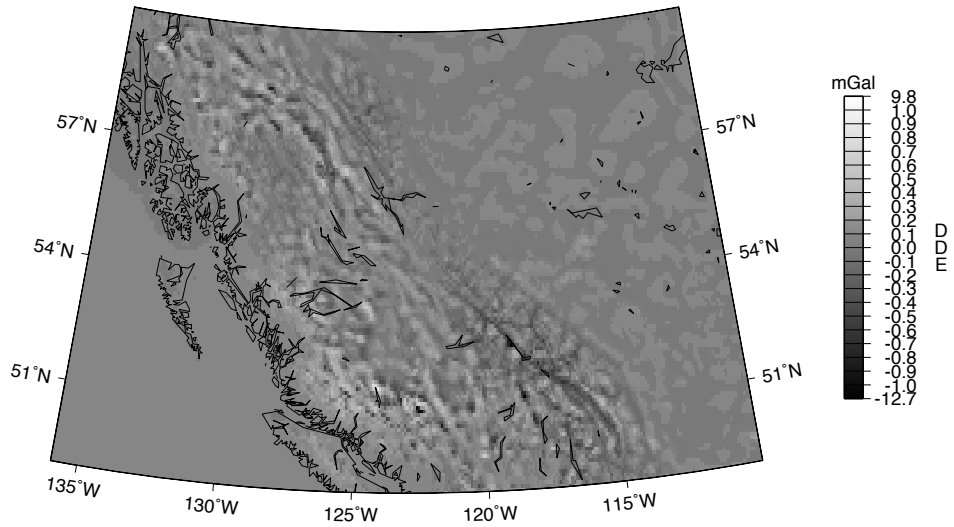


Figure 6.6: The mean DDE $\overline{\delta A_D}$ on the geoid in the Canadian Rocky Mountains in mGal. The solid lines delimit water bodies.

through Stokes's integration, the effect on the geoid reaches a few centimeters with short wavelengths being dominant (see Table 6.2 and Figure 6.7). The DDE displays a high correlation with the topographical density as shown in Figure 6.1.

Table 6.2: Direct and primary indirect lateral topographical density variation effects on geoid heights, in cm.

TERM	MIN	MAX	Mean	r.m.s.
DDE	-5.1	2.6	-1.0	1.3
PIDE	-2.5	1.7	0.2	0.5
StD	0.0	0.5		0.0
Total Effect	-7.0	2.8	-0.7	1.1

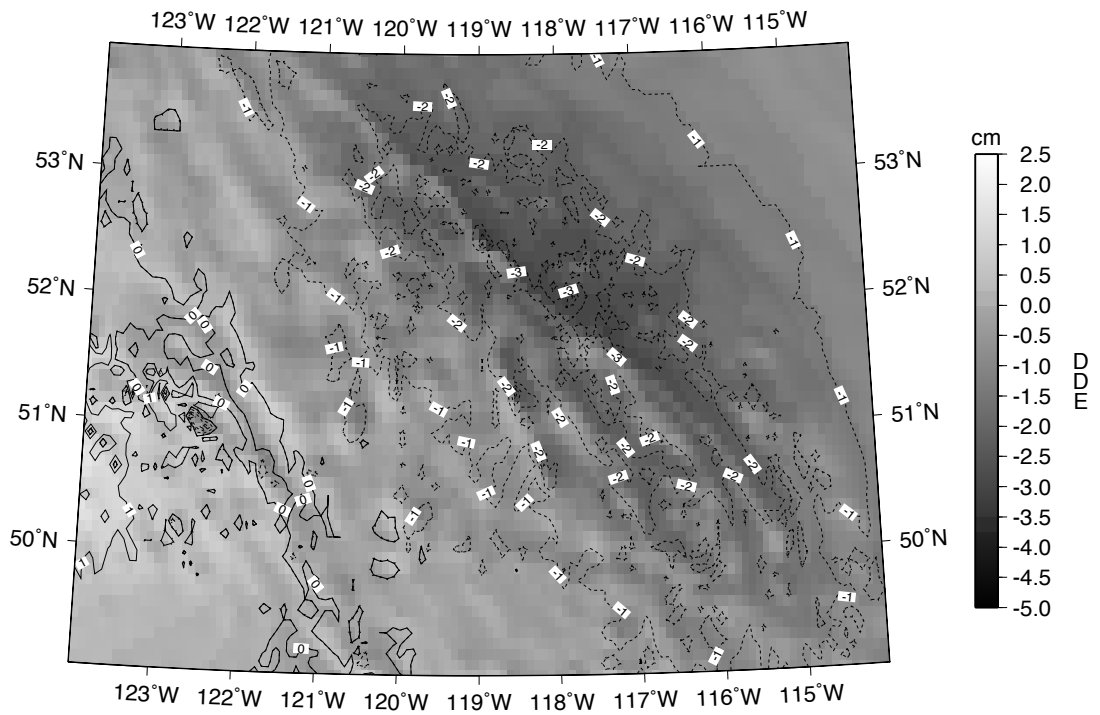


Figure 6.7: The mean DDE on the geoid in the Canadian Rocky Mountains. Contour interval: 1 cm.

6.4.2 Primary Indirect Density Effect

Similar to the DDE, the PIDE affects the geoid at the centimeter level. The PIDE estimates are statistically precise as we can see from the comparison with their standard deviations (Figures 6.8 and 6.9). The range roughly corresponds to 5% of the PITE range (Vaníček et al., 1995). While the PITE is always negative, the sign of the PIDE changes between positive and negative due to the nature of the density variation. The PIDE is mainly characterized by intermediate wavelength features which correlate highly with topographical density.

6.4.3 Total Lateral Topographical Density Variation Effect on the Geoid

The sum of both effects (DDE and PIDE) on geoid heights was evaluated, and is presented in Figure 6.10. No significant cancellation between the PIDE and the DDE can be detected in these results. Both short wavelength components from the DDE and intermediate wavelength components from the PIDE have reinforced each other. More than 99% of the values are between -3 and 3 cm (see Table 6.4). Only eight values are larger (in absolute value) than 5 cm.

Table 6.3: Topographic mass density variation effects versus the total topographical effects using the actual mean density value. (Note: DTE, SITE and PITE by Vaníček et al. are computed by using the constant density 2.67 g/cm³.)

TERM	MIN	MAX	RANGE
DTE(Vaníček et al., 1995)	-54.3 mGal	79.5 mGal	133.8 mGal
DDE	-4.5 mGal	2.3 mGal	6.8 mGal
SITE(Vaníček et al., 1995)	0 μ Gal	470 μ Gal	470 μ Gal
SIDE	-8 μ Gal	5 μ Gal	13 μ Gal
PITE(Vaníček et al., 1995)	-105 cm	1 cm	106 cm
PIDE	-2.5 cm	1.7 cm	4.2 cm

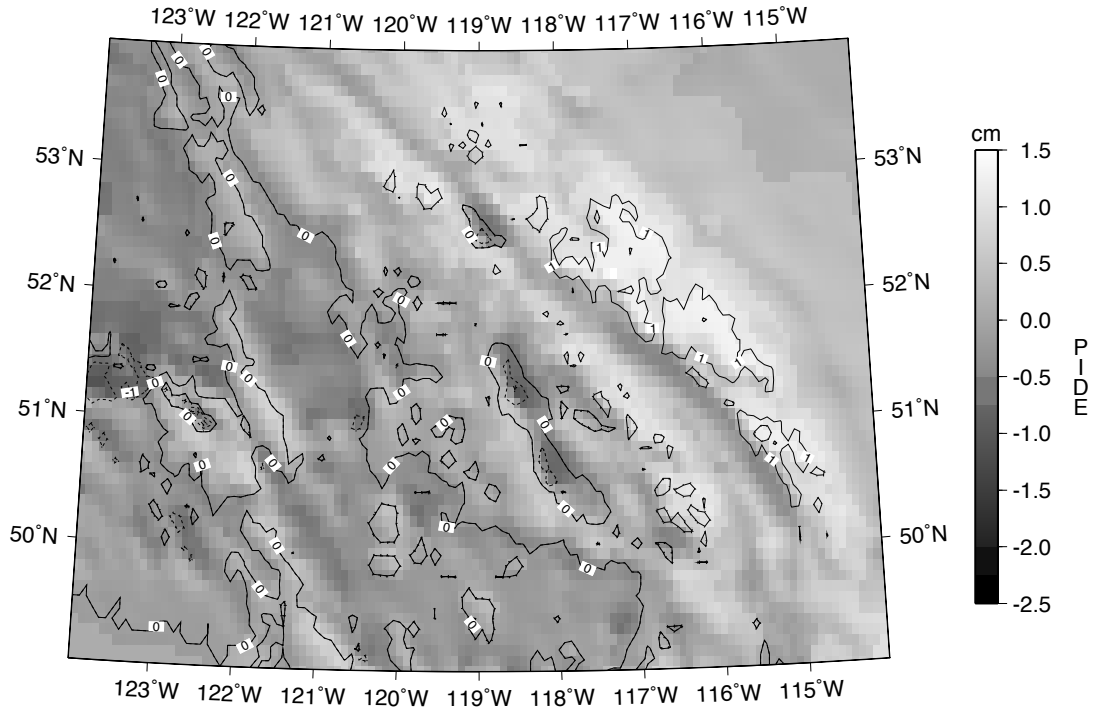


Figure 6.8: The PIDE δN_D on the geoid in the Canadian Rocky Mountains. Contour interval: 1 cm.

Table 6.4: Distribution of the total effect values caused by the lateral topographical mass density variation.

Range (cm)	Count	%	Range (cm)	Count	%
-7 to -6	4	0.06	-2 to -1	1800	25.04
-6 to -5	4	0.06	-1 to 0	3779	52.57
-5 to -4	8	0.11	0 to 1	890	12.38
-4 to -3	51	0.71	1 to 2	159	2.21
-3 to -2	479	6.66	2 to 3	15	0.21

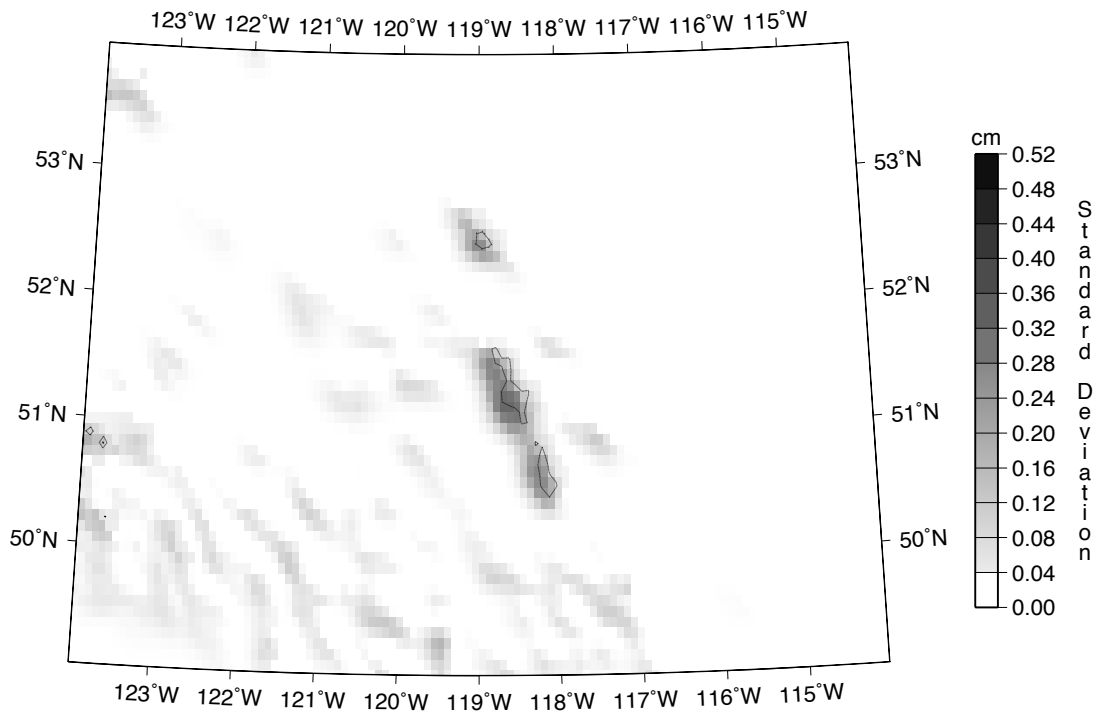


Figure 6.9: The standard deviation of the PIDE $\sigma_{\delta N}$ in the Canadian Rocky Mountains (cm).

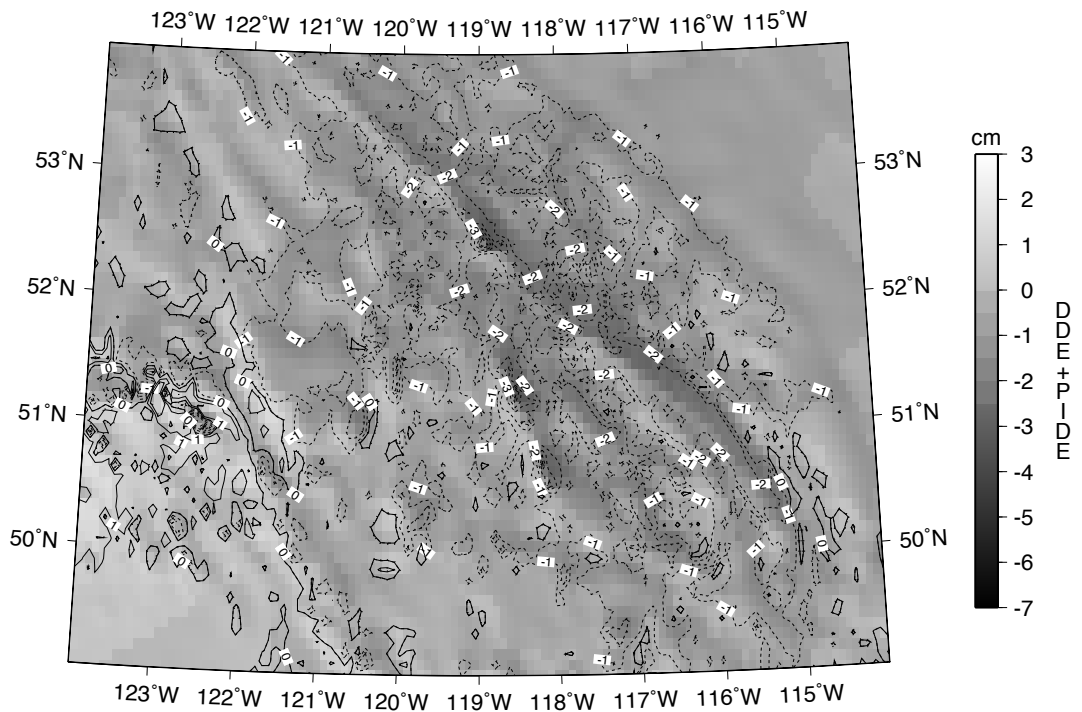


Figure 6.10: The sum of the DDE and PIDE on the geoid in the Canadian Rocky Mountains. Contour interval: 1 cm.

6.5 Summary

Formulae for estimating the standard deviation of the DDE, SIDE and PIDE have been derived. A procedure for the evaluation of the density effects is proposed.

This investigation shows that the DDE and PIDE can reach about 5% of the DTE and PITE, respectively. The SIDE is too small to be taken into account. Comparing the DDE and PIDE with their standard deviations, their estimates appear to be statistically precise enough. The total density variation effect on geoid heights ranges from -7.0 cm to 2.8 cm in the Canadian Rocky Mountains. It is evident that the introduction of a digital topographical density model will significantly improve the accuracy of the geoid. The results presented in this research may have underestimated the effects because the mean DEM of $30'' \times 60''$ is not sufficient to model the topography in the Canadian Rocky Mountains. Furthermore, a better density model will be needed to estimate the density effects at the one-centimeter level of accuracy.

Chapter 7

Conclusions and Recommendations

The downward continuation of the Earth's gravity is an essential step in the gravity reduction for solving the geodetic boundary value problem (GBVP) to determine a gravimetric geoid. This step reduces gravity from the Earth's surface, or a flight level, to the geoid by taking the real gradient of the gravity into account. It can be carried out either by the discrete Poisson downward continuation (DDC), or by the analytical downward continuation (ADC). Nevertheless it is controversial whether or not this step leads to a better solution for the geoid because the downward continuation of the Earth's gravity is classified as an ill-posed problem. The main objective of this research was to develop computational methods for the discrete Poisson downward continuation to support the determination of a precise geoid.

In the determination of the geoid based on Helmert's 2nd condensation, the topographical mass must be completely removed and condensed on the geoid by evaluating the direct topographical effect (DTE) on gravity, the secondary indirect topographical effect (SITE) on gravity, and the primary indirect effect (PITE) on the geoid. The DTE, SITE and PITE are being routinely evaluated by taking the constant density $2.67g/cm^3$ instead of the real topographical mass density. Another objective of this research was to investigate the effect of the topographical mass density variation with respect to the constant density $2.67g/cm^3$ on the geoid.

7.1 Solvability of the Discrete Poisson Downward Continuation

A spherical harmonic form of the solution to the continuous inverse Poisson problem was derived. It was pointed out that the corresponding discrete solution exists, but may not be unique and stable. For a small error in input, we unavoidably get a large error in output. The high-resolution solution may be completely wrong if high-frequency errors exist in the data. It is in this sense that the inverse Poisson problem is defined to be an ill-posed problem.

7.2 Discretization of Poisson's integral

Since we only collect gravity data at discrete points, either on the Earth's surface or in the air, Poisson's integral has to be approximated by a discrete form that best uses available data and efficiently eliminates errors and biases. The discretization of Poisson's integral consists of the following problems: evaluation of the far zone contribution; modification of the Poisson kernel; combination of terrestrial data with a global geopotential model; truncation of Poisson's integral and discretization of the Poisson integral in the near zone.

The far zone contribution was formulated using the Molodenskii-type harmonic expansion technique based on the standard, spheroidal and modified spheroidal Poisson kernels in conjunction with the combined technique in which terrestrial data and satellite data are jointly used.

The efficiency of the modified spheroidal Poisson kernel in reducing the real far zone contribution over using the unmodified spheroidal Poisson kernel was studied. The numerical results suggest that the modified spheroidal Poisson kernel significantly reduce the real far zone contribution but it cannot perform better than the standard Poisson kernel.

The determination of the critical radius of the near zone cap was studied. It was found that Heiskanen and Moritz's condition gives a radius that is too small for the determination of the 1-cm geoid, while Martinec's condition gives a radius unnecessarily large. The critical radius must be chosen according to accuracy of the adopted global geopotential model.

An efficient algorithm for the evaluation of the far zone contribution was developed. The new algorithm is one order of magnitude faster than the standard algorithm with an accuracy of 0.001 mGal.

The three discrete models (point-point, point-mean and mean-mean) of Poisson's integral were formulated. The analysis of the three models suggested that the mean-mean model tend to produce the roughest solution, while the point-point model tend to give the smoothest solution among the three models. Furthermore, the topographical height rather than the relative relief determines the condition of the coefficient matrix for a discrete model. The numerical tests in three different regions in Canada showed that the $5' \times 5'$ downward continuation was a very stable problem regardless of the discrete model used.

7.3 Solution of the Discrete Inverse Poisson Problem

The inverse Poisson problem can be reduced to a linear system of algebraic equations for each discrete model. The coefficient matrix of the system is large and sparse. The iterative method is the most efficient method to solve the system. The combined iterative method was suggested to speed up convergence and eliminate round-off errors. In the case of a singular coefficient matrix, the iterative approach may fail to give a useful solution. The truncated singular value decomposition (TSVD) was introduced

to provide a stable solution from noisy data. The TSVD is superior to other regularization methods since it makes the process of solving the system physically and mathematically meaningful.

The synthetic approach was used to evaluate the three discrete models. GPM98a was adopted to generate synthetic data. The tests showed that the mean-mean model produces a sufficiently accurate solution when the averaging error is corrected for. Synthetic tests also showed that 0.5° may be chosen as the radius of the near zone cap when the maximum elevation does not exceed 2 km, and EGM96 is adopted.

A block-wise technique was developed to avoid solving a large system of equations and improve the computational speed of the discrete Poisson downward continuation. The coefficient interpolation method was implemented to reduce the CPU time of evaluating the doubly averaged Poisson kernel. A software package, DOWN97, was developed to compute the discrete Poisson downward continuation.

7.4 Analytical Downward Continuation

The analytical downward continuation (ADC) is a method based on the Taylor series expansion of the gravity anomaly. It was introduced as an improved method for solving the Molodenskii boundary value problem. One open question may arise as to whether it gives a solution as good as the one by the discrete Poisson downward continuation (DDC).

The synthetic tests with EGM96 and GPM98a suggested that the ADC causes an error about 10 percent of the downward continuation effect, while the error of the DDC is smaller than 1 cm. The test result using the residual Helmert anomaly in the Rocky Mountains show that the maximum difference between the two methods can reach 10 mGal in gravity, and about 10 cm in geoid height. The DDC geoid height results are 5 cm larger on average than the ADC one. The mean difference also accounts for about 10 percent of the mean downward continuation effect.

It was implied that an ultra-high degree synthetic global geopotential model constrained to the Kaula-type degree variance models is too smooth to simulate the Helmert gravity anomaly, especially in mountainous areas. Therefore, the accuracy assessment of a geoid calculation method, based on this type of synthetic geopotential model, will not necessarily reflect the accuracy of a realistic geoid model computed by the method even though errorless data are used.

7.5 Topographical Density Variation Effects on Gravity and Geoid

In the Stokes-Helmert approach, the Helmert gravity anomaly is derived through removal and condensation of the topographical mass. The use of a constant density ($2.67g/cm^3$) introduces errors in the reduced Helmert gravity anomalies, and consequently, in the geoid.

Formulae for estimating the standard deviations of the DDE, SIDE and PIDE were derived. This investigation showed that the DDE and PIDE can reach about five percent of the DTE and PITE, respectively. The SIDE is too small to be taken into account. Comparing the DDE and PIDE to their standard deviations, their estimates appear to be statistically precise. The total density variation effect on the geoid heights ranges from -7.0 cm to 2.8 cm in the Canadian Rocky Mountains. It is evident that the introduction of the digital topographical density model will significantly improve the accuracy of the geoid. The results presented in this dissertation may have underestimated the density effects because the mean DEM of $30'' \times 60''$ was not sufficient to model the topography in the Canadian Rocky Mountains.

7.6 Recommendations

This research establishes a few important research directions regarding the downward continuation of the Earth's gravity and the topographical density effect on the geoid:

1. The present study discussed the Molodenskii-type modified Poisson kernel only. Further developments with regard to the modification method in association with accuracy of the global geopotential model to derive the far zone contribution more accurately are necessary.
2. In Canada, the $5' \times 5'$ downward continuation was proved to be a stable problem. To derive a higher resolution geoid model, the numerical stability and reliability of higher resolution downward continuation must be studied.
3. To facilitate the calculations, the gravity data to be downward continued were assumed to be known at regular grid points, while the actual gravity data were collected at unevenly spaced points. The error caused by interpolation was ignored. The downward continuation method based on the arbitrary distribution of the data should be developed to eliminate the interpolation error.
4. A comprehensive synthetic global geopotential model should be developed in simulating the regularized gravity field, such as the Helmert gravity anomaly, to evaluate accuracy of the discrete models.
5. A computational method of the analytical downward continuation accounting for the far zone contribution should be developed to improve its accuracy.
6. The topographical density effect was evaluated in this research based on Helmert's 2nd condensation. Other isostatic compensation models, such as the Airy-Heiskanen model, Pratt-Hayford model and the Moho model, should be studied to find the best method to account for the topographical density effect.

References

- Aronoff S. (1989). *Geographic information systems*, A management perspective. WDL Publications.
- Bjerhammar, A. (1966). On the determination of the shape of the geoid and the shape of the Earth from an ellipsoidal surface of reference. *Bull. Géod* , 81, 235-265.
- Bjerhammar, A. (1975). Discrete solutions of the boundary value problem in physical geodesy. *Tellus*, 2, 2, 97-105.
- Bjerhammar, A. (1976). A Dirac approach to physical geodesy. *Zeitschrift für Vermessungswesen*, 101, 41-44.
- Bjerhammar, A. (1987). Discrete physical geodesy. OSU Rep. 380, Dept. of Geodetic Science and Surveying, The Ohio State Univ., Columbus.
- Bomford, G. (1971). *Geodesy*. 3th ed., Oxford, at the Clarendon Press.
- Castle R (1998). Personal communication.
- Engels, J., E. Grafarend, W. Keller, Z. Martinec, F. Sansò and P. Vaníček (1993). The geoid as an inverse problem to be regularized. In: *Inverse Problems: Principles and applications in Geophysics, Technology and Medicine*. Eds. G. Anger, R. Gorenflo, H. Jochmann, H. Moritz and W. Webers, AkademieVerlag, Berlin, 122-167.

- Faddeev, D. K. and V. N. Faddeev (1963). *Computational Methods of Linear Algebra*, WH Freeman and Company.
- Featherstone, W. E., J. D. Evans and J. G. Olliver (1998). A Meissl-modified Vaníček and Kleusberg kernel to reduce the truncation error in gravimetric geoid computations. *Journal of Geodesy*, 72, 154-160.
- Featherstone, W. E. and J. F. Kirby (2000). The reduction of aliasing in gravity anomalies and geoid heights using digital terrain data. *Geophys. J. Int.*, 141, 204-212.
- Fei, Z. L. and M. G. Sideris, (2000). A new method for computing the ellipsoidal correction for Stokes's formula. *Journal of Geodesy*, 74, 223-231.
- Forsberg, R. and M. G. Sideris (1993). Geoid Computation by the Multi-band Spherical FFT Approach. *Manuscripta Geodaetica*, 18, 82-90.
- Forsberg, R. (1987). A new covariance model for inertial gravimetry and gradiometry. *JGR*, 92(B2), 1305-1320.
- Forsberg, R. and S. Kenyon (1994). Evaluation and downward continuation of airborne gravity data - the Greenland example. Proc. Int. Symp. Kinematic Systems in Geodesy, Geomatics and Navigation (KIS 94), 531-538.
- Fraser D, Pagiatakis S. D. and Goodacre A. K. (1998). In-situ rock density and terrain corrections to gravity observations, Proc. Of 12th Annual Symposium on Geographic Information Systems, Toronto 6 to 9 April, 1998, 357-360.
- Geological Survey of Canada (1997). Geological Map of Canada (CD-ROM). Natural Resources Canada.
- Gerald, C. F., P. O. Wheatley (1994). *Applied Numerical Analysis*, Addison-Wesley Publishing Company.

- Golub, G. H. and F. C. Van Loan 1989. *Matrix Computations*, 2nd edn Baltimore, MD: Johns Hopkins Univ. Press.
- Groetsch, C. W. (1984). *The Theory of Tikhonov Regularization for Fredholm Equations of the First Kind*, Bost, MA: Pitman.
- Haagmans, R., E. de Min, M. van Gelderen (1993). Fast evaluation of convolution integral on the sphere using 1D-FFT and a comparison with existing methods for Stokes integral. *Manuscripta Geodaetica*, 18, 227-241.
- Haagmans, R. (2000). A synthetic Earth for use in Geodesy. *Journal of Geodesy*, 74: 503-511.
- Hadamard, J. S. (1952). *Lectures on Cauchy's Problem in Linear Partial Differential Equations*, New York, Dover.
- Hansen, P. C. (1987). The truncated SVD as a method for regularization. *BIT* 27, 534-553.
- Hansen, P. C. (1990). Truncated singular value decomposition solutions to discrete ill-posed problems with ill-determined numerical rank. *SIAM J. SCI. STAT. COMPUT.* 11(3), 503-518.
- Hansen, P. C. (1990). The discrete Picard condition for discrete ill-posed problems. *BIT* 30, 658-672.
- Hansen, P. C. (1992). Numerical tools for analysis and solution of Fredholm integral equations of the first kind. *Inverse Problem*, 8, 849-872.
- Heiskanen, W. A. and H. Moritz (1967). *Physical Geodesy*, WH Freeman, San Francisco.
- Huang, J., P. Vaníček, P. Novák (2000). An alternative algorithm to FFT for the numerical evaluation of Stokes's integral. *Stud. Geoph. et Geod.*, 44, 374-380.

- Huang, J., P. Vaníček, S. Pagiatakis and W. Brink (2001). Effect of topographical mass density variation on gravity and geoid in the Canadian Rocky Mountains. *Journal of Geodesy*, 74, 805-815.
- Huang, J., M. Véronneau and S. D. Pagiatakis (2000). On the ellipsoidal correction to the spherical Stokes in the determination of geoid. CGU2000, May 23-27, 2000, Banff, Alberta, Canada.
- Huang, J., S. D. Pagiatakis and M. Véronneau (2000). Truncation of Poisson's integral in upward and downward continuations of the Earth's gravity. GGG2000, July 31-August 4, 2000, Banff, Alberta, Canada. In Proc IAG Symp, Banff, Sideris (ed.), Gravity, Geoid and Geodynamics 2000, Vol. 123, 323-328, Springer-Verlag, 2001.
- Holms, S. and W. Featherstone (1999). Using a synthetic Earth gravity model to assess performance of modified kernels in gravimetric geoid computation. (personal communication).
- Hotine, M. (1969). *Mathematical Geodesy*, U. S. Department of Commerce.
- Jekeli, C. (1978). An investigation of two models for the degree variances of global covariance functions. OSU Rep. 275, Dept. of Geodetic Science and Surveying, The Ohio State Univ., Columbus.
- Jekeli, C. (1981). The downward continuation to the Earth's surface of truncated spherical and ellipsoidal harmonic series of the gravity and height anomalies. OSU Rep. 323, Dept. of Geodetic Science and Surveying, The Ohio State Univ., Columbus.
- Jekeli, C. (1981). Modifying Stokes's function to reduce the error of geoid undulation computations. *JGR*, 86(B2), 6985-6990.

- Jekeli, C. and R. Garcia (2000). Local geoid determination with in Situ geopotential data obtained from satellite-to-satellite tracking. GGG2000, July 31-August 4,2000, Banff, Alberta, Canada.
- Kaula, W. M. (1966). Tests and combination of satellite determinations of the gravity field with gravimetry. *JGR*, 71, 5303-5314.
- Kellogg, O. D. (1929). Foundations of potential theory. Berlin, J. springer (New York, Dover Publications, 1953).
- Koch, K. R. (1968). Solution of the geodetic boundary value problem in case of a reference ellipsoid. OSU Rep. 104, Dept. of Geodetic Science and Surveying, The Ohio State Univ., Columbus.
- Kuhn M. (2000). GeoidBestimmung unter verwendung verschiedener dichteypothesen. Deutsche Geodätische Kommission, Reihe C, Dissertationen, Heft Nr. 520, München 2000.
- Kuhn M. (2000). Density modelling for geoid determination. GGG2000, July 31-August 4,2000, Banff, Alberta, Canada.
- Lemoine F. G., S. C. Kenyon, J. K. Factor, R. G. Trimmer, N. K. Pavlis, D. S. Chinn, C. M. Cox, S. M. Klosko, S. B. Luthcke, M. H. Torrence, Y. M. Wang, R. G. Williamson, E. C. Pavlis, R. H. Rapp, and T. R. Olson. (1998). The development of the joint NASA GSFC and the National Imagery and Mapping Agency geopotential model EGM96. NASA/TP-1998-206861.
- MacMillan, W. D. (1930). Theoretical mechanics, vol.2: The theory of the potential. New York, McGraw-Hill (New York, Dover Publications, 1958).
- Mainville, A., M. Véronneau, R. Forsberg and M. Sideris (1995). A comparison of geoid and quasigeoid modeling methods in rough topography. In *Gravity*

- and Geoid*, pp. 491-501, eds. H. Sünkel and I. Marson, IAU Symposium 113, Springer Verlag, New York.
- Martinec, Z. (1993). Effect of lateral density variations of topographical masses in view of improving geoid model accuracy over Canada. Contract report for Geodetic Survey of Canada, Ottawa, June 1993.
- Martinec, Z., C. Matyska, E. W. Grafarend and P. Vaníček (1993). On Helmert's 2nd condensation technique. *Manuscripta Geodaetica*, 18, 417-421.
- Martinec, Z. and P. Vaníček (1994a). The indirect effect of topography in the Stokes-Helmert's technique for a spherical approximation of the Geoid. *Manuscripta Geodaetica*, 19, 213-219.
- Martinec, Z. and P. Vaníček (1994b). Direct topographical effect of Helmert's condensation for a spherical approximation of the geoid. *Manuscripta Geodaetica*, 19, 257-268.
- Martinec, Z. (1996). Stability investigations of a discrete downward continuation problem for geoid determination in the Canadian Rocky Mountains. *Journal of Geodesy*, 70, 805-828.
- Martinec, Z. and P. Vaníček (1996). Formulation of the boundary-value problem for geoid determination with a higher-order reference field. *Geophys. J. Int.*, 126, 219-228.
- Martinec, Z. and E. W. Grafarend (1997). Solution to the Stokes boundary value problem on an ellipsoid of revolution. *Stud. Geoph. et Geod.*, 41, 103-129.
- Martinec, Z. (1998). *Boundary-Problems for Gravimetric Determination of a Precise Geoid*, Lecture Notes in Earth Sciences 73, Springer.

- Meissl, P. (1971). Preparation for the numerical evaluation of second-order Molodensky-type formulas. OSU Rep. 163, Dept. of Geodetic Science and Surveying, The Ohio State Univ., Columbus.
- Milbert, D. (1999). The dilemma of downward continuation. AGU 1999 Spring Meeting, June 1-4, 1999, Boston, Massachusetts.
- Molodenskii, M.S., V.F. Eremeev, and M.I. Yurkins (1960). *Methods for Study of the External Gravitational Field and Figure of the Earth*. (Translated from Russian by the Israel Program for Scientific Translation, Office of Technical Services, Department of Commerce, Washington, D. C., 1962.)
- Moritz, H. (1976). Least-square collocation as a gravitational inverse problem. OSU Rep. 249, Dept. of Geodetic Science and Surveying, The Ohio State Univ., Columbus.
- Moritz, H. (1980). Geodetic Reference System 1980, Geodesist's Handbook. *Bull. Géod.*, 66, 187-192.
- Moritz, H. (1980). *Advanced Physical Geodesy*, Wichmann, Karlsruhe.
- Najafi, M. (1996). The Computation of a Precise Regional Geoid. Ph.D Dissertation, Dept. of Geodesy and Geomatics Engg., Univ. of New Brunswick.
- Novák, P. (2000). Evaluation of gravity data for the Stokes-Helmert Solution to the geodetic boundary-value problem. Ph.D Dissertation, Dept. of Geodesy and Geomatics Engg., Univ. of New Brunswick, GGE Technical Report No. 207.
- Novák, P., P. Vaníček, M. Véronneau, W. E. Featherstone, and S. A. Holmes (2000). On the accuracy of Stokes's integration in the precise high-frequency geoid determination. *Journal of Geodesy*, 74, 644-654.

- Novák, P., M. Kern, K. P. Schwarz (2000). On the determination of the relative geoid from airborne gravimetry. GGG2000, July 31-August 4, 2000, Banff, Alberta, Canada.
- Pagiatakis, S. D. (1988). Ocean tide loading on a self-gravitating, compressible, layered, anisotropic, visco-elastic and rotating Earth with solid inner core and fluid outer core. Tech. Rep. 139, Dept. of Surveying Engg., Univ. of New Brunswick.
- Pagiatakis, S. D. and Armenakis C. (1999). Gravimetric geoid modeling with GIS. *International Geoid Service Bulletin*, 8, 105-112.
- Pagiatakis, S. D., D. Fraser, K. McEwen, A. K. Goodacre and M. Véronneau (1999). Topographic mass density and gravimetric geoid modeling. *Bollettino Di Geofisica Teorica Ed Applicata* (in press).
- Press, W. H., S. K. Teukolsky, W. T. Vetterling and B. P. Flannery (1992). *Numerical Recipes in C - The art of Scientific Computing*, 2nd edition, Cambridge Univ. Press.
- Rapp, R. H., Y. M. Wang, and K. N. Pavlis (1991). The Ohio State 1991 geopotential and sea surface topography harmonic coefficient models. OSU Rep. 410, Dept. of Geodetic Science and Surveying, The Ohio State Univ., Columbus.
- Rizos, C. (1979). An efficient computer technique for the evaluation of geopotential from harmonic model. *Aust. J. Geod., Photogram. and Sur.*, 31, 161-169.
- Rummel, R., K. P. Schwarz, and M. Gerstl (1979). Least square collocation and regularization. *Bulletin Geodesique*, 53, 343-361.
- Schwarz K. P. (1978). Geodetic improperly posed problems and their regularization. Lecture Notes of the Second Int. School of Advanced Geodesy, Erice.

- Schwarz, K. P., M. G. Sideris, and R. Forsberg (1990). The use of FFT techniques in physical geodesy. *Geophys. J. Int.*, 100, 485-514.
- She, B. B., M. G. Sideris, and K. P. Schwarz (1993). A PC-based unified geoid for Canada. Final report for DSS contract No. 23244-0-4451/01-ET. The Univ. of Calgary, Dept. of Geomatics Engineering.
- Sideris, M. G. (1987). Spectral methods for the numerical solution of Molodensky's problem. UCSE Rep. 20024, Dept. of Surveying Engineering, The Univ. of Calgary.
- Sideris, M. G. and Y. C. Li (1993). Gravity field convolution without windowing and edge effects. *Bull. Géod.*, 60, 51-63.
- Sideris, M. G. and B. B. She (1995). A new, high-resolution geoid for Canada and part of the U. S. by the 1D-FFT method. *Bull. Géod.*, 69, 92-108.
- Sideris, M. G., P. Vaníček, J. Huang, and I. N. Tziavos (1999). A comparison of downward continuation techniques of terrestrial gravity anomalies. XXII IUGG Assembly, July 18-23, 1999, Birmingham, UK.
- Sjöberg, L. E. (1984). Least-squares modification of Stokes's and Vening Meinesz's formula by accounting for truncation and potential coefficient errors. *Manuscripta Geodaetica*, 9, 209-229.
- Sjöberg, L. E. (2000) Topographic effects by the Stokes-Helmert method of geoid and quasi-geoid determinations. *Journal of Geodesy*, 74, 255-268.
- Smith, D. A. and D. G. Milbert (1999). The GEOID96 high resolution geoid height model for the United States. *Journal of Geodesy*, 73, 219-236.
- Stokes, G. G. (1849). On the variation of gravity on the surface of the Earth. *Trans. Camb. Phil. Soc.*, 8, 672-696.

- Sun, W. and P. Vaníček, (1996). On the discrete problem of downward Helmert's gravity continuation. Proc. of Session G7 (Techniques for local geoid determination), Annual meeting of European Geophysical Society. The Hague, May 6-10, 1996, Rep. of the Finnish Geodetic Institute, 96:2, pp. 29-34.
- Sun, W. and P. Vaníček, (1998). On some problems of the downward continuation of the $5' \times 5'$ mean Helmert gravity disturbance. *Journal of Geodesy*, 72, 411-420.
- Tikhonov, A. N. and V. Y. Arsenin (1977). *Solution of Ill-Posed Problems*, John Wiley and Son, New York, Toronto, London, Sydney.
- Tarantola, A. (1987). *Inverse Problem Theory*, Elsevier, Amsterdam.
- Tscherning, C. C., and R. H. Rapp (1974). Closed covariance expressions for gravity anomalies, geoid undulations and deflections of the vertical implied by anomaly degree variance models. OSU Rep. 208, Dept. of Geodetic Science and Surveying, The Ohio State Univ., Columbus.
- U.S. Geological Survey (1998). Geology of the Conterminous United States at 1:2,500,000 Scale Geology of the Conterminous United States at 1:2,500,000 Scale-A Digital Representation of the 1974 P.B. King and H.M. Beikman Map, U.S. DEPARTMENT OF THE INTERIOR.
- Vaníček P (1971). Introduction to Adjustment Calculus. Lecture Notes 20, Dept. of Surveying Engg., Univ. of New Brunswick.
- Vaníček, P. and E. J. Krakiwsky (1986). *Geodesy: The Concepts*, 2nd corrected ed., North Holland, Amsterdam.
- Vaníček, P. and A. Kleusberg (1987). The Canadian geoid- Stokesian approach. *Manuscripta Geodaetica*, 12, 86-98.

- Vaníček, P. and L. E. Sjöberg (1991). Reformulation of Stokes's theory for higher than second-degree reference field and a modification of integration kernels, *JGR*, 96(B4), 6529-6539.
- Vaníček, P. and Z. Martinec (1994). The Stokes-Helmert scheme for the evaluation of a precise geoid. *Manuscripta Geodaetica*, 19, 119-128.
- Vaníček, P., A. Kleusberg, R. G. Chang, H. Fashir, N. Christou, M. Hofman, T. Kling, and T. Arsenault (1987). The Canadian geoid. Dept. of Surveying Engineering, Univ. of New Brunswick, P.O. Box 4400, Fredericton, N. B., Canada, E3B 5A3.
- Vaníček, P., A. Kleusberg, Z. Martinec, W. Sun, P. Ong, M. Najafi, P. Vajda, L. Harrie, P. Tomášek, and B. Ter Horst (1995a). Compilation of a precise regional geoid. Final report on research done for the Geodetic Survey Division, Geomatics Sector, Natural Resources Canada, Ottawa, under a DSS contract No. 23244-1-4405/01-SS.
- Vaníček, P., M. Najafi, Z. Martinec, L. Harrie, and L. E. Sjöberg (1995b). Higher-degree reference field in the generalized Stokes-Helmert scheme for geoid computation. *Journal of Geodesy*, 70, 176-182.
- Vaníček, P., W. Sun, P. Ong, Z. Martinec, M. Najafi, P. Vajda, and B. Ter Horst (1996). Downward continuation of Helmert's gravity anomaly. *Journal of Geodesy*, 71, 21-34.
- Vaníček, P., J. Huang, and P. Novák (1997). DOWN'97 discrete Poisson downward continuation program package for 5' by 5' data, Contract Progress Report for Geodetic Survey Division of Canada, Ottawa.
- Vaníček, P., J. Huang, and P. Novák (1998). A comparison of downward continuation techniques of terrestrial gravity anomalies. Contract Progress Report for

Geodetic Survey Division of Canada, Ottawa.

- Vaníček, P., J. Huang, P. Novák, S. D. Pagiatakis, M. Véronneau, Z. Martinec and W. E. Featherstone (1999). Determination of boundary values for the Stokes-Helmert problem. *Journal of Geodesy*, 73, 180-192.
- Vaníček, P. and J. C. F. Wong (1999). On the downward continuation of Helmert's gravity anomalies. Spring Meeting of the American Geophysical Union, June 1-4, 1999, Boston, MA, US.
- Véronneau, M (1996). The GSD95 geoid model of Canada. Gravity, Geoid and Marine Geodesy, Proceedings of International Symposium, Tokyo, Japan, 1996. Springer Vol.117, 573-580.
- Varah, J. M. (1979). A practical examination of some numerical methods for linear discrete ill-posed problems. *SIAM Review*, 21, 100-111.
- Wang, Y. M. and R. H. Rapp (1990). Terrain effects on geoid undulation computations. *Manuscripta Geodaetica*, 15, 23-29.
- Wang, Y. M. (1988). Downward continuation of the free-air gravity anomalies to the ellipsoid using the gradient solution, Poisson's integral and terrain correction - numerical comparison of computations. OSU Rep. 393, Dept. of Geodetic Science and Surveying, The Ohio State Univ., Columbus.
- Wong J. C. F. (2001). On Picard criterion and the well-posed nature of harmonic downward continuation. MSE Dissertation, Dept. of Geodesy and Geomatics Engg., Univ. of New Brunswick, GGE Technical Report No. 213.
- Wong, L. and R. Gore, (1969). Accuracy of geoid heights from modified Stokes kernels. *Geophys. J r. astr. Soc.*, 18, 81-91.

Wichiencharoen, C. (1982). The indirect effects on the computation of geoid undulations. OSU Rep. 336, Dept. of Geodetic Science and Surveying, The Ohio State Univ., Columbus.

Xu, P. L. and R. Rummel (1992). A generalized regularization method with applications in determination of potential field. in: Proc. 1st Continental Workshop on the geoid in Europe, Prague, May 11-14, 1992, 444-457.

Vita

Candidate's full name : Jianliang Huang

Place / date of birth : 128, Kuitun, Xinjiang, P. R. China / July 09, 1965

Permanent address : Jia Gong Company, 128, Kuitun
Xinjiang, 833207
P. R. China

Schools attended : Elementary School, 128, Kuitun, Xinjiang, 1973 – 1978
High School, 128, Kuitun, Xinjiang, 1978 – 1983

Universities attended : Wuhan Technical University of Surveying and Mapping,
Wuhan, Hubei, P. R. China, 1983 – 1987
Institute of Seismology, State Seismological Bureau,
Wuhan, Hubei, P. R. China, 1987-1990
University of New Brunswick,
Fredericton, New Brunswick, Canada, 1996 – 2001

University degree : Bachelor of Engineering, Wuhan Technical University of
Surveying and Mapping, 1987
Master of Science, Institute of Seismology, State Seis-
mological Bureau, 1990

Main Publications

Huang, J., P. Vaníček, S. Pagiatakis and W. Brink (2001). Effect of topographical mass density variation on gravity and geoid in the Canadian Rocky Mountains. *Journal of Geodesy*, 74, 805-815.

Huang, J., P. Vaníček and P. Novák (2000). An alternative algorithm to FFT for the numerical evaluation of Stokes's integral. *Stud. Geoph. et Geod.*, 44, 374-380.

Vaníček, P., **J. Huang**, P. Novák, S. D. Pagiatakis, M. Véronneau, Z. Martinec, and W. E. Featherstone (1999). Determination of boundary values for the Stokes-Helmert problem. *Journal of Geodesy*, 73, 180-192.

Huang, Jian-Liang, Chong-Yang Shen and Hui Li (1998). Robust inversion analysis of local gravity anomalies caused by geological dislocation model of faults. *Acta Seismologica Sinica*, 20(1), 86-95 (in both Chinese and English editions).

Li, Rui-Hao, **Jian-Liang Huang**, Hui Li and Dong-Sheng Chen (1997). The mechanism of regional gravity changes before and after the Tangshan earthquake. *Acta Seismologica Sinica*, 19(4), 399-407 (in both Chinese and English editions).

Huang, Jian-Liang, Wei-Zhong Wang and Hong-Jiao Xue (1997). Dynamic analysis of seismic stability of slopes. *Earthquake Engineering and Engineering Vibration*, 17(4), 113-122 (in Chinese).

Huang, Jian-Liang, Hui Li and Rui-Hao, Li (1995). Gravity and its potential changes caused by point dislocation, *Acta Seismologica Sinica* , 17(1), 72-80 (in both Chinese and English editions).

Huang, Jian-Liang, Hui Li, Jie-Lin Yu (1995). Application of gravimetry in studies of fault motion. *Crustal Deformation and Earthquake*, 15 (Supplementary) (in Chinese).

Main Conference Papers

Huang, J., S. D. Pagiatakis and M. Véronneau (2000). Truncation of Poisson's integral in upward and downward continuations of the Earth's gravity. GGG2000, July 31-August 4, 2000, Banff, Alberta, Canada. In Proc IAG Symp, Banff, Sideris (ed.), Gravity, Geoid and Geodynamics 2000, Vol. 123, 323-328, Springer-Verlag, 2001.

Vaniček P., J. Janák and **J. Huang** (2000). Mean vertical gradient of gravity. GGG2000, July 31-August 4, 2000, Banff, Alberta, Canada.

Huang, J., M. Véronneau and S. D. Pagiatakis (2000). On the ellipsoidal correction to the spherical Stokes in the determination of geoid. CGU2000, May 23-27, 2000, Banff, Alberta, Canada.

Véronneau, M. and **J. Huang** (2000). A preliminary Canadian gravimetric geoid model 2000: GSD. CGU2000, May 23-27, 2000, Banff, Alberta, Canada.

Sideris, M. G., P. Vaniček, **J. Huang**, and I. N. Tziavos (1999). A comparison of downward continuation techniques of terrestrial gravity anomalies. XXII IUGG Assembly, July 18-23, 1999, Birmingham, UK.

Huang, J., P. Vaniček, W. Brink, and S. D. Pagiatakis (1999). Effect of topographical mass density variation on gravity and the geoid. Spring Meeting of the American Geophysical Union, May 31 - June 3, 1999, Boston, MA, US.

Huang, Jian-Liang, Hui Li, Rui-Hao Li (1993). Fault creep and gravity changes before and after Tangshan Earthquake in 1976. CRCM'93 of IAG, December 6-11, 1993, Kobe, Japan, in *Proc. CRCM'93*, 279-284.

Li, Rui-Hao, **Jian-Liang Huang**, Hui Li (1993). Effects of the earth tide deformation on GPS measurements. CRCM'93 of IAG, December 6-11, 1993, Kobe, Japan, in *Proc. CRCM'93*, Kobe, Japan.